University of Southampton

Faculty of Natural and Environmental Sciences

The structure, fluid distribution and earthquake potential of the Makran Subduction Zone, Pakistan

By

Gemma Louise Smith

Thesis for the degree of Doctor of Philosophy

May 2013

UNIVERSITY OF SOUTHAMPTON

ABSTRACT

FACULTY OF NATURAL AND ENVIRONMENTAL SCIENCES

Ocean and Earth Science

Thesis for the degree of Doctor of Philosophy

THE STRUCTURE, FLUID DISTRIBUTION AND EARTHQUAKE POTENTIAL OF THE MAKRAN SUBDUCTION ZONE, PAKISTAN

By Gemma Louise Smith

The Makran subduction zone (offshore Pakistan and Iran) has the largest accretionary prism of any margin worldwide, formed due to the thick incoming sediment section of up to 7.5 km. This margin has been relatively understudied, and this thesis presents a new, detailed structural and hydrological interpretation and seismogenic hazard assessment for the Makran. The accretionary prism is dominated by simple, imbricate thrusts which form seaward verging, anticlinal ridges up to 200 km long. The prism has a low average taper angle of 4.5°. Two oceanic basement features intersect the deformation front: The Little Murray Ridge (LMR), a discontinuous, largely buried seamount chain, and the Murray Ridge, a large transtensional ridge. The subduction of the LMR causes an increase in fault spacing, a seaward step in the position of the deformation front, and may segment earthquake rupture. The Murray Ridge influences the incoming sediment stratigraphy and reduces sediment thickness in the east. Fault activity in the Makran is widely distributed within the prism, with over 75% of faults showing some evidence for recent activity. This may be the result of the high levels of frontal accretion causing the Makran to behave as a sub-critical prism. The décollement in the outer prism occurs within the sediment section and is unreflective. There is extensive evidence for fluid and fluid migration in the Makran, with a widespread hydrate BSR, high amplitude gas zones in the shallow sediment, reflective fault sections (indicating high porosity and likely high pore pressure), and surface seeps. The spatial distribution of these features appears to be controlled by changes in the incoming section and fault activity, and significant fluids are trapped within anticlinal hinge zones. Reflective fault sections are concentrated in the upper sediments, and there is no evidence for a significant fluid contribution from the deeper (>4 km) sediment section. This may indicate that the lower sediment section is largely dehydrated, prior to accretion.

The Makran experiences low seismicity compared to many global subduction zones, but produced a M_w8.1 tsunamigenic earthquake in 1945. Thermal modelling suggests that temperatures at the plate boundary are over 150°C at the deformation front due to the thick sediment section. These results suggest that the plate boundary may have the potential to be seismogenic to shallow depths. Thermal modelling also indicates that the shallow dip of the subducting plate produces a wide potential seismogenic zone, which when combined with along-strike rupture scenarios produces potential earthquake magnitudes of M_w8.7-9.2 with significant regional hazard implications.

List of Contents

List of Figures

List of Tables

List of Accompanying Material

Appendix 1. Thermal modelling methodology and sensitivity test results.

Plate 1. Plot of all interpreted seismic reflection lines aligned at the deformation front.

Plate 2. Plot of all uninterpreted seismic reflection lines aligned at the deformation front.

Academic Thesis: Declaration Of Authorship

I, Gemma Louise Smith declare that this thesis entitled 'The structure, fluid distribution and earthquake potential of the Makran Subduction Zone, Pakistan' and the work presented in it are my own and have been generated by me as the result of my own original research.

I confirm that:

1. This work was done wholly or mainly while in candidature for a research degree at this University;
2. Where any part of this thesis has previously been submitted for a degree or any other qualification at this University or any other institution, this has been clearly stated;
3. Where I have consulted the published work of others, this is always clearly attributed;
4. Where I have quoted from the work of others, the source is always given. With the exception of such quotations, this thesis is entirely my own work;
5. I have acknowledged all main sources of help;
6. Where the thesis is based on work done by myself jointly with others, I have made clear exactly what was done by others and what I have contributed myself;
7. Parts of this work have been published as:
   - **Smith, G. L.**, L. C. McNeill, T. J. Henstock, and J. Bull (2012). The structure and fault activity of the Makran accretionary prism, Journal of Geophysical Research, 117, B07407, doi:10.1029/2012JB009312.
   - **Smith, G.L.**, L.C. McNeill, K. Wang, J, He, and T. J. Henstock (2013). Thermal structure and megathrust seismogenic potential of the Makran subduction zone, Geophysical Research Letters, 40, doi:10.1002/grl.50374.

Signed:

Date:

Acknowledgements

I would first like to thank my primary supervisor Lisa McNeill, who has been endlessly helpful, patient and insightful in helping me to extract coherent stories from the often confusing Makran! I feel very lucky to have had such a committed and enthusiastic supervisor. Many thanks also to the other members of my panel - Tim Henstock, Jonathan Bull and Ian Wright, for their helpful input, support and discussion.

I am very grateful to Kelin Wang and Jiangheng He from PGC in Canada for their help with the thermal modelling in Chapter 3. Particular thanks to Kelin and his family for their kind hospitality in Victoria. I would also like to thank Volkhard Spiess, Gerhard Bohrman and colleagues for their help with Chapter 4 (and hospitality in Bremen). Comments from editors and reviewers greatly improved Chapters 2 and 3 during the publication process. Tim Minshull provided helpful advice on the Makran throughout this project. I would like to thank Masters students Oliver Ralph (NOCS) and Daniel Arráiz (Bremen) for their contributions to initial data interpretation. Becky Cook has been the perfect 'subduction zone buddy' and has been an extremely helpful presence on the opposite side of the office! Gawen Trathen, Mark Vardy, Dean Wilson and Simon Dean – without your help I would have thrown my computer out of the window years ago – thank you for endlessly rescuing me from 'code doom' and not ignoring my plaintive emails. You are all wizards.

The support and encouragement I received from my excellent supervisors and lecturers during my undergraduate degree at the University of Birmingham (particularly Dr Andy Chambers and Professor Paul Smith) was crucial in giving me the confidence to attempt a PhD, and I am so grateful for their help!

I would have gone insane a hundred times over without the amazing PhD community at NOCS, particularly the plentiful past, present and honorary Blue House residents. Jen, Grant and Michael – you are all my PhD siblings whether you like it or not, and I can't imagine a more perfect set of housemates. Jen – I'm so glad we still don't know what each other's PhD's are about! Tommy, Teenie, Yasmin, Becky, Joe and Claud,

Jimbo and Claire, Jeff, Casey, Anya, Charlie B, Adam, Smiths 1 and 2 (Ed and Katie), Dave and so many others – you have all kept me constantly amused through the past 3.5 years and I feel very lucky to have such great friends! Most importantly Mike, you've rescued me from many meltdowns, been so supportive, and kept me laughing even through the hardest bits of my PhD. I can't wait for our next adventure!

Thank you to my sisters (Lottie and Katy) for their perfect indifference to science in general, and my PhD in particular, and for always being happy to provide Harry Potter and cat-based antidotes to PhD life. Thank you to my mum for being eternally practical, wise and helpful (and for the occasional bank transfer!). And finally thank you to my dad for being perhaps slightly less practical, always being so enthusiastic and interested in everything I do, and for always being proud of me.

1 Chapter 1. Introduction

1.1 Executive Summary and Project Rationale

In the past decade subduction zone earthquakes and their associated tsunami have killed over 250,000 people and caused extensive damage to coastal regions. The most notable recent examples; the 2004 Sumatra – Andaman earthquake, and the 2011 Tohoku-Oki earthquake both exhibited characteristics which surprised the scientific community in terms of their locations and slip distribution. One point highlighted by these events was the need to acknowledge the hazard which may be posed by previously understudied subduction zones and by those which may have been previously considered to be largely aseismic. Of particular interest in this respect are subduction zones with a high (>1-2 km) incoming sediment thickness, and ultra thick (>5-6 km) sediment margins such as the Makran, S. Hikurangi, S. Lesser Antilles, and Hellenic subduction zones which may have not experienced significant recent earthquakes (Henstock et al., 2006, Wallace et al., 2009, Shaw and Jackson, 2010, Gulick et al., 2011). Instead of inhibiting seismicity, a thick incoming sediment section may smooth the plate interface and promote high-magnitude earthquakes (Heuret et al., 2012). The deep sediment section may also be highly compacted, and be at sufficiently high temperatures to be largely dehydrated and therefore potentially seismogenic (e.g. Gulick et al., 2011). The Makran Subduction Zone has one of the thickest incoming sediment sections of any global subduction zone (up to 7.5 km), and experienced a M_w 8.1 earthquake in 1945 (Byrne et al., 1992) however it is overall relatively understudied in terms of both structure and seismic potential.

The Makran represents an end-member among global subduction zones with its high sediment input, low taper and large accretionary prism. Numerous studies have been made of the deformation and dynamics of other accretionary subduction zones such as Barbados (Lesser Antilles), Hikurangi (New Zealand), Nankai (Japan), Cascadia, Alaska and Sumatra in order to understand their evolution and mechanics (e.g. Moore et al., 1990a, MacKay, 1995, Gutscher et al., 1998, Bangs et al., 1999, Barker et al., 2009, Dean et al., 2010). Accretionary prism morphology and dynamics are

dependant on basal shear strength and the internal strength of the prism materials (Dahlen, 1990, Suppe, 2007). High sediment input accretionary margins commonly demonstrate low (< 5°) prism tapers, indicating a potentially weak basal surface (or high internal strength), however this must be reconciled with the occurrence of updip seismogenic rupture (e.g. at Sumatra in 2004 (Henstock et al., 2006)) which suggests a relatively strong basal surface. The strength of the basal surface (the plate boundary décollement) can also be strongly influenced by the occurrence of overpressured fluids sourced from the subducted sediment section, which may reduce its effective strength (Byrne and Fisher, 1990). At several high sediment input subduction zones, the décollement surface is highly reflective (e.g. Bangs et al., 1999, Park et al., 2002b, Tobin and Saffer, 2009), interpreted to suggest the presence of fluids at depth. Fluids may also be channelled along the imbricate thrusts of the prism itself, and potentially reach the surface as seabed seeps (e.g. Henry et al., 2002, Barnes et al., 2010), though this is likely to be controlled by relative permeabilities of the thrusts and adjacent sediments, and the distribution of deformation within the prism. It has also been suggested that high sediment input margins may evolve and deform in a different manner to traditional accretionary prisms, with more diffuse fault activity than the traditional model of fault activity focused on the frontal thrusts (Storti and McClay, 1995). Gaining a greater understanding of the development, deformation and hydrology of the Makran (the highest sediment input subduction zone) will therefore contribute to our understanding of subduction zones and fold and thrust belts worldwide, and help to inform some of the concepts introduced above.

1.2 Geological Background

The Makran subduction zone is located offshore Pakistan and Iran in the northwest Indian Ocean and is formed by the subduction of the Arabian Plate beneath the Eurasian plate in a northerly direction at ~4 cm/yr (DeMets et al., 2010). The subduction zone is separated from regions of continental collision in the west by the right-lateral strike-slip Minab Fault and in the east by the left-lateral Ornach-Nal fault system (Figure 1.1). Two onshore topographic depressions; the Jaz Murian and the Hamun-i-Mashkel, located between the Makran coastline and the Baluchistan

volcanoes are interpreted as forearc basins (Jacob and Quittmeyer, 1979). The Baluchistan Volcanic Arc occurs 400-600 km inshore from the trench, increasing in distance from the trench from west to east. This large trench-arc distance makes the Makran the widest forearc complex in the world, with an accretionary prism of up to 300 km in width (Leggett and Platt, 1984). The frontal 100 -150 km of the accretionary prism occur offshore and are the focus of this study.

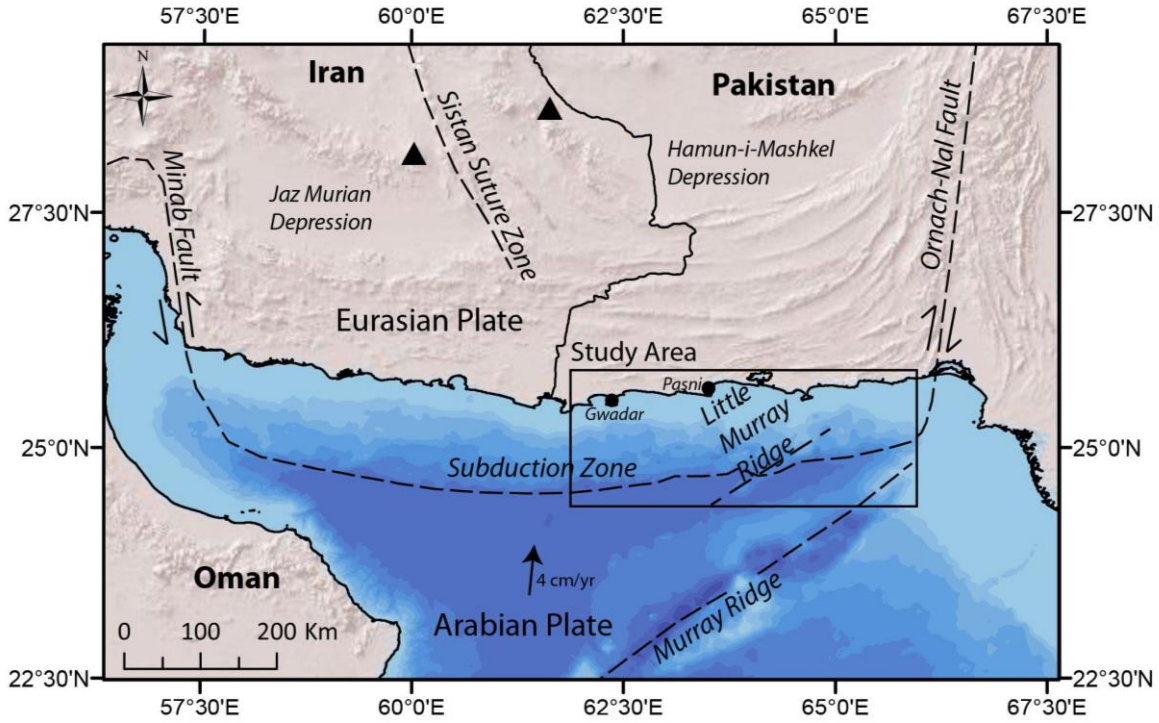

Figure 1.1. Location map of the Makran subduction zone indicating the main tectonic features. Black triangles are the Baluchistan volcanic arc. Bathymetry and topography are ESRI grids based on combined SRTM, GTOP030 and NOAA datasets.

The age of the subducting Arabian Plate has been debated (Edwards et al., 2000). There are no identifiable sea-floor magnetic anomalies in the region between the Murray Ridge and the Makran subduction zone (White, 1979) which has led to the suggestion that the oceanic crust in this region was formed in the Cretaceous "quiet" zone (Whitmarsh, 1979). Heat flow data also suggest an age of between 70-120Ma (Hutchison et al., 1981), however an alternative younger age of 50 – 60Ma has also been suggested based on different plate reconstruction models (Mountain and Prell, 1990).

The most notable feature of the Makran subduction zone is the thick incoming sediment section of up to 7.5 km and resulting wide (>400 km) accretionary prism. This thick sediment section is composed of sediments derived from an early stage of the Indus Fan (Clift et al., 2001), and sediment transported from the proximal coastlines of Pakistan and Iran (Bourget et al., 2011). Mud volcanoes are common onshore and have also been observed offshore, particularly on the continental shelf (Delisle et al., 2002), indicating degrees of overpressure. To the south of the accretionary prism the Murray Ridge, a significant transtensional basement ridge, trends southwest-northeast influencing basement topography and sediment transport and thickness (Edwards et al., 2000). To the north of, and running parallel to the Murray Ridge a smaller, discontinuous line of seamounts known as the Little Murray Ridge intersects the deformation front (White, 1983).

1.3 Previous Studies

The Makran subduction zone has relatively little historical coverage of published seismic reflection data, and what has been collected is concentrated in the region around Pasni and Gwadar (62.0-63.5°E). Multichannel lines (notably the Cam-30 line) shot by Cambridge University in the 80s were the only MCS data available for several years (White, 1982a, Minshull and White, 1989, Fruehn et al., 1997). Further data were collected by four legs on the RV Sonne in 1997-1998 (SO 122, 123, 124 and 130) and R/V Meteor Cruise 74, Legs 2 & 3, 2007; including reflection and refraction seismic data, magnetics, gravity, heat flow, swath bathymetry and sidescan sonar (e.g. Kopp et al., 2000, von Rad et al., 2000, Kukowski et al., 2001, Ding et al., 2010, Römer et al., 2012), but all focussed in this same region. Studies have also been undertaken on the Iranian half of the Makran, though to a lesser extent (Grando and McClay, 2007). Recent studies have collected cores and multibeam bathymetry to investigate seafloor morphology, sediment transport and deposition (Bourget et al., 2010, Mouchot et al., 2010). The Murray Ridge to the south has been studied with both multichannel seismic reflection data and potential field data (Edwards et al., 2000, Gaedicke et al., 2002). The Makran's seismicity was discussed by Byrne et al. (1992), and its potential for tsunami generation has also been investigated through numerical

modelling (Okal and Synolakis, 2008, Heidarzadeh et al., 2009). This study is based on over 6000 km of 2D multichannel seismic (MCS) reflection data collected by WesternGeco® in 1998-1999. This dataset is combined in places with multibeam bathymetry and sidescan sonar data collected on Leg 2 of Meteor Cruise 74 in 2007 (Spiess, 2007), and with data from other sources where required.

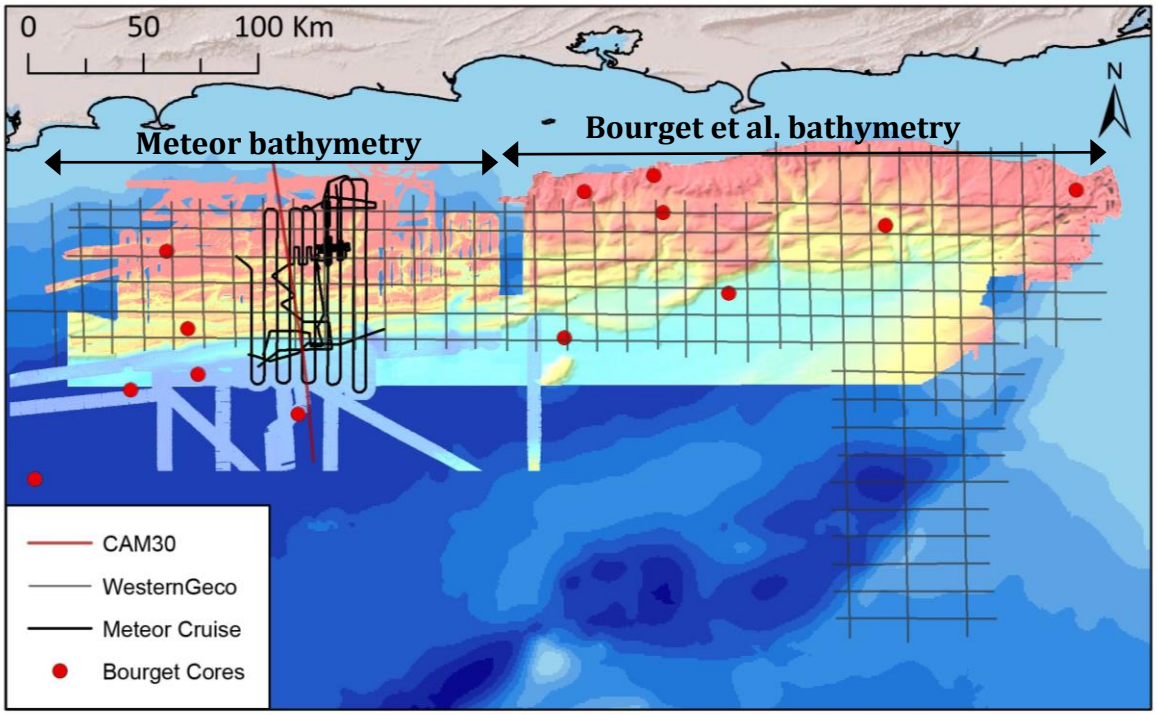

Figure 1.2. Overview of datasets utilised in this study. Includes WesternGeco, Meteor and CAM30 reflection seismic lines, Meteor and Bourget multibeam bathymetry, and Bourget long-piston core locations (Bourget et al., 2010).

1.4 Thesis Overview

Chapters 2 to 4 of this thesis have been prepared as independent papers for publication. Therefore to avoid repetition, these chapters are only briefly described below with a full abstract given at the start of each chapter. Another consequence of this formatting style is that relevant methods are described in each chapter rather than in a separate and self-contained 'Methods' chapter. Chapters 2 and 3 are published and Chapter 4 will be submitted shortly after thesis submission.

Chapter 2 - Structure and Fault Activity of the Makran Accretionary Prism

An analysis of the Makran Accretionary Prism based on over 6000 km of 2D seismic reflection data collected by WesternGeco and integrated with mulitbeam bathymetry data. This chapter focuses on the structure of the accretionary prism including fault geometry and continuity, décollement depth and properties, and fault activity. The key questions addressed by this chapter are:

(Q2.1). What is the dominant structural style of the Makran accretionary prism and how does this vary with incoming sediment thickness/basement topography?
(Q2.2). How does the unusually thick incoming sediment section affect the structure and prism taper of the Makran?
(Q2.3). How is activity and deformation distributed between the accretionary prism imbricate thrust faults and how does this vary along strike?
(Q2.4). What can we infer about the décollement properties of the Makran and what implications do they have for the seismogenic potential of the margin?

This paper was published in the Journal of Geophysical Research in July 2012.
Citation: *Smith, G. L., L. McNeill, T. J. Henstock, and J. Bull (2012). The structure and fault activity of the Makran accretionary prism, Journal of Geophysical Research, 117, B07407, doi:10.1029/2012JB009312.*

Chapter 3 - Thermal structure and megathrust seismogenic potential of the Makran subduction zone

This chapter inputs structural information from Chapter 2, in conjunction with additional data, into a 2D thermal model in order to generate the thermal structure of the Makran subduction zone. This allows the temperature of the subducting plate to be evaluated, and the potential seismogenic zone to be analysed using predicted (theoretical and experimental) thermal updip and downdip limits. This is then used to estimate potential maximum earthquake magnitudes for the Makran. The key questions addressed in this chapter are:

(Q3.1). What is the thermal structure of the Makran subduction zone, and how does this relate to the incoming section (sediment thickness) and plate geometry?
(Q3.2). Based on this thermal modelling, what are the maximum potential earthquake magnitudes which could be generated at the Makran?

This paper was published in Geophysical Research Letters in May 2013. Citation: *Smith, G.L., L. McNeill, K. Wang, J, He, and T. J. Henstock (2013). Thermal structure and megathrust seismogenic potential of the Makran subduction zone, Geophysical Research Letters, 40, doi:10.1002/grl.50374.*

Chapter 4 - Fluid generation and distribution in the highest sediment input accretionary margin, the Makran

This chapter uses seismic reflection data, in conjunction with published sidescan data and seafloor observations, to identify fluid-related features in the Makran accretionary prism. The primary features identified are a Bottom Simulating Reflector (BSR), high amplitude fluid-rich zones in the shallow (<3 km) sediment and reflective fault sections. The spatial distribution of these features is assessed in relation to the incoming section, wedge structure and faulting, and their depth distribution is related to the thermal structure of the sediment section and likely fluid-generating diagenetic processes. The Makran is compared to other margins at which similar features have been observed including Nankai (Japan) and Hikurangi (New Zealand). The key questions addressed in this chapter are:

(Q4.1). What is the distribution of fluid-related features in the Makran accretionary prism?
(Q4.2). How is fluid distribution in the Makran related to changes in the incoming section and prism structure?
(Q4.3). What are the potential fluid sources and how do these relate to the thermal structure of the margin?

This chapter forms the basis of a manuscript in preparation to be submitted to Earth and Planetary Science Letters in 2013.

Chapter 5 – Conclusions

This chapter summarises the results of the chapters 2-4, answers the questions posed in this chapter (1), and makes suggestions for future work.

2 Chapter 2. Structure and Fault Activity of the Makran Accretionary Prism

This chapter is a reproduction of an article published in the Journal of Geophysical Research in 2012 - *Smith, G., L. McNeill, T. J. Henstock, and J. Bull (2012). The structure and fault activity of the Makran accretionary prism, Journal of Geophysical Research, 117, B07407, doi:10.1029/2012JB009312.*

Data collected, analysed and written-up by Gemma Smith with feedback, discussion and editorial assistance from Lisa McNeill, Tim Henstock and Jonathan Bull.

Structure and Fault Activity of the Makran Accretionary Prism

Gemma L. Smith[1], Lisa C. McNeill[1], Timothy J Henstock[1], Jonathan Bull[1]

[1]Ocean and Earth Science, National Oceanography Centre Southampton, University of Southampton, SO14 3ZH, UK

Abstract

The Makran Subduction Zone has the highest incoming sediment thickness (up to 7.5 km) of any subduction zone. These sediments have formed a wide accretionary prism (~400 km). Seismicity in the Makran is generally low; however the margin experienced a M_w 8.1 earthquake in 1945 which generated a significant regional tsunami. Seismic reflection data and swath bathymetry data from offshore Pakistan are used to analyze the structure and fault activity of the outer accretionary prism. The outer prism has a simple structure of seaward verging imbricate thrust faults, many continuous for over 100 km along strike. Fault activity is analyzed using basin stratigraphy and fault geometry, revealing a frontal continuously active zone, a central intermittently active zone, and a landward inactive zone. Over 75% of the faults in the seaward ~70 km of the prism show evidence for recent activity. The décollement occurs within the lower sediment section, but steps onto the top-basement surface in regions of elevated basement topography. Fault spacing (6 km) and taper (4.5 °) are comparable to other margins such as S. Hikurangi, Cascadia and Nankai, suggesting that high sediment input is not leading to an unusual prism structure. The décollement is unreflective, which is unexpected considering other prism characteristics predicting a weak surface, and may suggest a potentially stronger décollement than previously predicted. This study provides a significant advance in our understanding of the structure of an end member convergent margin and demonstrates that systematic analyses of accretionary prism structure can help to elucidate subduction zone dynamics with ultimate relevance to seismogenic potential.

2.1 Introduction

The Makran Subduction Zone is generated by the subduction of the Arabian Plate beneath the Eurasian plate at ~4 cm/yr offshore Pakistan and Iran (Figure 2.1). The accretionary prism is the largest accretionary complex in the world (Gutscher and Westbrook, 2009) and is thus an end member globally, with an exceptionally high incoming sediment thickness (up to 7.5 km) and a low taper of ~4 ° (Davis et al., 1983, Kopp et al., 2000). As well as high sediment input, the Makran is characterized by generally low seismicity, however it did experience a M_w 8.1 earthquake in 1945 (Byrne et al., 1992). The aim of this study is to interpret the morphology and structure of the outer Makran accretionary prism along a 400 km (along-strike) section offshore Pakistan, including an analysis of fault activity. This interpretation will allow the mechanical properties of the outer prism to be investigated, structural comparisons with other margins to be made, and will contribute to the understanding of its seismogenic potential. This manuscript is the first study of the Makran to systematically assess prism structure from seismic reflection data over such a large area. We evaluate the Makran Subduction Zone in the context of other global subduction zones (e.g. Southern Lesser Antilles, Hikurangi (New Zealand), parts of Cascadia and Sumatra/Sunda), including those with relatively high (>1 km) sediment input and/or large accretionary prisms. These accretionary prisms are also located at plate boundaries with slow to moderate convergence rates (~3-5 cm/yr), similar to the Makran (DeMets et al., 1990).

Fault activity within fold-thrust belts has been suggested to concentrate in the toe region, with activity reducing significantly landward of the deformation front. This suggestion has been supported by analogue (e.g. Davis et al., 1983, von Huene and Scholl, 1991, Gutscher et al., 1996) and numerical modelling (e.g. Willett et al., 1993, Fuller et al., 2006). Other studies suggest that the distribution of deformation may be more complex, with a wider zone of activity and reactivation of landward thrusts (Hardy et al., 1998, Lohrmann et al., 2003). Significant out-of-sequence thrusts, often associated with major structural and morphological boundaries, have been identified in margins such as Nankai, Japan and Sunda, Indonesia (Park et al., 2002a, Kopp and Kukowski, 2003). The Makran Subduction Zone, with its high sediment input and

wide accretionary zone, provides an ideal region in which to examine prism structure and strain distribution.

For submarine prisms, pore fluid pressure is an important controlling factor on thrust mechanics and the strength of prism materials (Moore and Vrolijk, 1992, Saffer and Bekins, 2006). Fluids are sourced both from the subducting oceanic crust and the incoming sediment section, and from digenetic dehydration reactions with increasing temperature (Moore and Saffer, 2001). As the subducting section is subjected to horizontal compression and vertical compaction, pore fluids attempt to migrate upwards. The presence of a thick sediment section with low vertical permeability may impede this fluid release, producing pore fluid pressures of up to lithostatic at the plate boundary (e.g. Moore and Vrolijk, 1992). Overpressured pore fluid can influence décollement properties, leading to decreased effective basal strength which in turn, according to Coulomb wedge theory, will produce a prism of low taper (Davis et al., 1983, Le Pichon et al., 1993). Elevated pore pressures have been inferred from seismic velocities at several subduction zones including Barbados and Nankai (e.g. Bangs et al., 1990, Tobin and Saffer, 2009). Fluid may migrate along the décollement horizon, vertically through the accreted sediment, or along thrust faults depending on the relative permeability of these pathways (e.g. Moore and Vrolijk, 1992, Le Pichon et al., 1993). The high sediment input experienced by the Makran suggests a potentially high fluid input, which may affect the mechanical properties of the prism.

Historically, aseismic behaviour was suggested to occur in the Makran, Hikurangi, Southern Barbados, and Cascadia subduction zones due to the presence of large accretionary prisms at these margins and relatively low background seismicity (Byrne et al., 1988). Subsequent to this suggestion, evidence of prehistoric earthquakes in the Cascadia region suggested that this margin, rather than being aseismic, produces large earthquakes. The occurrence of the 1945 Makran earthquake, ~30 km landward of the trench, has proved difficult to reconcile with other features of the Makran. The low taper, high sediment input and wide accretionary prism of the Makran would, according to traditional models (Byrne et al., 1988, Hyndman et al., 1997) suggest that the outer prism is largely aseismic. Prior to the Sumatra 2004 and Tohoku Oki 2011 events, seaward rupture was considered

unlikely, however both these events show evidence for rupture farther trenchward than anticipated, and in the case of the Sumatra 2004 event, through the outer prism (e.g. Henstock et al., 2006, Dean et al., 2010, Gulick et al., 2011, Ide et al., 2011).

2.1.1 Geological setting

The offshore Makran accretionary prism is located in water depths of 750 - 3000 m. There is no bathymetric trench seaward of the deformation front (~3000 m depth) due to the high sediment input. The age of the lithosphere in the Arabian Sea has been debated due to the lack of identifiable sea-floor magnetic anomalies in the region between the Murray Ridge and the Makran subduction zone (White, 1979). This absence has led to the suggestion that the oceanic crust in this region was formed either in the Cretaceous 'quiet zone', supported by heat flow measurements taken from shallow cores in the Gulf of Oman (Hutchison et al., 1981), or late Jurassic-early Cretaceous (Whitmarsh, 1979), or Palaeocene-Eocene (Mountain and Prell, 1990, Edwards et al., 2000), both suggested from plate reconstructions.

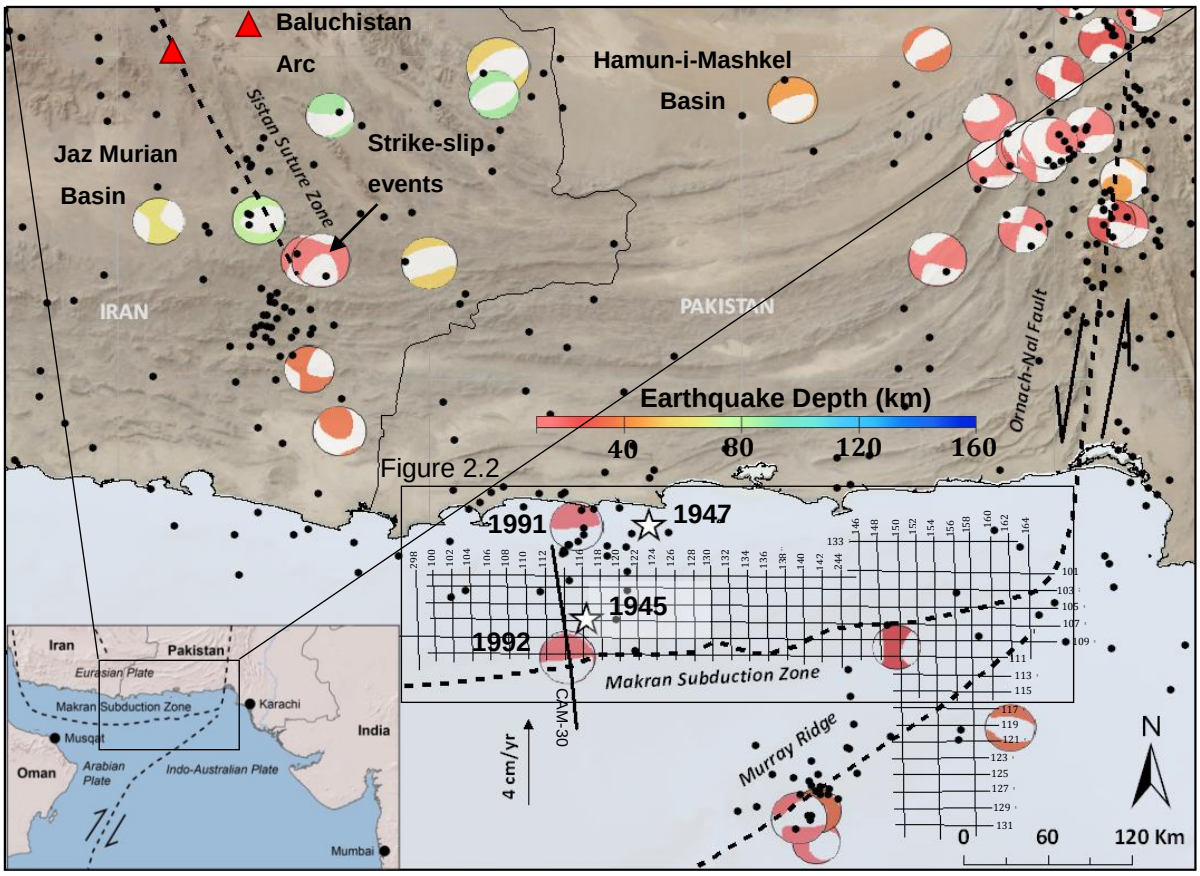

Figure 2.1. Location map of the Makran Subduction Zone. Inset shows the regional tectonics, with the Makran located where the Arabian Plate subducts beneath the Eurasian Plate. Main map shows focal mechanisms from the Global CMT Catalog (1976-present) coloured by depth. Black dots indicate earthquakes (>M_b 3.3) from ANSS catalogue from 1963-2011. In addition the 1945 and 1947 earthquakes are indicated by stars - locations from Byrne et al.(1992), Heidarzadeh(2008). Thick dashed lines indicate major tectonic boundaries. Fine black lines indicate the 2D seismic lines used in this study. Higher seismicity is visible in the Ornach-Nal strike slip system than the Makran Subduction Zone. Triangles are volcanoes. Topography is ESRI grid based on combined SRTM, GTOP030.

The Makran is bound to the west by the right-lateral Minab Fault and to the east by a triple junction consisting of the left-lateral Ornach-Nal fault system and the transtensional Murray Ridge (Figure 2.1). These strike-slip systems separate the Makran from regions of continental collision (Zagros and Himalayan). The Baluchistan Volcanic Arc, including the Bazman and Taftan Volcanoes in Iran, is located 400-600 km from the trench (Grando and McClay, 2007). Onshore, two

topographic depressions, the Jaz Murian and the Hamun-i-Mashkel, located between the accretionary prism and the Baluchistan volcanoes are interpreted as forearc basins (Jacob and Quittmeyer, 1979). These basins are separated by the N-S trending strike-slip Sistan Suture Zone (Figure 2.1) (Tirrul et al., 1983) which has been suggested to segment the subduction zone into discrete eastern and western zones, based on contrasting levels of seismicity (higher in the east) (Rani et al., 2011). This study is focused on the eastern offshore Makran subduction zone (east of the Sistan Suture), and on the outer ~70 km of the accretionary prism.

Mud volcanoes are common onshore, where they appear to be associated with E-W-trending fault zones (Ahmed, 1969) and sourced from the Upper Miocene Parkini mudstones (Schluter et al., 2002). Mud volcanoes and gas seeps have also been identified within the offshore prism (von Rad et al., 2000, Kukowski et al., 2001, Wiedicke et al., 2001, Ding et al., 2010).

2.1.2 Previous Studies

The offshore Makran currently has limited coverage of published seismic reflection data. Early seismic reflection surveys identified the imbricate structure of the accretionary prism (White, 1982a, Minshull and White, 1989). Further data, including seismic reflection and refraction, magnetic, gravity, heat flow and swath bathymetry datasets (offshore both Pakistan and Iran) allowed the thick sediment section and velocity structure to be resolved in more detail but with limited along-strike coverage (Kopp et al., 2000, Kukowski et al., 2001, Grando and McClay, 2007, Ding et al., 2010). Published core coverage is sparse, however analyses of 13 long piston cores (<35 m below sea level) from the trench and prism basins found high mean Holocene sedimentation rates (0.5-1.5 mm/yr) dominated by interbedded hemipelagite and turbidites (Bourget et al., 2010, Mouchot et al., 2010, Bourget et al., 2011).

2.1.3 Seismicity

The Makran is seismically relatively quiet compared to other margins such as Chile and Nankai, and more similar to quiescent margins such as Cascadia. However the region has experienced occasional significant historical earthquakes. The largest recent earthquake in the Makran occurred in 1945 (Figure 2.1), recently relocated to 24.5°N 63.00°E (Heidarzadeh et al., 2008), placing it only 30 km landward of the deformation front. This was a M_w 8.1 earthquake with a possible shallow-dip thrust source (focal mechanism derived from body waveform inversions of P and SH waves and dislocation modelling of coastal uplift, (Byrne et al., 1992)), interpreted as an interplate event at a depth of approximately 25-30 km. This event generated a tsunami which killed 4000 people locally, with wave heights up to 10 m (Heidarzadeh et al., 2008). A laterally extensive marine shelly bed in an intertidal lagoon in Oman has been interpreted as the 1945 tsunami deposit due to its shallow stratigraphic depth, although dating of the layer was unsuccessful (Donato et al., 2009). The highest run-up is reported to have affected the coast of Pakistan three hours after the earthquake. This time lag, in conjunction with the timing of undersea cable breaks, has been interpreted as evidence for widespread delayed slope failure triggered by the earthquake (Byrne et al., 1992). A further probable thrust earthquake in 1947 (M_w 7.3) is interpreted as an aftershock to the 1945 event, located 80 km to the northeast (Byrne et al., 1992). Smaller thrust earthquakes in the eastern Makran appear to also be N-S compressional events, potentially on the plate boundary (Byrne et al., 1992). The two thrust events illustrated on Figure 2.1 occurred in 1991 & 1992 with M_w of 5.6 & 5.8 respectively, both at a depth of ~15 km.

Deeper (>60 km), normal faulting events occur further landward likely within the subducting plate. A swarm of strike-slip events occurred further landward from 1978 to 1980 in the region of the Sistan Suture Zone (Figure 2.1) (Byrne et al., 1992). These events produced right-lateral strike-slip focal mechanisms, indicating that activity is still occurring along the suture zone. This suggests continued relative motion between the onshore Eastern and Western Makran, consistent with a level of segmentation in the onshore Eurasian plate. Higher levels of background seismicity

are recorded in the Murray Ridge and onshore strike-slip systems east and west of the Makran Subduction Zone, than in the subduction zone itself.

2.2 Data and analysis

The multichannel seismic (MCS) reflection dataset for this project consists of 6200 km of 2D data collected by WesternGeco® in 1998-1999 (Figure 2.1). These data were acquired using a 2250 cubic inch airgun array (4 strings) towed at a depth of 6.5 m, and recorded using a 5100 m streamer at 8 m depth with a shot spacing of 12.5 m. The MCS data are 102 fold, have been stacked and Kirchoff migrated and have undergone both pre- and post-stack deconvolution. The record length of these data is 10 seconds two-way-time (TWT). The dataset includes 19 strike lines and 34 dip lines with a line spacing of 12 km. Additional constraints on the incoming section in the west were gained through integration of the Cam-30 MCS Line (Minshull and White, 1989) (Figure 2.1). Swath bathymetry data covering an area roughly 75 km by 150 km of the western study area (Figure 2.2) were collected on Leg 2 of Meteor Cruise 74 in 2007 using a Simrad EM120 12 kHz hull-mounted multibeam system, at a speed of between 2.5 – 12 kts, and subsequently gridded at 50 m (Ding et al., 2010) and made available to this project. Additional bathymetric information for the central and eastern areas has been acquired from published multibeam bathymetry data images (Bourget et al., 2010).

MCS data have been interpreted using IESX (Schlumberger GeoFrame®). Horizons were picked using a combination of auto tracking and manual picking, and faults manually picked and where possible correlated between lines. The stacking velocities associated with this dataset are not used in this study as we do not currently have access to them; however published stacking velocity data from the Cam-30 line and coincident refraction lines can be incorporated allowing localized depth conversion & regional depth estimates. Kopp et al*. (2000)* recorded ocean-bottom-hydrophone (OBH) data and reported sediment velocities of between 1.8 km/s at the seabed to 4.4 km/s just above the basement (~7 km depth) on the oceanic plate in the western study area. They note a small velocity increase between the basal sediments and the

top of the oceanic basement landward of the deformation front, and a similarly small velocity increase between the accreted and underthrust sediment. Interval velocities from stacking velocities of the Cam-30 reflection line suggest high sediment velocities, of up to 4.5 km/s, in the deepest accreted sediment, and up to 4 km/s in the incoming section (Minshull and White, 1989).

2.3 Results

We describe outer accretionary prism fault structure and activity, décollement position and properties, prism taper analysis and stratigraphy of the incoming section.

2.3.1 Accretionary prism structure

Seafloor morphology is dominated by E-W trending ridges separated by narrow sedimentary (piggy-back) basins and cut by canyon-channel systems (Figure 2.2). The frontal ridge (formed by the frontal thrust) is a significant bathymetric feature, with a vertical relief of up to 1000 m and local gradients of over 30°. The frontal and subsequent ridges are anticlinal fault propagation folds which express the imbricate thrust structure of the accreted sediments, and can be used to aid along-strike fault correlation. Where a bathymetric ridge is not evident, correlation is more difficult, but can still be achieved using surrounding features, e.g. fault position relative to the hanging wall ridges of adjacent faults, similarities in fault structure and extrapolation of fault trend. The current correlations are conservative; therefore the length of some faults, particularly for those further landward, is likely underestimated (due to increased slope sediment cover and disruption by submarine canyons). Increased slope sediment blankets the accreted sediment and reduces the bathymetric expression of the ridges, thus making their bathymetric trace harder to follow. The frontal thrust can be confidently followed continuously for 250 km (Figure 2.2). The deformation front is intersected by the Murray Ridge and Little Murray Ridge (north

of and parallel to the Murray Ridge but with minimal bathymetric expression) (White, 1983) (Figure 2.2).

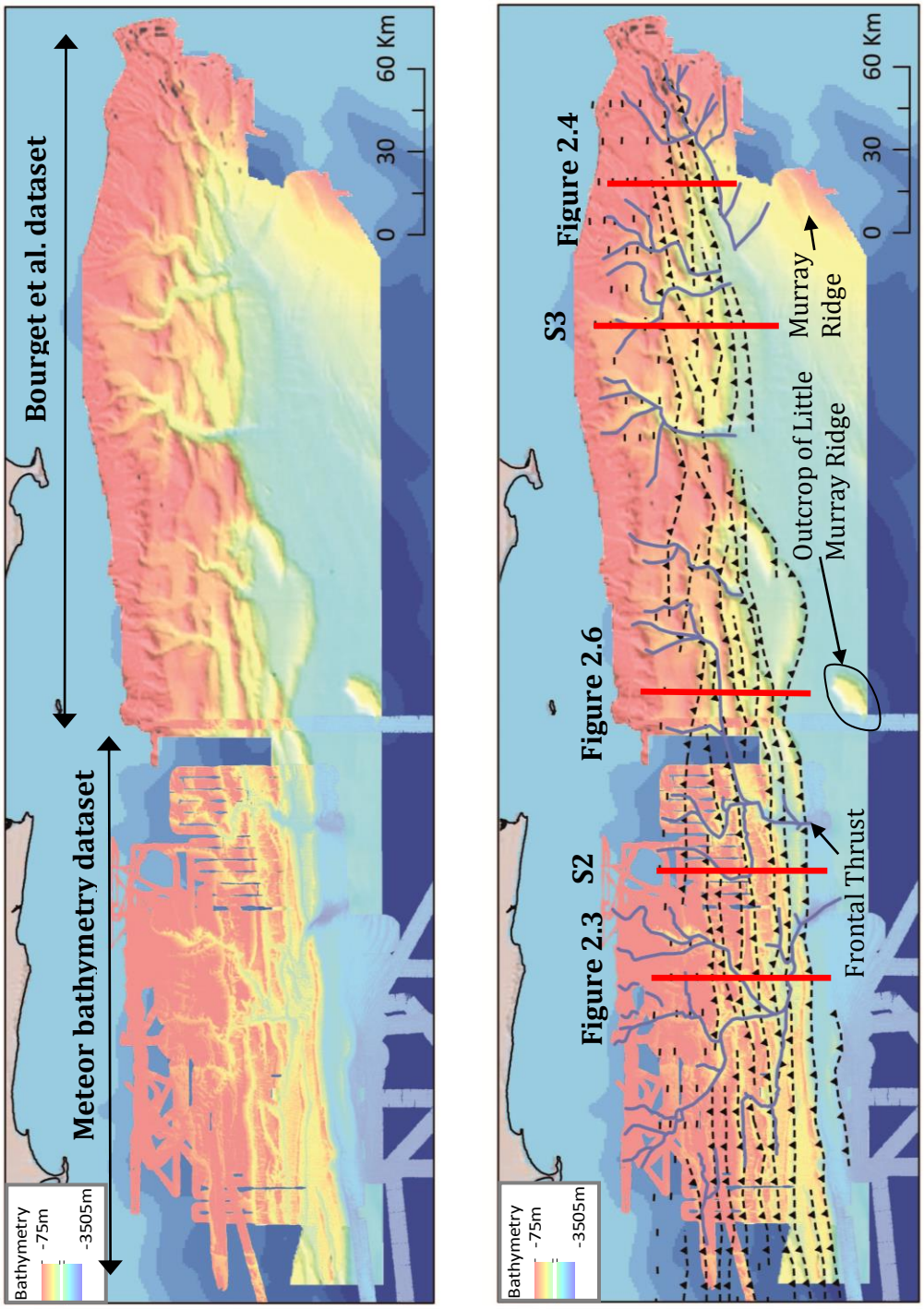

Figure 2.2. Structure map of the Makran accretionary prism. Imbricate thrust faults picked from MCS data and correlated with the aid of bathymetry data. Bathymetry data in east from Bourget et al. (2010). Submarine canyon-channel systems in blue. Water depth seaward of the deformation front ~3500 m. Location of supplementary figures S2 & S3 indicated.

Three reflection seismic lines (Figure 2.3, Figure 2.4, Figure 2.6) are presented to represent the structure of the accretionary prism, accompanied by two additional seismic lines presented as supplementary material (Figures S2 and S3). The imbricate thrusts are exclusively seaward vergent (landward dipping) with occasional secondary faults (backthrusts or minor forward thrusts with no associated anticline) (Figure 2.3). The fault propagation anticlines of the thrusts often contain small bending-moment normal faults in the hinge zone, driving collapse of the ridge slopes. The thrust faults dip at 20-30° and the majority strike E-W (080-090°). In the easternmost Makran there is a slight rotation in fault strike to the NE, following the trend of the deformation front as the Murray Ridge impinges. In the west and central regions of the study area a simple imbricate fault structure dominates, whereas fault structures become more complex in the east, with more antithetic backthrusts and secondary faults (Figure 2.4). Fault spacing fluctuates along the margin, varying from 2.2 km – 18.6 km (Figure 2.5), however median fault spacing remains fairly consistent at ~6 km, indicating that fault spacing increases are balanced by corresponding decreases. In the central region (overlying the obliquely subducting Little Murray Ridge) the second thrust steps inward relative to the frontal thrust (spacing >18 km) and the distance between the 2nd and 3rd thrusts is significantly reduced (2.2 km) (Figure 2.6). By the 3rd and 4th thrusts in this area, spacing has returned to the average value of ~6 km. The Little Murray Ridge at this location is approximately 30 km wide (measured perpendicular to the margin) where it intersects the deformation front. There is no evidence of the proposed strike-slip Sonne Fault cross-cutting the forearc, however the obliquity of this lower plate feature may preclude its clear imaging (Kukowski et al., 2000). Though the subducting basement ridges produce topography on the downgoing plate there does not appear to be any large scale segmentation (breaks in structure along strike, significant changes in structural style etc.) of the upper plate imbricate thrusts in response to subducting topographic features. This may be due to the smoothing effect of the thick sediment section overlying these basement ridges.

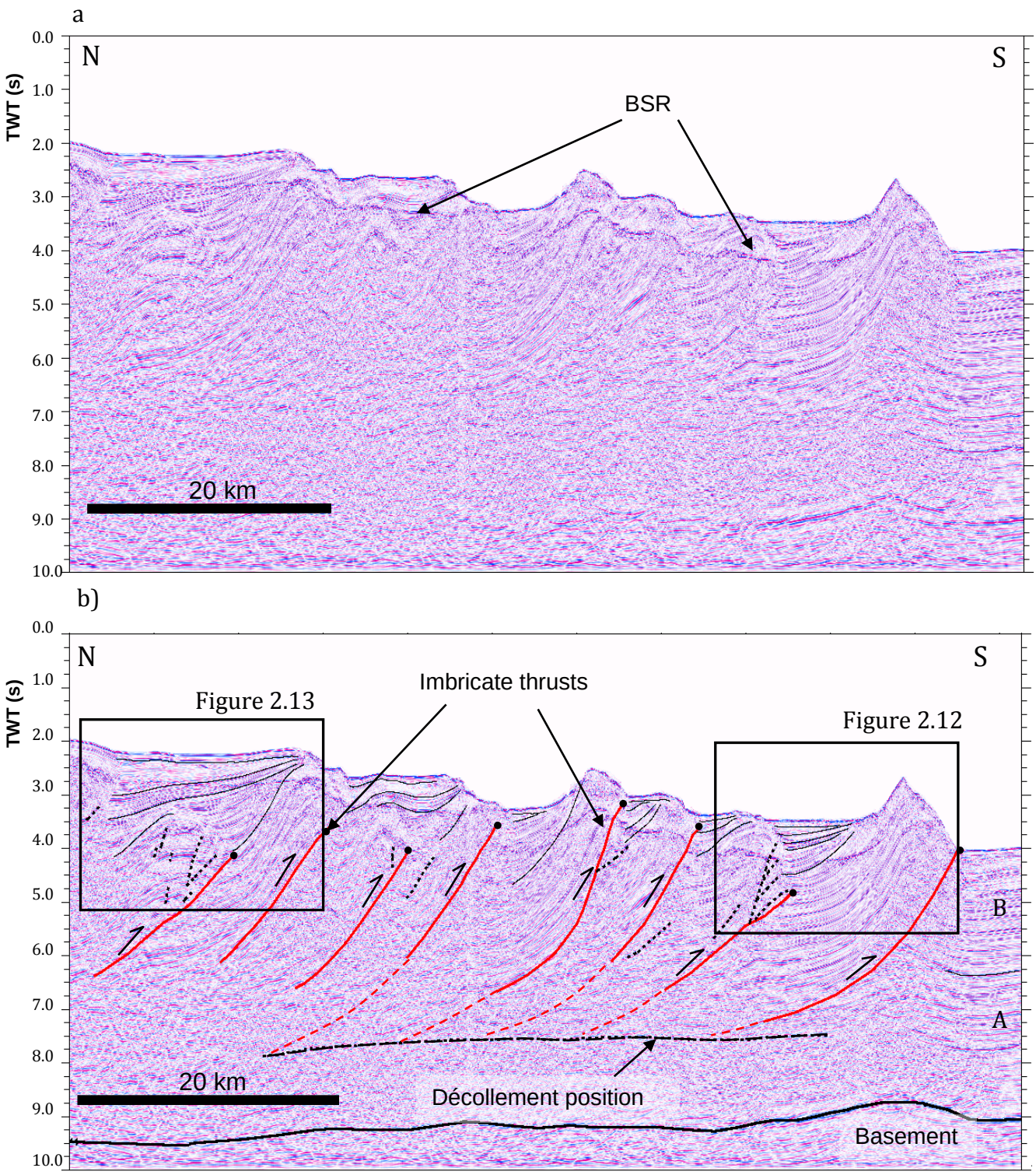

Figure 2.3. Seismic line 116 from the west of the study area (location on) a) without interpretation, b) with interpretation. Simple imbricate structure visible, with an average fault spacing of ~6 km. Increased sediment blanketing can be seen towards the north. Horizons interpreted in thin black lines – piggyback basin sediments. Incoming sediment thickness of 7.0 km. Width of view ~70 km. Vertical exaggeration x2.3 at seafloor. Location on Figure 2.2.

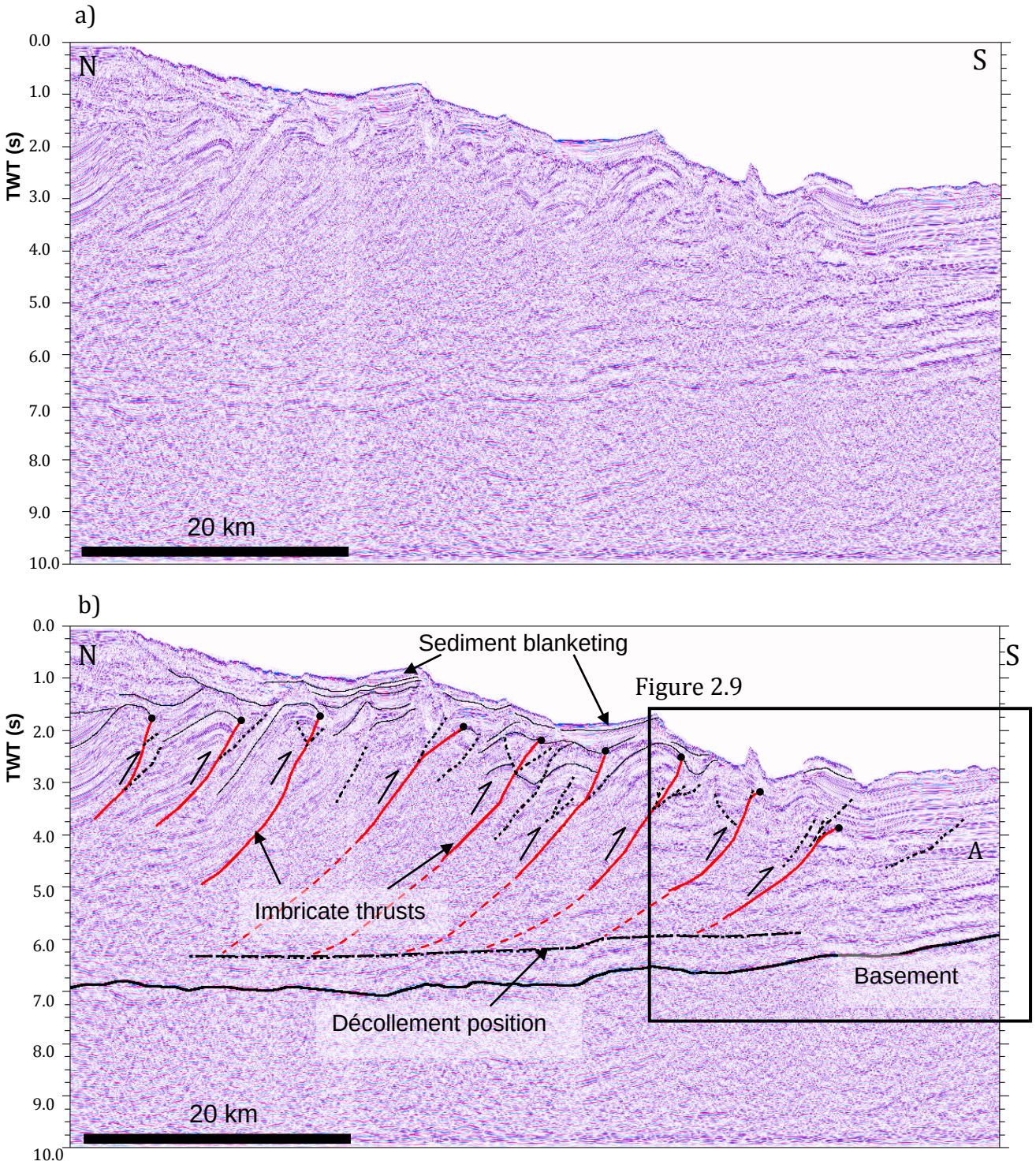

Figure 2.4. Seismic line 160 from the east of the study area a) without interpretation, b) with interpretation.Increased sediment input and channel structures visible. Incoming sediment thickness of 4.5 km. Width of view ~70 km. Vertical exaggeration of x2.5 at seafloor. Location on Figure 2.2.

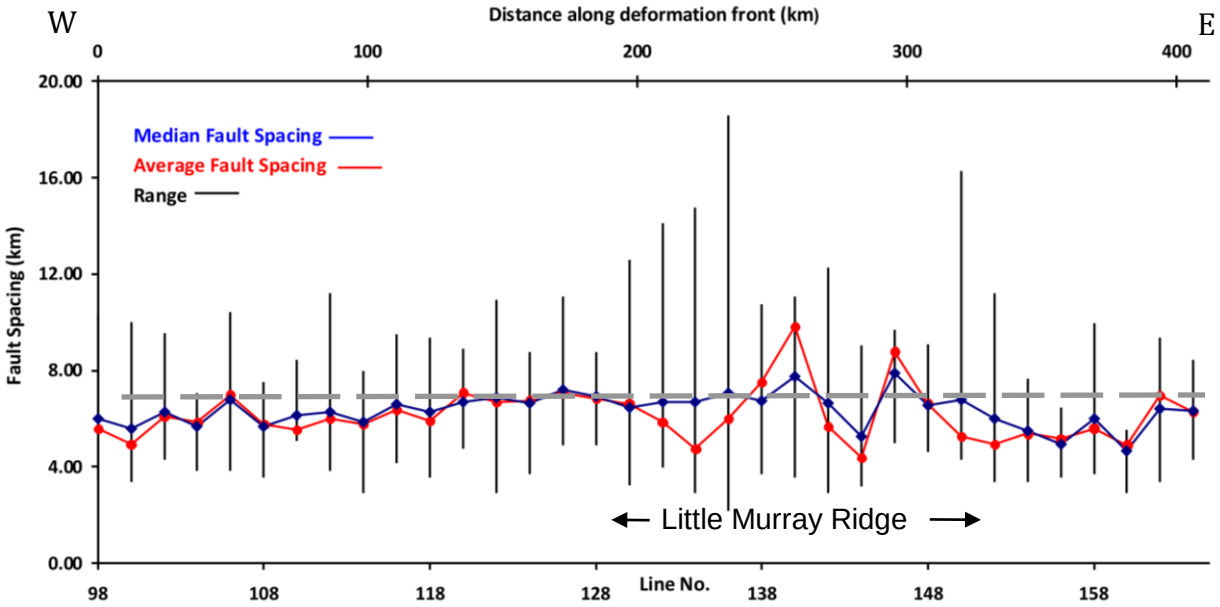

Figure 2.5. Plot of average (red) and median (blue) fault spacing for each line, with range of values indicated by black error bars. The range of values increases over the Little Murray Ridge. Average fault spacing along the margin is 6 km (grey dashed line).

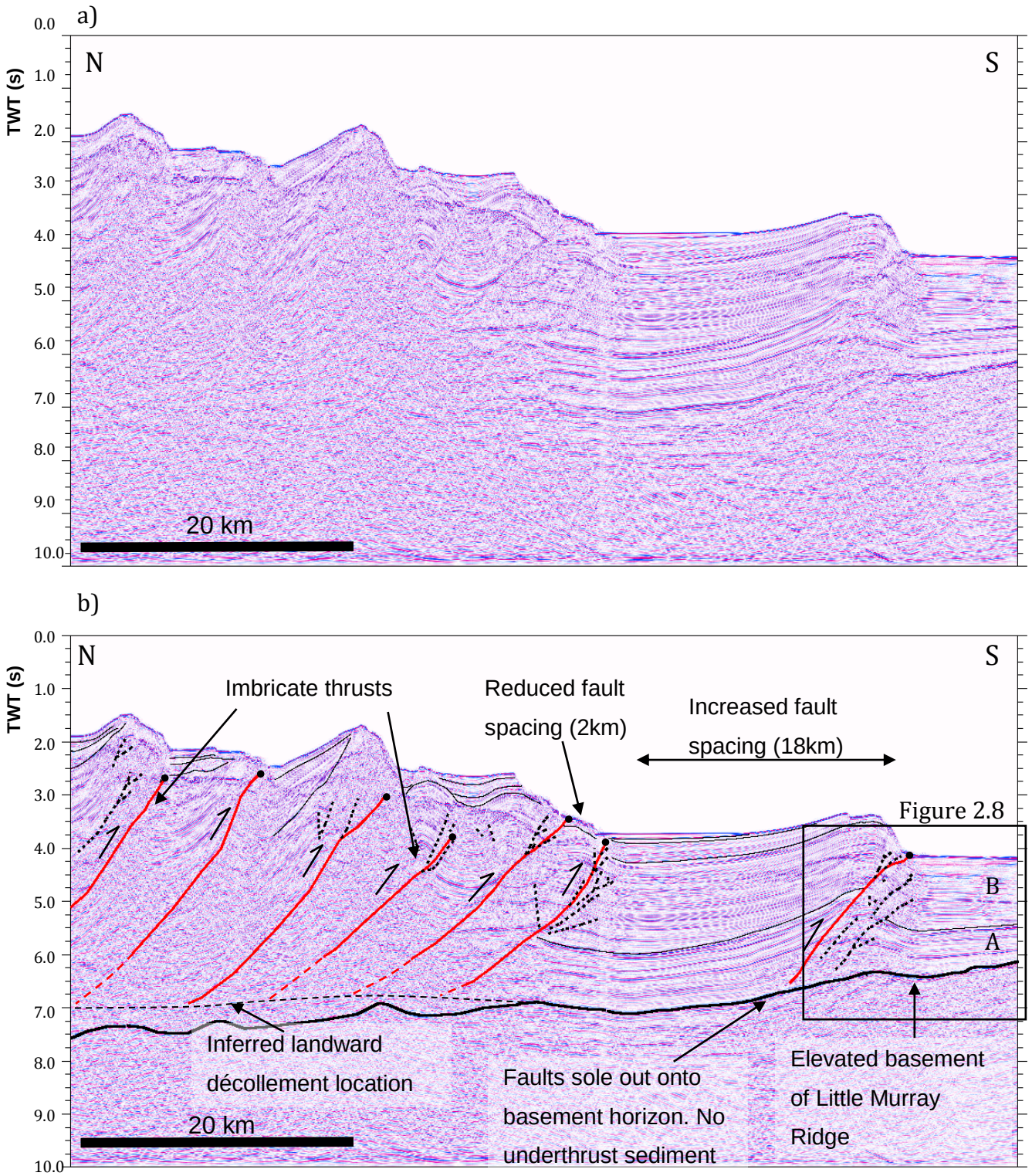

Figure 2.6. Seismic line 136 (over Little Murray Ridge a) without interpretation, b) with interpretation. W*idth of view is ~70 km. Sediment thickness of 2.5 km. Imbricate faults show more variable spacing and sole out onto the top-basement surface. 100% of the incoming section is accreted. Vertical exaggeration x 2.3 at seafloor. Location on Figure 2.2 .*

2.3.2 Sediment input and stratigraphy of the incoming sediment section

The accretionary prism is cut by submarine canyon-channel systems transporting sediment to the trench (from the Pakistan coast). Trench-parallel channel systems are also visible in the bathymetry data in the eastern trench region flowing from east to west; seaward extensions of significant fluvial systems such as the Hab and Bela sourced in the Himalayan collision zone. Stratigraphy of the incoming oceanic Arabian Plate has been interpreted from the MCS data; however a shortage of local borehole data prevents detailed lithological interpretation (Clift et al., 2002). The thickest input section (7.5 km) is in the west of the study area. In the central region, the elevated basement of the Little Murray Ridge (White, 1983) locally reduces sediment thickness (to as little as <1 km) and in the east the topography of the Murray Ridge flank reduces sediment thickness to approximately 5 km (Figure 2.7). The Murray Ridge may act as a barrier to northwards sediment transport and its evolution exerts a significant control on the stratigraphy of the input section.

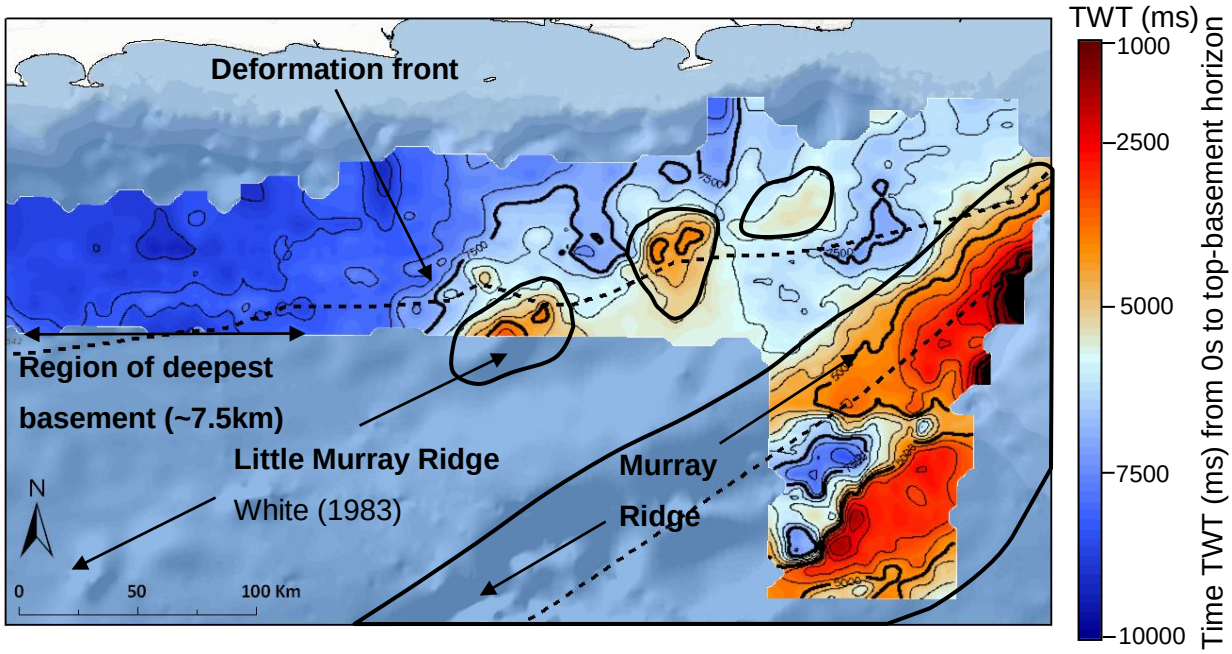

Figure 2.7. Grid of the depth to top-basement surface in TWT. The basement is dominated by NE/SW trending ridges: The Murray Ridge and Little Murray Ridge (outlined in thick black lines). The deepest basement occurs in the west at 3 s (~7.5 km) beneath the seabed. The top basement surface has been picked as the first high amplitude, positive polarity reflector at the base of the sediment pile, and by the

transition into chaotic reflections. Dashed black lines are tectonic boundaries. Bathymetry from (Smith and Sandwell, 1997)

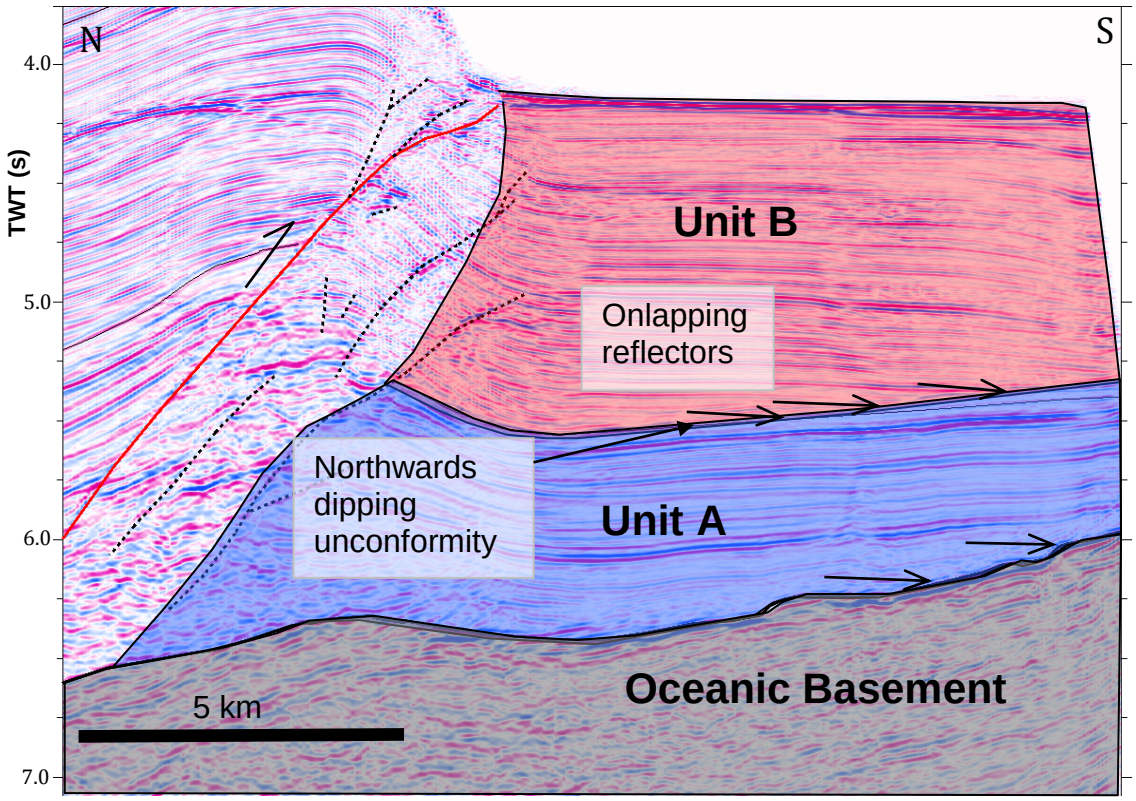

Figure 2.8. Close-up of the incoming section from Line 136. Three units can be identified: oceanic basement, and two sedimentary units (A & B). Width of view 17 km. Vertical exaggeration x 2.3 at seafloor. Location on Figure 2.6*b.*

The sediment input section can be divided into two units separated by a widespread N-dipping unconformity (Figure 2.8). The lower unit (Unit A) dips to the north, onlapping the basement, and can be correlated along the length of the deformation front. Reflectors are sub-parallel, closely spaced and laterally continuous. Reflector amplitude is variable with several high amplitude horizons visible, as well as some transparent sections. Channel-levee structures and normal faults are also visible in this unit, particularly in the east (Figure 2.9). Unit A has a fairly constant thickness of ~4 km (assuming a velocity of 2.5 km/s from Freuhn et al., (1997), with localized thinning over the Little Murray Ridge. The upper unit (Unit B) contains laterally continuous horizontal reflectors and does not show any evidence for normal faulting. It forms a wedge-shaped, horizontally-bedded unit, thinning to the south and east (onlapping onto Unit A) and thickening to the north and west, with a maximum

thickness of 3.5 km (velocity model from Freuhn et al. (1997)), and is absent in the easternmost lines. The regional unconformity separating the two units may either be due to subduction-related flexure, uplift of the Murray Ridge, or a combination of the two. The geometry of the upper unit, determined from contoured isopachs, trends SW-NW and parallel to the Murray Ridge, supporting a Murray Ridge related origin (White, 1983).

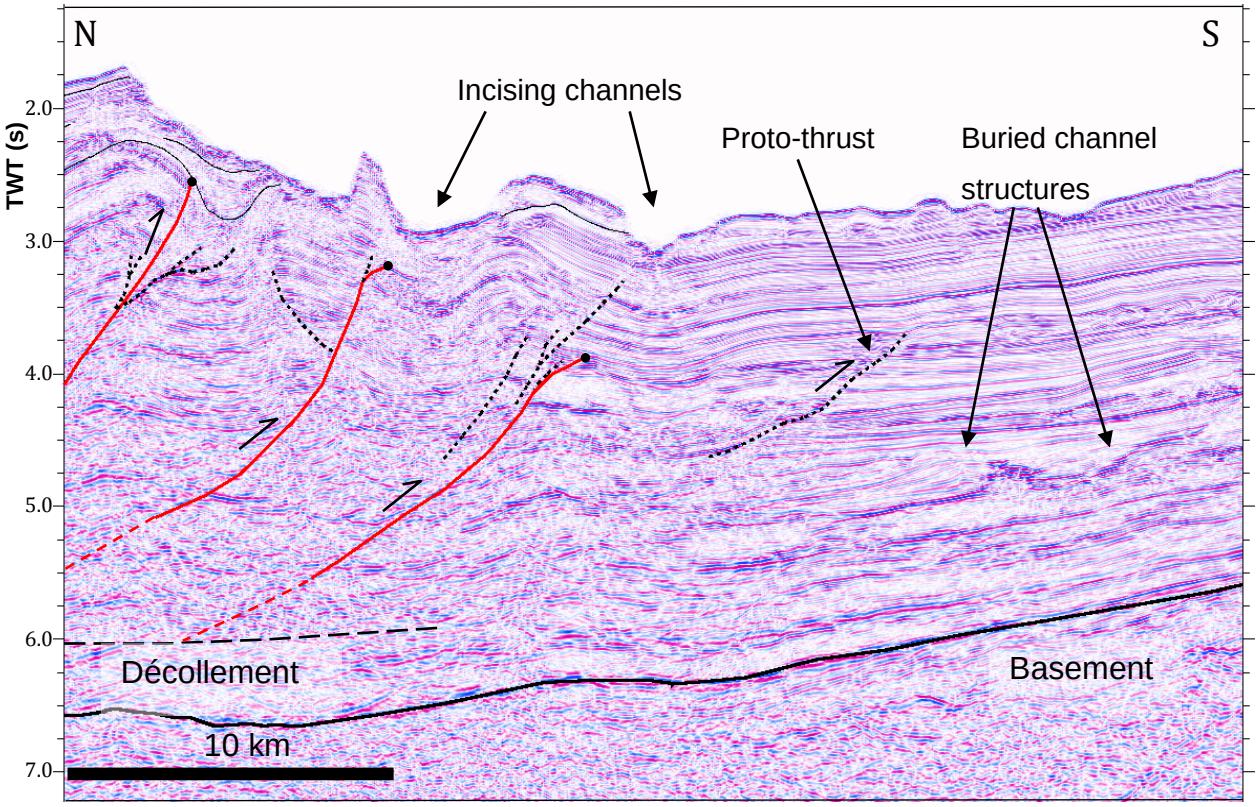

Figure 2.9. Buried channel structures in Unit A in the east of the study area (Line 160).Incising channels are also visible affecting the uppermost sediments. The entire incoming section is composed of Unit A in this region. Width of view 37 km. Vertical exaggeration x 2.3 at seafloor. Location on Figure 2.4.

Previous studies have also identified two units in the incoming section. The lower unit (Unit A) in the west of our study area has been interpreted as a turbidite unit derived from Himalayan uplift, with alternating hemipelagic and turbidite layers deposited in a proto-Indus fan (Fruehn et al., 1997, Schluter et al., 2002). The upper unit (Unit B) has been previously described as a mixed suite of turbidites and hemipelagics derived both from the east and the onshore Makran to the north

(Schluter et al., 2002) with deposition occurring from the late Miocene to present. The occurrence of modern trench-parallel channels in the eastern Makran shows that there is clearly a component of sediment transport from the east, not solely from the onshore Makran to the north. There is also evidence for small channels flowing northwards into the abyssal plain from the northern flank of the Murray Ridge (Figure 2.2).

2.3.3 Gas hydrate distribution

A BSR (bottom simulating reflector) is visible across much of the prism indicating the presence of widespread gas hydrate (Figure 2.3a). In the west and central regions of the study area the BSR is fairly ubiquitous; however in the east its distribution is greatly reduced. The BSR occurs at an average depth (TWT) of 500 ms (~500 m based on the velocity model of Minshull & White (1989)), consistent with the interpretations of Grevemeyer et al. (2000) from the west of the study area. The BSR does not appear to be disrupted where it crosses imbricate thrusts, as suggested by Minshull & White (1989), however further analysis of BSR properties and its relationship to faults and fluid flow is ongoing.

2.3.4 Décollement position and properties

The décollement beneath the outer prism is in general not reflective, however, its location can be inferred from the geometry and downward projection of thrust faults (i.e., where they sole out), the identification of the undeformed subducting sediment, and from the thickness of the accreted hanging wall sediment section. There is a level of uncertainty associated with locating the décollement surface within the sediment, as the boundary between accreted and underthrust sediment is, in most cases, not a visible sharp boundary. It is also possible that the décollement itself may not be a discrete horizon, rather a zone of sheared sediment. Estimating and integrating uncertainties from these methods, the interpreted décollement positions can be expected to have an error of +/- 0.5 s TWT (~600-700 m). The position of the

décollement surface can be estimated to 25-40 km landward of the deformation front, beyond which the thick, deformed sediment section precludes the identification of deeper structure and stratigraphy. The proportion of accreted versus underthrust sediment can be established by extrapolating the likely décollement position into the incoming section and analyzing its variation along strike.

The position of the décollement relative to the top-basement surface shows significant variations along strike (Figure 2.10). In the western survey area (Figure 2.3), the décollement sits within the section and the percentage of sediment accreted is 70-80 % (~4.3 km). At both locations the décollement surface is located within the lower sedimentary unit (Unit A), while all of Unit B is accreted. This agrees with previous studies (Fruehn et al., 1997, Kopp et al., 2000, Grando and McClay, 2007), all of which interpreted a décollement within the lower sedimentary unit, and from the mass balance calculations of Platt et al. (1985). To the east of the Little Murray Ridge (Figure 2.4) the décollement is again located within the Unit A and approximately 70-80% (~3-4 km) of the section is accreted. Thus, away from topographic basement anomalies, the décollement consistently occurs ~0.5-2 s TWT (~1.5-3 km) above basement, within the lower sedimentary unit.

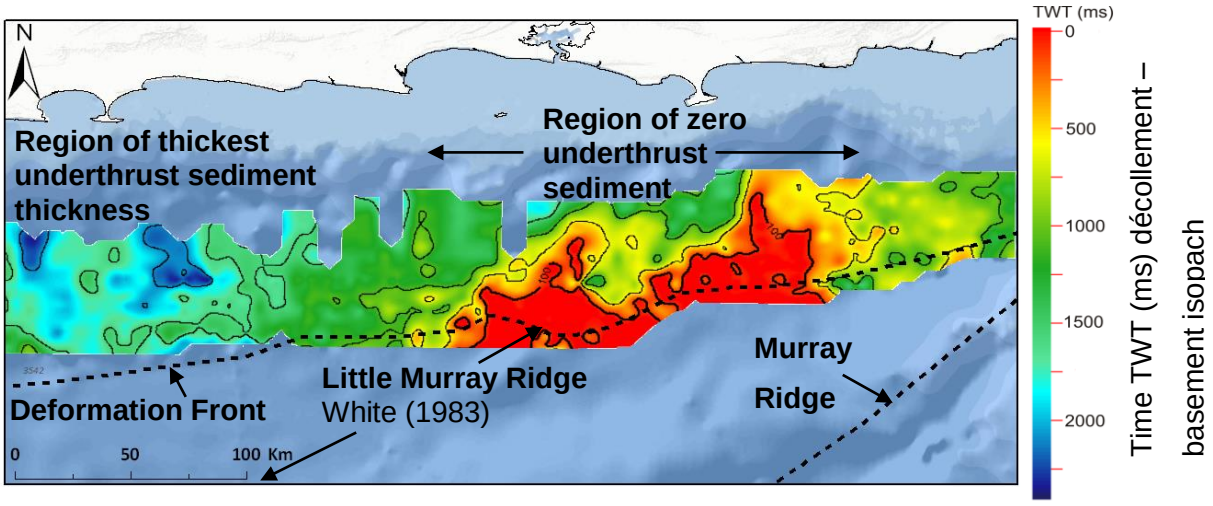

Figure 2.10. Décollement-basement isopach generated by gridding basement and décollement horizons and calculating thickness. Red indicates zero thickness between the two horizons i.e. no underthrust sediment. Green/blue colours indicate underthrust sediment thickness in TWT. Maximum thickness of underthrust sediment is 3-4 km in the westernmost area (assuming a sediment velocity of 4 km/s from Kopp et al.(2000)).

In the central study area, the incoming section is affected by the discontinuous basement highs of the Little Murray Ridge. This basement topography clearly influences the position of the décollement and the proportion of accreted sediment. Over the basement highs the décollement lies at the sediment-basement interface (Figure 2.6). The décollement does not appear to structurally step down along strike; rather it abuts and then follows the top-basement surface. In the landward prism it is possible that the décollement steps off the top basement surface and back into the sediment section, though this is difficult to interpret due to imaging limitations of this deeper section. In this region (~150 km along strike section of the margin) 100% of the incoming section (1-3.5 km) is currently being accreted at the deformation front (Figure 2.10).

2.3.5 Prism Taper Analysis

Surface slope values can be combined with the subducting plate dip to establish prism taper, and then used to elucidate information about the basal and internal frictional properties of the prism (Davis et al., 1983). A low taper suggests low basal friction relative to internal strength (Dahlen, 1990).

Slope and basement dip values were measured (using local depth conversions from velocity data for the latter) from the deformation front to 35 km into the prism (Table 2.1). The top-basement pick at the deformation front is clearly visible so has minimal error associated with it, however the landward picks are more difficult and so introduce an error of ±2.5%. There is additional uncertainty associated with the average velocities used for depth conversion which introduce an error of ~10%. The frontal 35 km is the maximum prism width covered by all of the lines allowing a comparison between consistent portions of the prism on each line. For completeness, taper along the lines which covered larger widths of prism (up to 70 km) was also calculated and gives a similar but slightly lower average taper of 3.7 °, compared to 4.5 ° for the frontal region.

Line No.	Slope°	Basement Dip°	Taper°
98	2.2	3.5	5.7
100	0.9	3.8	4.7
102	1.0	2.2	3.2
104	1.0	1.8	2.8
106	0.7	1.8	2.5
108	2.4	2.3	4.7
110	2.1	2.6	4.8
112	1.7	1.6	3.3
114	1.9	2.0	3.9
116	1.7	2.4	4.2
118	1.4	2.7	4.0
120	2.0	2.3	4.3
122	1.7	2.8	4.5
124	1.5	3.2	4.8
126	2.1	3.4	5.4
128	2.0	5.6	7.7
130	2.6	5.0	7.7
132	2.8	3.6	6.4
134	1.8	5.5	7.3
136	2.6	4.0	6.6
138	2.7	3.9	6.6
140	2.6	2.8	5.4
142	3.0	7.3	10.2
144	2.8	6.6	9.4
146	2.1	6.0	8.1
148	1.6	2.2	3.8
150	2.6	2.7	5.3
152	1.5	1.3	2.7
154	1.8	1.7	3.6
156	1.8	1.4	3.3
158	2.4	1.6	4.0
160	2.3	2.7	5.0
162	3.0	3.7	6.7
164	2.0	3.5	5.6
Average	2.0	3.2	5.2
Average excluding LMR values			**4.5**

Table 2.1. Slope and basement dip values calculated for the frontal 35 km of prism for each 2D seismic line. Values in red are excluded from regional average due to proximity to Little Murray Ridge (LMR) and resulting anomalously high (>5 °) basement dips. Line numbers increase from west to east.

Basal dip beneath the outer Makran prism is shallow; with an average value of 3.2 ° (Table 2.1). Our basement dips in the western region of 1.3 ° - 2.7 ° agree with results from refraction data of White & Loudon (1982b). Slope values are consistently low along strike, with a range of 0.7 ° - 3 °, and average of 2 °. Excluding regions of anomalous oceanic basement topography, the average taper is 4.5 °. This taper value is slightly higher than previous estimates of ~3.6 ° (Davis et al., 1983), although this

value was cited from White & Ross (1979), which focused on the western (Iranian) part of the accretionary prism. Our taper value however is similar to the ~5 ° calculated from the slope values of Kukowski et al. (2001) and basement dip values of Kopp et al *(2000).* Higher (>5 °) taper values are found in the central study area where the Little Murray Ridge is locally subducting (Lines 142 & 144 have both the highest slope and basal dip values), and to a lesser extent in the east where the Murray Ridge flank increases basement dip. The taper values for these lines are therefore elevated due to basement topography.

2.3.6 Fault Activity Analysis

Piggy-back basins in the hanging wall of a thrust fault contain sediment which onlaps the deformed, accreted hanging wall sediments of each fault. These basins contain growth packages, the geometry of which is related to fault activity. The sediments within the Makran piggy-back basins consist of turbidites and debrites from the failure of adjacent ridges, sediment transported by canyon channel systems and hemipelagic sedimentation (Bourget et al., 2010). These basins are generally 1-7 km in width (across strike), and can extend for over 50 km along strike. Many piggy-back basins contain >2 sTWT (~2 km) of sediment.

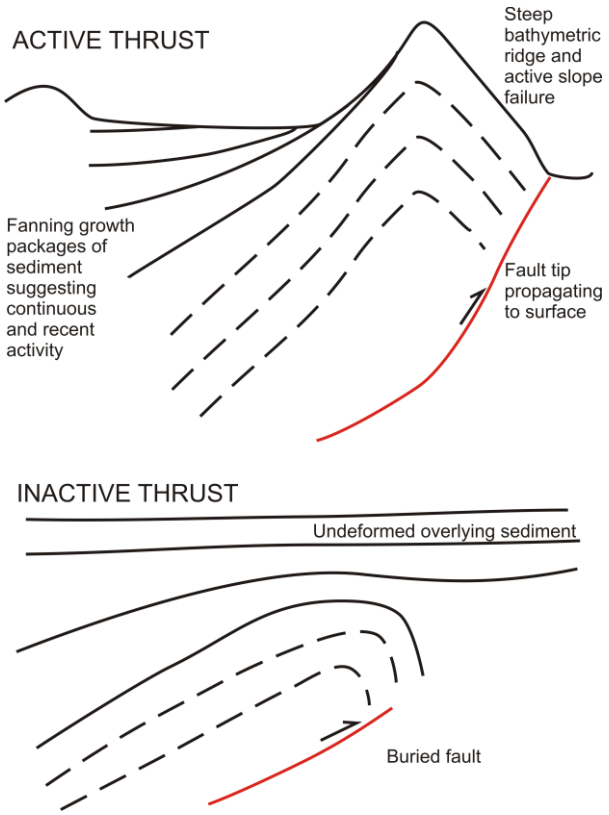

Figure 2.11. Schematic diagrams of active and inactive faults showing interaction between overlying sediment and underlying structure

Unconformities present in the piggy-back basins are the result of changes in the balance between sedimentation and tectonic activity, and may indicate changes in fault activity, changing fault position/geometry, or the initiation of a new thrust. Examples from the Kumano transect of the Nankai Subduction Zone illustrate that slope failure deposits may also create onlapping relationships and reflector terminations within piggy-back basin sediments (Strasser et al., 2011), generating complex stratigraphy. Fanning, wedge shaped growth packages of sediment are likely to indicate periodic or continuous syn-sedimentary activity on the underlying thrust fault which progressively tilts the piggy-back basin landward (Figure 2.11). Conversely horizontal recent sediments indicate minimal current fault activity. These classifications may be complicated by interactions between activity on adjacent faults, for example displacement on the frontal thrust may increase the dip of sediments in the piggy-back basin of the second thrust. Piggy-back basins have been identified on dip lines and the stratigraphy interpreted and correlated along strike (where

possible) to classify faults into currently active vs. inactive and continuously vs. intermittently active during the depositional history of the basins.

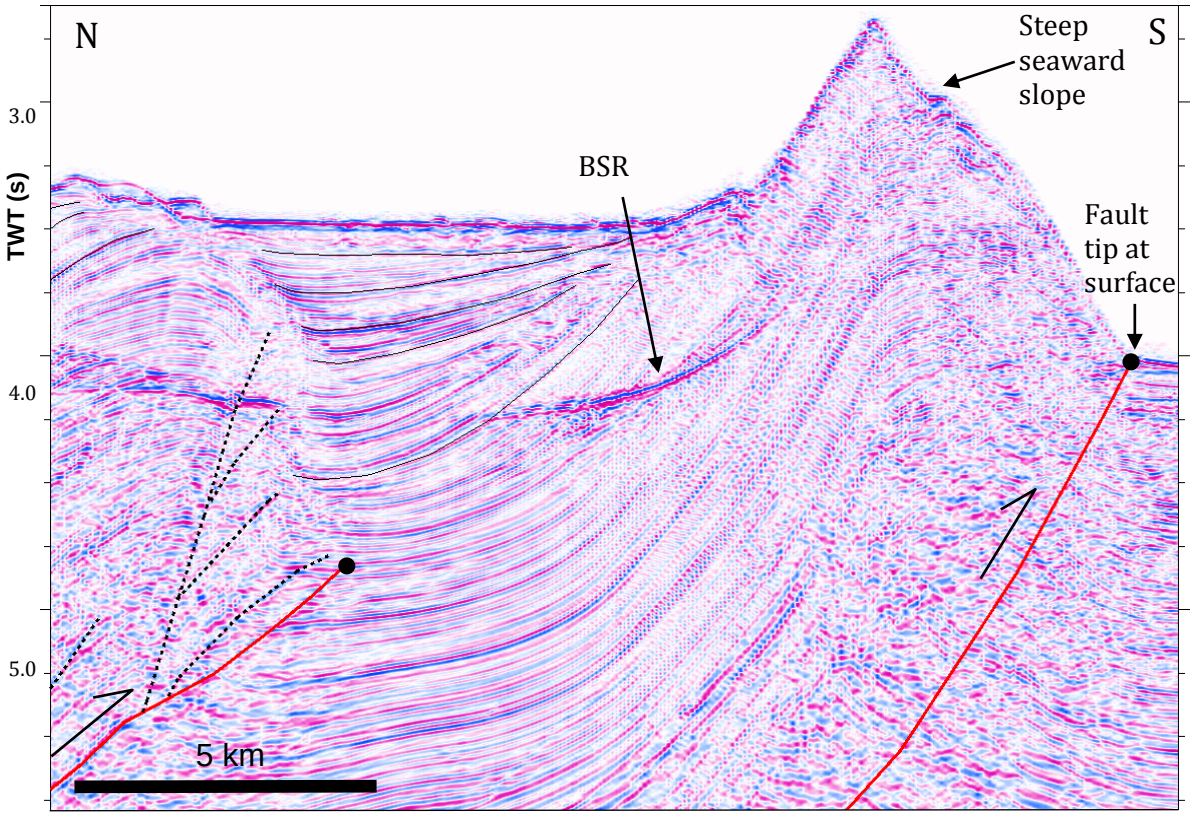

Figure 2.12. Example of an active fault. Piggyback basin shows sequential packages of fanning sediment indicating continuous activity. Thin black lines are interpreted piggy-back basin sediments. Location on Figure 2.3*.*

Applying these methodologies, over 75% of faults (from the deformation front to ~70 km landward) show evidence for recent activity (e.g. Figure 2.12), including some over 50 km from the deformation front. Inactive faults (no evidence for recent activity) are almost exclusively located towards the north of the study area (e.g. Figure 2.13). Clear variations in fault activity distribution are also observed along strike (Figure 2.14). In the easternmost Makran prism fault activity is limited to within 30 km of the deformation front (generally up to the ~4th thrust), and on the easternmost line only the frontal thrust shows evidence for recent activity. This contrasts with the western study area where up to 9 sequential prism faults appear to be currently active. These results show that in the west and central parts of the study

area, accretionary prism strain is currently being distributed over a ~50 km zone of the outer prism, rather than on a single, or small number of thrusts as in the east.

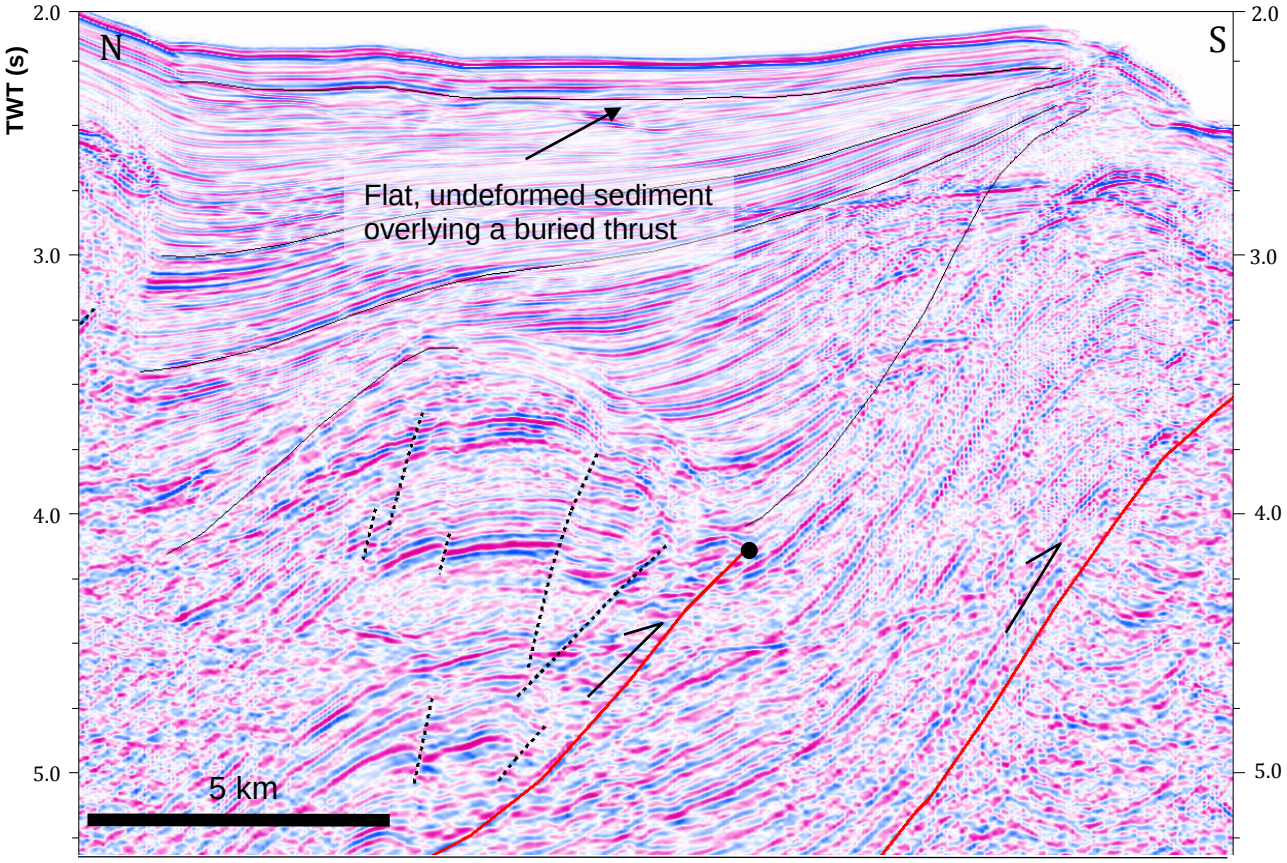

Figure 2.13. Example of an inactive fault. Thrust is buried beneath layers of undeformed sediment. Thin lines indicate interpreted piggy-back basin sediments. Location on Figure 2.3.

The faults are also classified into whether they have experienced continuous or intermittent activity. The seaward, younger thrusts (within 30 km of the deformation front/ the 3rd- 4th thrust) tend to demonstrate more continuous activity than the older, landward thrusts, where some appear to have had a period of quiescence (represented by undeformed, parallel strata) between active periods (Figure 2.14). This across strike variation in activity suggests that a given thrust fault is likely to be continuously active until ~30 km from the deformation front, where periods of quiescence are interspersed with renewed activity. In cases where there is a variation in activity along short sections of a thrust, the most common behaviour has been plotted. Variations in activity along strike of individual faults are generally related to

lower activity at the lateral tips of the fault, where displacement may be reduced, while increased displacement/activity occurs in the centre of the fault.

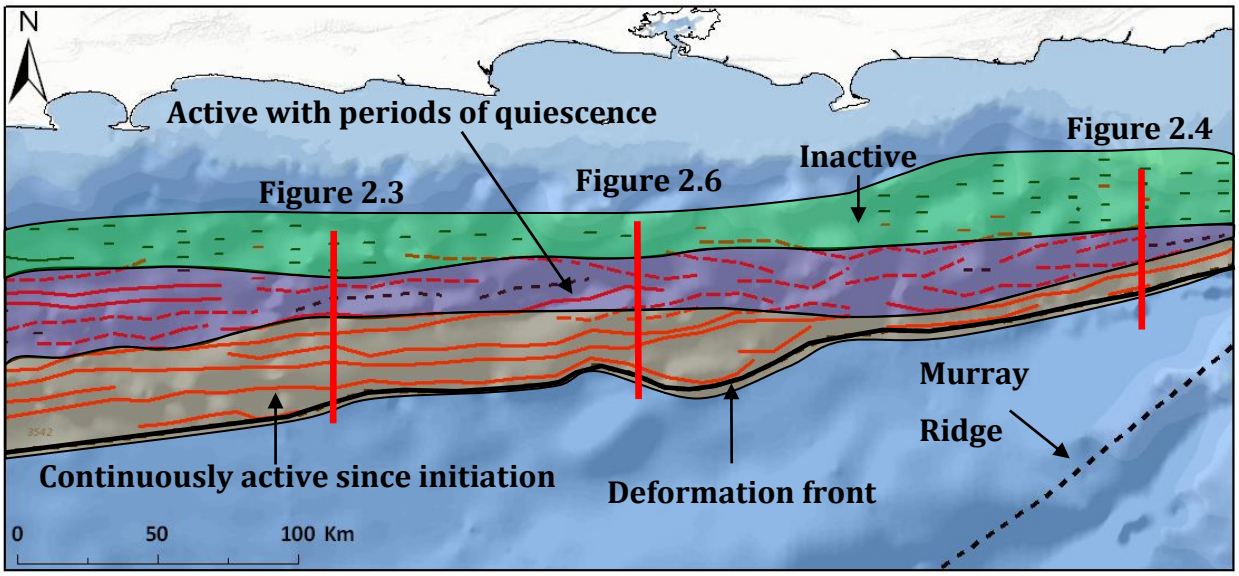

Figure 2.14. Plot of fault activity along/across the accretionary prism. Red faults show evidence for recent activity, black faults do not. Dashed faults show intermittent activity and those with solid lines appear to experience more continuous activity. The prism is divided into three zones based on this analysis: 1) Continuously active since initiation (orange), 2) Active with periods of quiescence (purple), & 3) Inactive (green).

There appears to be a correlation between fault length and level of activity (Figure 2.14). This is likely due to a combination of factors. The length over which a fault can be correlated increases with the bathymetric expression of the fault, due to increased recent activity and associated anticlinal growth. Faults of shorter length tend to have small or absent bathymetric expressions, related to their lack of recent activity and/or smaller displacements, and are therefore more difficult to correlate along strike creating the potentially artificial correlation between reduced fault length and inactivity.

2.4 Discussion

2.4.1 Prism structure and influence of the incoming oceanic plate section

From these analyses of the Makran margin, the outer prism appears to be relatively structurally homogeneous across and along strike at a regional scale (with the exception of local changes over the Little Murray Ridge). The structures seen across the margin are simple, with a consistent imbricate structure, which may be partly a function of the normal convergence (Kukowski et al., 2001). There is no evidence for large scale segmentation of the upper plate, changes in fault vergence, or major out-of-sequence thrusts and, with the exception of the region overlying the Little Murray Ridge, fault spacing and taper are very consistent along the margin. The extensive frontal thrust (length ≥ 250 km) further illustrates the continuity of the prism structures. Comparisons between accretionary margins by McAdoo et al. (2004) highlight the unusual simplicity and along-strike continuity of the Makran structure when compared to other margins such as Cascadia and Nankai. There is however a gradual change in prism characteristics towards the eastern extent of the subduction zone: with increasing proximity to the Murray Ridge and the Eurasian/Arabian/ Indian triple junction, the deformation front begins to rotate to the north and strain becomes more focused in the outermost prism. The subduction of the Little Murray Ridge also causes local changes in fault spacing and reduces the incoming sediment thickness to less than 1 km.

To investigate how the thick accreted sediment section of the Makran affects two of its structural parameters (taper and fault spacing), the results from this study have been compared with those from other margins with significant accretionary prisms: Lesser Antilles, North & South Hikurangi, Cascadia and Nankai (Table 2.2). What is evident from this comparison is that, despite its high sediment input, the taper and fault spacing of the Makran are comparable to these other margins, suggesting that the high incoming sediment thickness of the Makran is not generating unusual structural behaviour in the offshore prism and is not the main control on structural development. The Makran, with an accreted sediment thickness of ~6 km, has similar fault spacing to N Cascadia (Washington) where the accreted section is only 2-3 km.

However, there does appear to be a potential lower cut-off of <1 km accreted sediment, below which the fault spacing drops to low values (3-4 km) such as in Nankai (Muroto) and possibly North Hikurangi (Table 2.2). An alternative interpretation for fault spacing in the Makran is proposed by Ding et al. (2010), who suggest that the primary fault spacing is 12 km, and that faults which form within this across-strike span are secondary, out-of-sequence thrust faults. We find no categorical evidence from our dataset for such regular out-of-sequence thrusting, or any clear distinction between 'primary' and 'secondary' thrusts, however uncertainties in the exact sequence of faulting should be noted as a possible source of error in the fault spacing measurements as a function of their spacing at initiation.

		Taper values (°)			
	Max accreted sediment thickness at trench (km)	**Surface slope (α)**	**Basement dip (β)**	**Taper (α+β)**	**Average fault spacing (km)**
Makran *This study*	6	2 (avg.)	1.5- 2.5 (avg.)	3.5 - 4.5	6
Southern-Central Lesser Antilles (13.5°N) *Bangs et al. (1990)*	5	2	1	3	8
Hikurangi (South-Central) *Barnes et al. (2010)*	2-4	1	3.0	4	5-6
North Cascadia (Washington) *Adam et al. (2004)*	2	2	1.8	3.8	6
Hikurangi (North) *(Barker et al., 2009)*	0-1	3	8	11	~3 (Frontal 3 thrusts)
Nankai (Muroto) *Gulick et al. (2004)*	0.7	1.5	1.6	3.1	4 *Ikari & Saffer (2011)*

Table 2.2. Comparison of structural parameters calculated for the Makran from this study, with published data from selected other margins. Where fault spacing is ambiguous, spacing between thrust anticlines has been used.

The average prism taper of the Makran, without the effects of the Little Murray Ridge is 4.5°. This classes it as a low taper margin among global subduction zones, comparable to Southern-Central Lesser Antilles, Southern Hikurangi & Cascadia-Washington (Lallemand et al., 1994). According to Coulomb tapered wedge theory, the low taper of the Makran is likely to indicate either a weak basal surface, or high internal strength (Davis et al., 1983). However, analogue models have suggested that accretionary prisms which experience very high sediment input may have mechanical differences to classic Coulomb wedges and may be prevented from reaching the critical taper their basal friction would predict, forming sub-critical wedges (Storti and McClay, 1995). Therefore the Makran may represent an example of a sub-critical wedge which is actively deforming in response to high levels of frontal accretion. This mechanism has also been suggested for the Southern Hikurangi margin, which experiences a similarly low taper (4 °) and high rates of frontal accretion (Barnes et al., 2010).

2.4.2 Fault Activity Analysis

Fault activity analysis indicates that much of the outer Makran accretionary prism is currently deforming, with strain distributed over a ~50 km wide region of the prism, and up to 9 imbricate thrusts in the offshore portion. Our analysis suggests that a given thrust in this environment will be continuously active until approximately 30 km from the deformation front (3rd - 4th thrust), when it will begin to experience periods of inactivity, and then will likely become fully inactive ~50-60 km from the deformation front. It is not possible here to establish the activity of the onshore portion of the prism, though it has been suggested that active folding and faulting also occurs in this region (Farhoudi and Karig, 1977, Platt et al., 1988). Our analysis divides the outer prism into three zones across strike, a seaward continuously active zone, a central intermittently active zone and a landward predominantly inactive zone (Figure 2.14). Detailed studies of fault activity in active accretionary prisms are relatively rare; however published analysis of the Nankai Muroto 3D volume indicates that the majority of prism thrusts retain some level of activity seaward of the out-of-sequence thrust (~35 km from the deformation front), with increased

recent relief on the frontal 5-6 thrusts (Gulick et al., 2004). As a further example, in the onshore imbricate fault system of Taiwan, GPS data indicate that maximum deformation is concentrated in a frontal zone ~15 km wide, but that moderate deformation continues across the prism (Chang et al., 2003).

The thick input section of the Makran, the majority of which is accreted, and the moderate convergence rate (~4 cm/yr) imply that frontal accretion rates will be high. This may require enhanced deformation across a wider region of the prism relative to other margins. Diffuse fault activity may also be a result of low basal friction: analogue models (Koyi et al., 2000) suggest that fold-thrust belts which form over a low basal friction décollement are more prone to sustained activity over a broad region than those which form over a high basal friction surface. It is also important to consider the scale of the Makran subduction zone. At ~400 km wide, it is the widest accretionary prism on earth, and therefore may be expected to have a wider active prism toe than narrower prisms if the active prism occupies a certain fraction of its total width. The division of the accretionary prism into three discrete zones of activity is similar to what is produced by analogue models (Hardy et al., 1998, e.g. Lohrmann et al., 2003). The intermittent activity of the central zone thrusts may be in response to changes in accretion or sedimentation rate, for example an increase in the rate of frontal accretion may trigger increased deformation as the prism deforms to reach/maintain its critical taper (Lohrmann et al., 2003). The reduction in fault activity in the east of the study area may be due to increased sediment blanketing (as observed from our MCS data), which has been suggested by analogue models to inhibit fault reactivation through increasing the normal stress on the fault (Storti and McClay, 1995, Hardy et al., 1998, Bigi et al., 2010). The proximity of the Murray Ridge triple junction and onshore strike-slip systems may also act to reduce fault activity in the east.

2.4.3 Response of the décollement to subducting basement topography

The position of the décollement affects many aspects of subduction zone dynamics (Moore, 1989, von Huene and Scholl, 1991, Saffer and Bekins, 2006). The proportion

of sediment subducted is important for global sediment budgets while the stratigraphic position of the décollement will affect its shear strength, and hence its development and seismogenic behaviour. For the majority of the E. Makran Subduction Zone, the décollement is located within the sediment section, with along-strike variations in the thickness of underthrust sediment as shown in Figure 2.10. In the central section where the Little Murray Ridge intersects with the deformation front, the décollement forms at the basement-sediment interface, accreting the entire (albeit thinner) sediment section. As a result, 100% of the incoming sediment is accreted in this region. The same phenomenon has been observed on the Northern Hikurangi margin where the décollement position changes from within the sediment to the basement-sediment interface where a seamount is being subducted (Barnes et al., 2010, Bell et al., 2010).

2.4.4 Implications for décollement properties and prism mechanics

The Makran can be characterized as a fluid and sediment rich margin, supported by its low prism taper (4.5 °), high sediment input (up to 7 km), and evidence for fluids. The identification of a BSR, fluid seeps, bubble plumes and regions of high backscatter in sidescan sonar data (likely seafloor carbonate crusts at cold seep sites) across the prism suggest that although dewatering must be significant due to compaction in the input section and accretion in the outermost prism, significant fluid and fluid flux persist throughout the prism (Spiess, 2007, Ding et al., 2010). These fluids also form mud volcanoes both offshore and onshore, suggesting a degree of overpressure (Schluter et al., 2002). Velocity-porosity conversions along the Cam-30 Profile (Fruehn et al., 1997) showed no significant evidence for overpressure in the incoming section, but increased porosity and slight inferred overpressure at depth landward of the deformation front. Similar conclusions were reached by Fowler et al. (1985) who noted from sonobuoy data that a high degree of tectonic consolidation occurs at the prism toe, where the incoming section is initially deformed. The normally compacted nature of the incoming sediment section (Fruehn et al., 1997) may be due to the presence of permeable layers in the sediment which facilitate vertical fluid loss and compaction, enhanced by the presence of widespread normal faults. It is important to

note that overpressure measurements from velocity models are for the bulk sediment volume, and will therefore not resolve localized overpressure variations at a discrete horizon (e.g. the décollement).

The potential effects of a thick sediment section, such as in the Makran Subduction Zone, on pore pressures are debated. On the one hand, thicker sediment is likely to suggest a higher sedimentation rate, which could increase pore pressures if sedimentation rates prevent sufficient fluid expulsion, alongside reduced vertical permeability due to increased drainage length (Saffer and Bekins, 2006). Conversely high sedimentation may indicate a higher proportion of coarser sediment, with likely increases in overall permeability (although not necessarily vertically) and hence reduced pore pressure. It is likely that reduced vertical permeability and insufficient fluid expulsion dominates, as margins with thick incoming sections (e.g. Southern Lesser Antilles, South Hikurangi) tend to be characterized by low taper angles indicative of high basal fluid pressures (Dahlen et al., 1984).

Low taper, fluid-rich subduction zone forearcs are often inferred to have weak basal surfaces, commonly observed as high-amplitude, negative polarity décollement reflectors in seismic data suggesting reduced bulk density, increased porosity and likely increased pore fluid pressure (e.g. Moore et al., 1995, Zhao et al., 2000, Bangs et al., 2004). Prism fault geometry analysis of Kukowski et al. (2001) suggest that the décollement in the Makran is >3 times weaker than the overlying prism sediments, however they also note that the slight observed overpressure (Fruehn et al., 1997) may only account for ~30% of the inferred décollement weakness, with the remainder a function of lithology or fracturing. The observed overpressure may also be distributed through the lower sediment section, rather than being concentrated at a particular interface (such as the décollement).

The décollement in the E Makran appears to be unreflective in seismic reflection data across the study area, which is unexpected considering other prism characteristics which may suggest a weak décollement. Kopp et al. (2000) point out a high amplitude horizon deep in the input section in the west of the study area on one seismic profile but this is a localized feature and there is no clear indication that this represents the

pre-décollement horizon. High amplitude, negative polarity reflectors may either be indicative of a discrete décollement horizon with specific properties, or be due to an impedance contrast between the accreted and underthrust sediment, and ordinarily these two cannot be distinguished. On the Muroto Nankai transect fluid overpressure and associated reduction in effective stress in the underthrust section were observed from drilling and direct sampling up to 20 km landward of the trench, in a region of high décollement reflectivity in seismic data (Tobin and Saffer, 2009).

The high sediment velocities at the base of the Makran sedimentary section (Fruehn et al., 1997, Kopp et al., 2000) may imply that there is an insufficient velocity contrast between the accreted and underthrust sediment to form a coherent reflector. The Makran has the thickest accreted sediment section of any accretionary margin, and it is therefore difficult to compare with other localities in this respect, however, seismic reflection data from the Southern Lesser Antilles accretionary prism (where the incoming section is ~4 km thick) also show little velocity contrast between accreted and underthrust sediment, though the reflectivity of the décollement here is unclear (Bangs et al., 1990). However, data from the Sumatran margin show similarly high (>4 km/s) velocities to the Makran in the lower sediment section, and do resolve a high amplitude, negative polarity basal surface (Dean et al., 2010).

The Makran therefore represents an intriguing contradiction between evidence for overpressure, and a weak basal surface, with an unreflective décollement. These observations might be explained by a weak décollement which is either fluid rich, but not producing a reflector in the MCS data, or not fluid rich, but weak due to other sediment properties which also do not produce a significant impedance contrast. However, these explanations do not truly provide an adequate explanation of the seismic properties observed when compared with other margins and datasets. These results may instead be explained by a sub-critical taper which therefore may not reflect basal strength, and distributed overpressure through the thick accreted sediment section, rather than at a discrete horizon. In this scenario the décollement in the Makran may be stronger than expected.

2.4.5 Implications for seismogenic potential

The high velocities (<4.4 km/s) observed in the deepest (>5 km) sediments of the Makran accretionary prism may indicate that the sediments at décollement level are sufficiently consolidated to support seismic rupture. These sediment velocities are comparable to those seen at depth in the southern December 2004 Sumatra rupture area (Dean et al., 2010) where shallow/seaward rupture beneath the prism has been suggested. As discussed above, the basal surface itself may also be stronger than expected, therefore increasing the potential for seismogenic rupture beneath the outer forearc, with implications for tsunamigenesis. Our MCS data show that the structures seen in this portion of the Makran are fairly homogenous along strike and show little evidence for large scale segmentation (although the basement topography of the subducting Little Murray Ridge may affect the outermost prism). Integrating all evidence, it therefore seems reasonable to suggest that the low level of seismicity currently seen in the Makran could be a reflection of a long recurrence interval of plate interface earthquakes, and short historical record, rather than simply due to aseismic subduction, and that there may be a significant seismogenic potential. The occurrence of the 1945 and 1947 earthquakes, and reports of previous historical events (Byrne et al., 1992) emphasizes this point. This discussion illustrates how an increased knowledge of the Makran through a systematic, spatially extensive investigation of prism structure, can help to elucidate information regarding seismogenic potential.

2.5 Conclusions

1. The structure of the Eastern Makran Subduction Zone, with the exception of the region immediately overlying the Little Murray Ridge and other local variations, is consistent at a regional scale, with a relatively simple seaward verging, evenly spaced imbricate thrust structure. Despite its high sediment input, the taper and fault spacing of the Makran are comparable to margins with significantly thinner incoming and accreted sediment sections. The high accreted sediment thickness does not appear to affect fault spacing, suggesting that there may be an upper limit on fault spacing in imbricate thrust systems.

2. Fault activity is distributed across up to 9 imbricate thrusts (over a 50 km region) in the outer prism. The outer prism can be divided into three zones according to fault activity: frontal continuous activity, central intermittent activity and landward inactivity. These zones narrow to the east with increasing proximity to the Murray Ridge and triple junction, with only a single active thrust on the easternmost survey lines. These results suggest that deformation in accretionary prisms may be more widely distributed than previously suggested, especially at low taper/high sediment input margins.
3. The average taper of the Makran accretionary prism is low (~4.5 °). This taper is likely to be a reflection of low basal strength and overpressured deep sediments; however the Makran may also have developed as a sub-critical wedge, where the prism is actively deforming but unable to reach its critical taper due to high rates of frontal accretion and sediment input.
4. The décollement is located within the lower sedimentary unit (Unit A) except in the vicinity of the Little Murray Ridge where it steps onto the top-basement horizon, accreting 100% of the incoming sediment section. The décollement is neither high amplitude nor negative polarity (it is unreflective), which is surprising as reflective décollements have been observed in the seaward parts of several other accretionary margins, particularly those with low taper and high sediment input, where they have been inferred to represent a weak, overpressured basal surface. Other evidence from the Makran (porosity – depth trends, mud volcanoes, low taper etc.) also supports a degree of overpressure and potentially weak basal surface; however these observations may also be explained in the context of a stronger décollement. If the Makran décollement is stronger than expected, then this may go some way to explaining the presence of historical seismicity in the offshore prism, and have important implications for seismogenic potential.
5. This study is the first of its kind on the Makran margin to examine accretionary prism deformation over a large along-strike (~400 km) section and represents one of only a small number of systematic studies of active prism structure over a large proportion of a single subduction margin. Our results indicate how prism structure responds to subducting basement

features and sediment input, describes distribution of deformation, and may be important for the assessment of seismogenic potential.

Acknowledgements

The authors would like to thank WesternGeco for providing the seismic reflection data. We would also like to thank the crew and scientists of Meteor Cruise 74 (Leg 2) for the collection of the bathymetry data and allowing access to the data, and Tim Minshull for helpful discussion. We thank Oliver Ralph for a useful preliminary analysis of the data. We thank the Associate Editor and reviewers Sean Gulick and Nina Kukowski for their helpful comments on the manuscript.

2.6 Supplementary material

This dataset presents two additional reflection seismic lines for the Makran Accretionary Prism collected by WesternGeco® in 1998-1999. Figure S1 shows the line locations. Figure S2 is a 2D seismic reflection line located in the west of the study area. Figure S3 is a 2D seismic reflection line located in the east of the study area. The accompanying text describes the figures and their interpretation.

Accompanying text

Figures S2 and S3 help to represent the similarities and variability in structure along the Makran margin when compared to Figures 2.3, 2.4 and 2.6 in the main text. Figure S2, located in the western region of the study area, shows a simple imbricate structure with a contrasting frontal fault/fold morphology relative to Figure 2.3. The fault spacing on this line is ~6 km. The décollement is located within the lower sediment section, accreting a thickness of 4.5 km. Figure S3 is located to the east of the Little Murray Ridge basement high and has a thinner incoming sediment section of ~4 km, of which ~3.5 km is being accreted. The geomorphology of the prism in the east is more affected by recent slope sedimentological processes, as is visible from sediment blanketing (Figure S3). A proto thrust is also visible on this line which has not yet developed an anticlinal fold, showing an early stage of frontal thrust evolution.

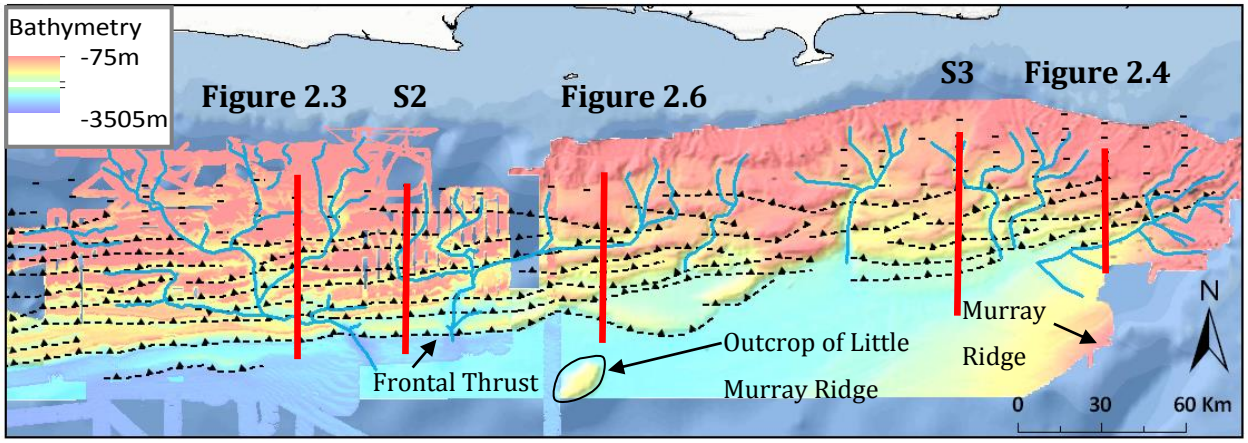

Figure S1. Structure map of the Makran accretionary prism with locations of Figures S2 and S3 shown. Imbricate thrust faults picked from MCS data and correlated with the aid of bathymetry data. Bathymetry data in east modified from Bourget et al.(2010).

Submarine canyon-channel systems in blue. Water depth seaward of the deformation front ~3500 m.

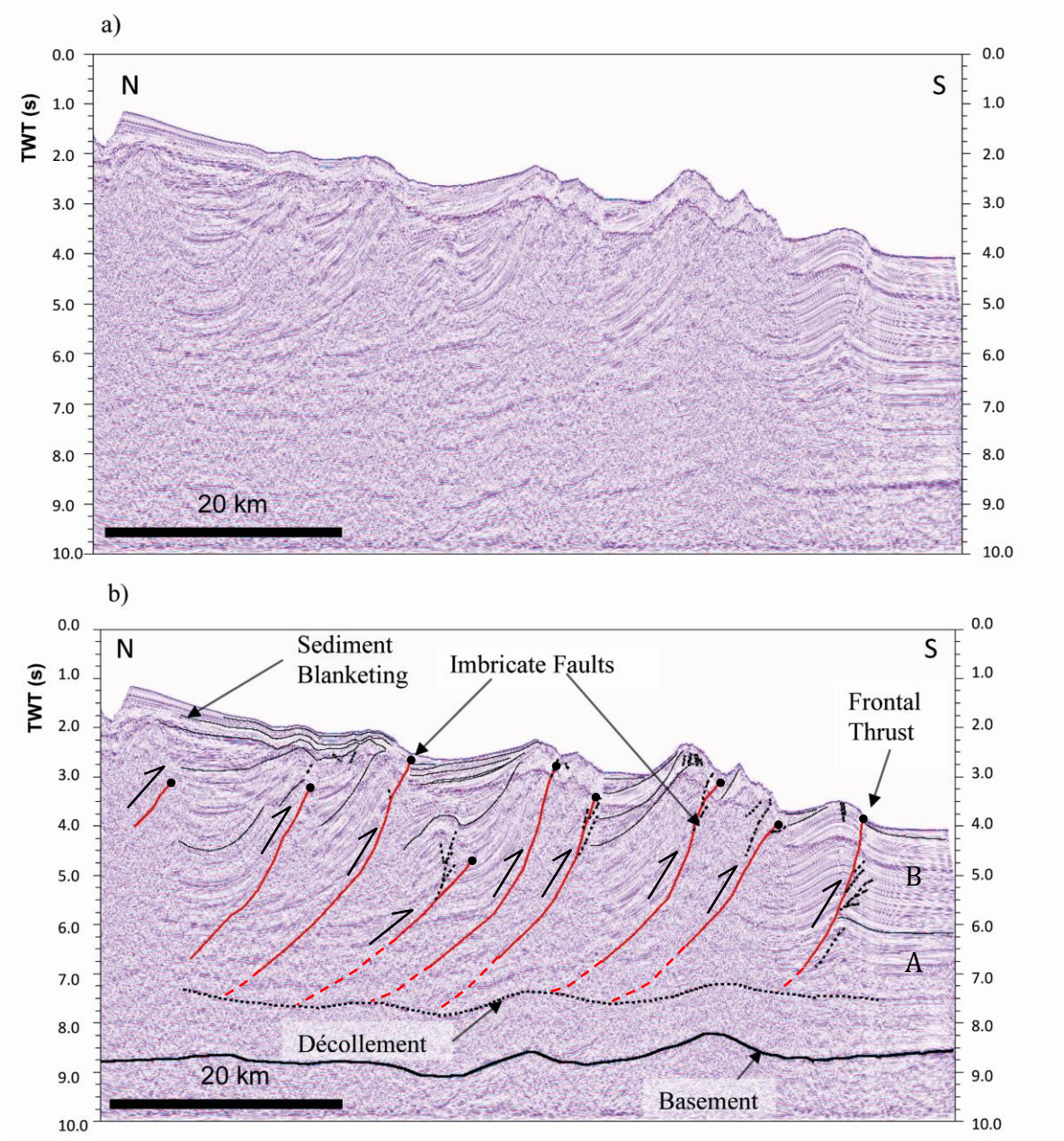

Figure S2. Seismic line 122 from the west of the study area. Location on Figure S1 a) without interpretation, b) with interpretation. Simple imbricate structure visible, with an average fault spacing of ~6 km. Increased sediment blanketing can be seen towards the north. Incoming sediment thickness of 6 km. Width of view ~70 km. Vertical exaggeration x2.5 at seafloor.

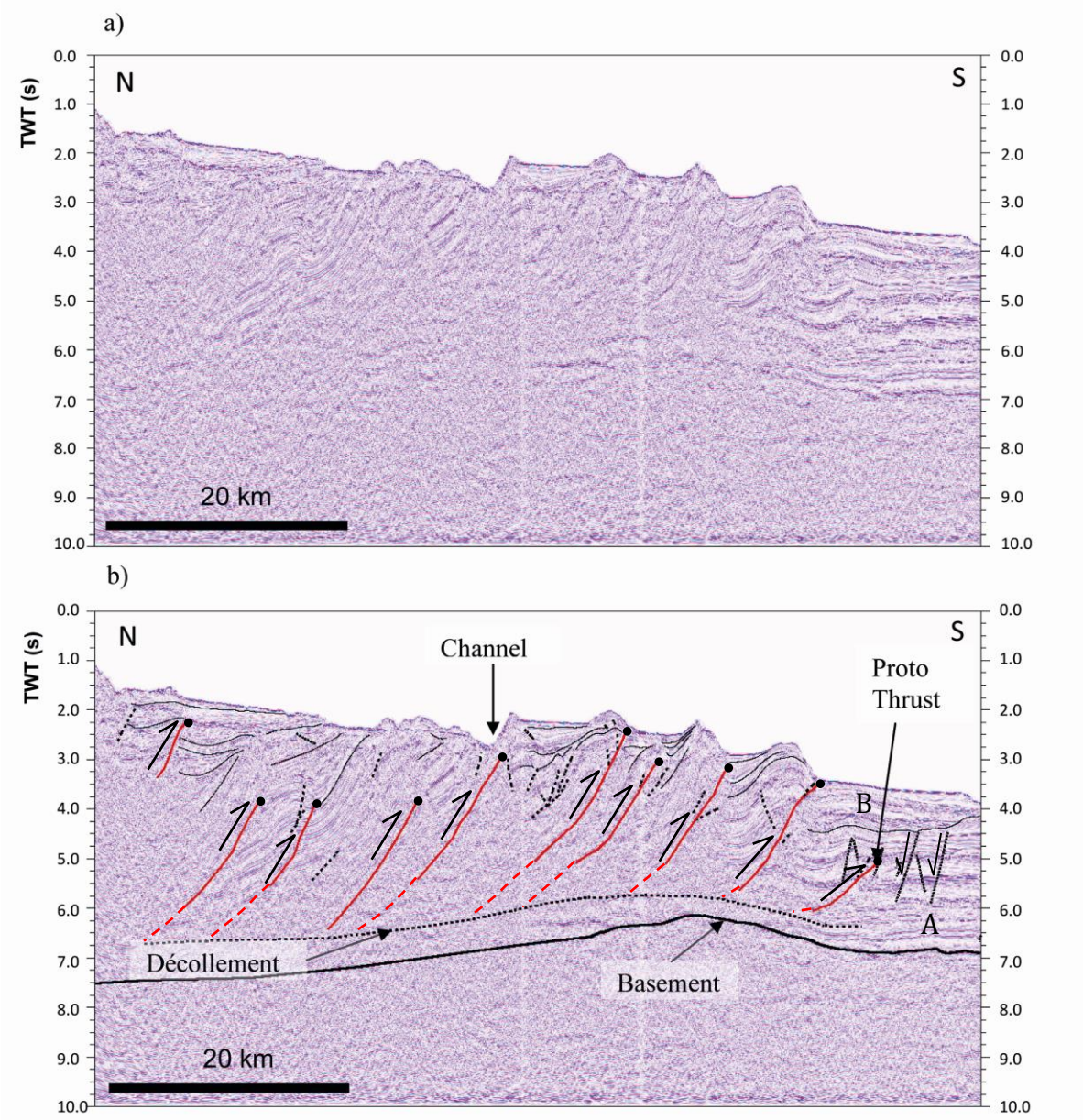

Figure S3. Seismic line 160 from the east of the study area.Location on Figure S1 a) without interpretation, b) with interpretation. Increased sediment input and channel structures visible. The unconformity separating units A and B is also visible in the incoming section. Incoming sediment thickness of 4 km. Width of view ~70 km. Vertical exaggeration of x2.5 at seafloor.

3 Chapter 3. Thermal structure and megathrust seismogenic potential of the Makran subduction zone

This chapter is a reproduction of an article accepted for publication in Geophysical Research Letters in 2013 - *Smith, G., L. McNeill, K. Wang, J, He, and T. Henstock (2013). Thermal structure and megathrust seismogenic potential of the Makran subduction zone, Geophysical Research Letters, 40, doi:10.1002/grl.50374*

Thermal model (PGCtherm2D) written and developed by Jiangheng He. Model geometry for the Makran generated by Jiangheng He with data provided by Gemma Smith. Other model parameters provided and input by Gemma Smith. SEDTEM 1D code for oceanic geotherm developed by Kelin Wang who also provided extensive guidance and assistance in developing and running the model for the Makran. Running the model, data extraction, analysis and write-up completed by Gemma Smith. All authors provided helpful feedback and discussion.

Thermal structure and megathrust seismogenic potential of the Makran subduction zone

Gemma L. Smith[1], Lisa C. McNeill[1], Kelin Wang[2], Jiangheng He[2], Timothy J. Henstock[1]

[1] Ocean and Earth Science, National Oceanography Centre Southampton, University of Southampton, Southampton, SO14 3ZH, U.K.

[2]Pacific Geoscience Centre, Geological Survey of Canada, 9860 West Saanich Road, Sidney, British Columbia, V8L 4B2, Canada

Abstract

The Makran Subduction Zone experienced a tsunamigenic M_w 8.1 earthquake in 1945 and recent, smaller earthquakes also suggest seismicity on the megathrust, however its historical record is limited and hazard potential enigmatic. We have developed a 2-D thermal model of the subduction zone. The results are twofold: 1) The thick sediment cover on the incoming plate leads to high (~150°) plate boundary temperatures at the deformation front making the megathrust potentially seismogenic to a shallow depth, and 2) the shallow dip of the subducting plate leads to a wide potential seismogenic zone (up to ~350 km). Combining these results with along-strike rupture scenarios indicates that M_w 8.7-9.2 earthquakes are possible in the seaward Makran Subduction Zone. These results have important earthquake and tsunami hazard implications, particularly for the adjacent coastlines of Pakistan, Iran, Oman and India, as the Makran has not been previously considered a likely candidate for a M_w>9 earthquake.

3.1 Introduction

The position of the updip and downdip limits of subduction zone megathrust rupture controls earthquake magnitude and the intensity of shaking and tsunami in coastal regions. These limits are believed to be thermo-petrologically controlled (Hyndman and Wang, 1993), and so can be investigated through studying the thermal structure

of a given subduction zone (e.g. Hyndman and Wang, 1993, Hyndman et al., 1995, Oleskevich et al., 1999, Klingelhoefer et al., 2010). Studies of this nature can be highly informative for seismogenic potential and resultant hazard assessments, especially at margins where background seismicity is low and/or the historical record is limited, such as the Makran.

The Makran Subduction Zone is located offshore Pakistan and Iran in the Arabian Sea. The Arabian plate is subducting beneath the Eurasian plate at ~4 cm/yr (DeMets et al., 2010). The age of the incoming Arabian plate is debated due to a lack of identifiable seafloor magnetic anomalies, but has been estimated as either 70-100Myr (Whitmarsh, 1979) or 50-60Myr (Mountain and Prell, 1990). Heat flow data (Hutchison et al., 1981) support the older age, and we use this for our calculations. The incoming plate has a thick overlying sediment section of up to 5-7 km, the majority of which is accreted forming a wide (>200 km) accretionary prism with a low taper of ~4.5° (Smith et al., 2012).

The Makran has low historical seismicity, which has made estimating its seismogenic potential problematic. Compilations of historically reported events in the Makran have suggested a possible recurrence interval of 100 – 200 years for $M_w > 8$ earthquakes (Byrne et al., 1992; Heidarzadeh et al., 2008), with the most recent occurring in 1945 (M_w 8.1). This event, modelled as a shallow thrust plate boundary event, caused a tsunami that killed over 4000 people. Its location has been recalculated with significant variations in estimated location (~100 km of latitude) and depth (~10 km) (Heidarzadeh et al., 2008). We use the ISC (International Seismological Centre) location (placing it offshore), but it should be noted that a more landward (northerly) epicentre has also been suggested (Byrne et al., 1992). Subsequent thrust fault seismicity is concentrated between the region of the 1945 event and the coastline, with few events exceeding M6 (Figure 3.1).

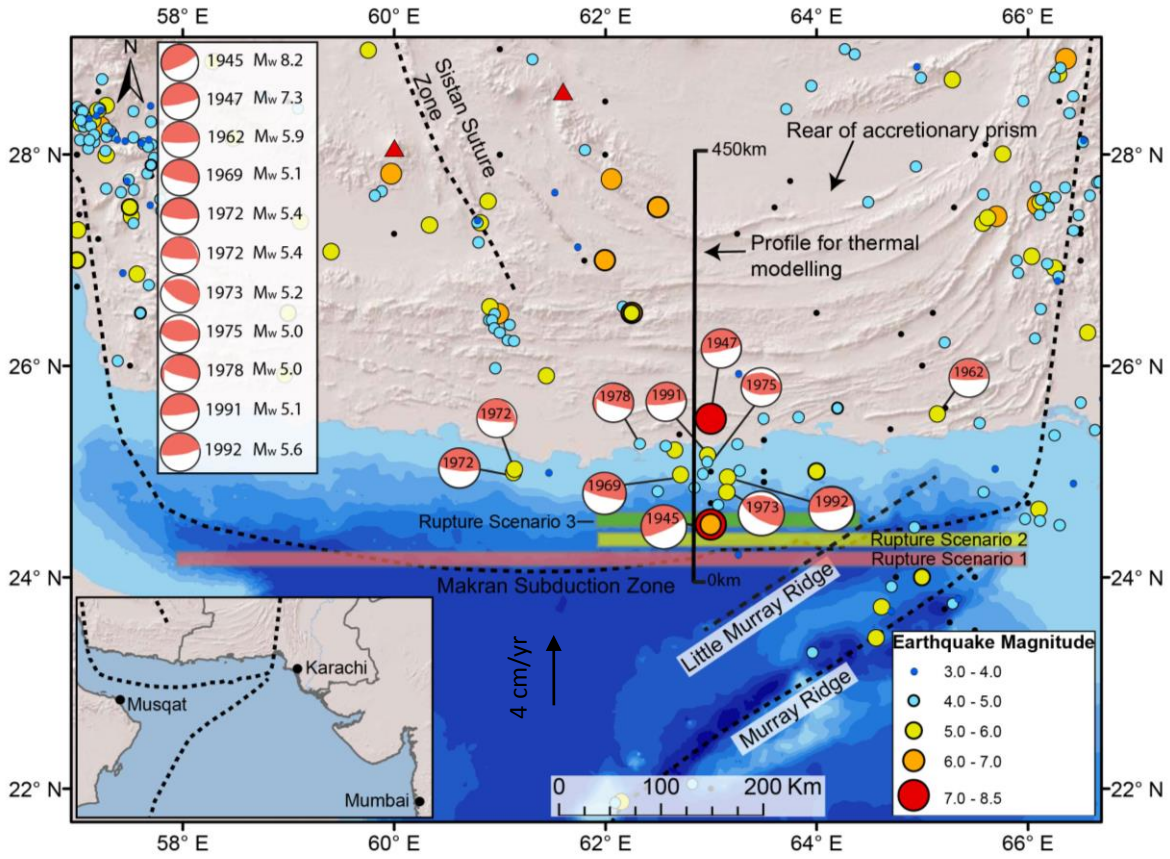

Figure 3.1. Location map of the Makran Subduction Zone. Earthquakes from post-1960 (and pre-1960 with assigned magnitudes) from the EHB Catalog (Engdahl et al., 1998) are illustrated by circles. Those from pre-1960 with no assigned magnitude are small black dots. Significant, possible plate boundary events with focal mechanisms from Byrne et al. (1992) and the Global CMT Catalog (magnitudes in inset table). 1945 earthquake location is from the ISC catalogue. Bathymetry is from the GEBCO_08 Grid (Smith and Sandwell, 1997). Strike lengths of three rupture scenarios for magnitude calculations are indicated by shaded bars. The thermal modelling profile is marked as a black line. Triangles are volcanoes.

A key question is how a M8^{+} earthquake with a likely plate boundary origin (1945) was generated beneath the Makran outer prism, when the prism is often inferred to be aseismic due to unconsolidated sediment (Byrne et al., 1992). It is possible that the deepest input sediments, where the plate boundary décollement forms, may be sufficiently lithified to support seismogenic rupture (Fruehn et al., 1997, Smith et al., 2012). The Makran also has a shallow dipping megathrust (~2°) (Smith et al., 2012),

which may increase coupling and facilitate high-magnitude earthquakes (Gutscher and Westbrook, 2009).

3.1.1 Constraints on earthquake rupture area

The shallowest portion of the plate interface (upper 5-10 km) is traditionally thought to slip in a velocity-strengthening fashion (Byrne et al., 1988, Hyndman et al., 1997, Wang and Hu, 2006, Saffer et al., 2012). This view has been challenged by earthquakes such as 2004 Sumatra-Andaman and 2011 Tohoku-Oki, with both showing evidence for locally shallow rupture (Chlieh et al., 2007, Fujiwara et al., 2011, Gulick et al., 2011). It has been suggested that, although large magnitude earthquakes may not initiate in this shallow region, ruptures which initiate deeper on the plate boundary may propagate to shallow depths (Hu and Wang, 2008). The resulting wide and shallow rupture increases the tsuanmigenic hazard associated with the earthquake. The downdip limit of very large ruptures has been proposed to occur at the intersection with the forearc mantle if hydrated mantle material is present (Peacock and Hyndman, 1999). If the downgoing plate is very warm, the limit may occur at a shallower depth where the plate boundary reaches temperatures of ~350°C to ~450°C (Oleskevich et al., 1999, Hyndman and Peacock, 2003).

The along-strike rupture length may be influenced by the subduction of topographic basement highs such as oceanic ridges and seamount chains. Basement features have been proposed to either prevent rupture propagation or to initiate rupture (Wang and Bilek, 2011). The Makran may be seismically segmented along its length into a western and an eastern segment, distinguished by contrasting levels of seismicity (lower in the west), and separated by the Sistan Suture Zone, an onshore strike-slip feature of the continental Eurasian Plate (Figure 3.1). In addition to this large-scale potential segmentation, the subduction of the Little Murray Ridge in the eastern Makran (Figure 3.1) may influence rupture propagation. These features will be included in our magnitude calculations to provide different rupture length scenarios.

3.2 Thermal Modelling Method

To estimate the thermal structure of the Makran subduction zone, we construct a steady-state two-dimensional finite element model using the PGCtherm2D code developed by one of the authors (JH) and previously used by, *e.g., Wada and Wang* (2009). Where we developed the model transect (62.9°E), the average convergence velocity is 4 cm/yr, and the sediment thickness is 7 km, of which 5 km is accreted and 2 km underthrust (Smith et al., 2012). The boundary conditions of our model are 0°C at the top surface and 1450°C at the base of the subducting slab. Because the thermal structure of the subduction zone is controlled mainly by the advection of the temperature profile of the incoming plate, where to place the base of the slab is unimportant (Wang et al., 1995). The seaward side of the model is defined by a geotherm generated with the SEDTEM 1D finite element code of *Wang and Davis* (1992) for the cooling oceanic lithosphere and overlying sediment. As sedimentation rates in the deep Makran section remain poorly constrained, low (~0.1 mm/yr), constant sedimentation rates were used to generate the 7 km sediment section based on the average basement age, whilst matching the observed average heat flow (42.6 mW m^{-2}) in the incoming section (Hutchison et al., 1981). Oceanic plate age was taken as 85Myr (midpoint of 70-100Myr: estimate of Hutchison et al, 1981), but the thermal state of the oceanic plate is similar for this entire age range (Stein and Stein, 1992). The continental side is defined by a continental geotherm to generate the global average back-arc heat flow value of 80 mW/m^2 (Currie and Hyndman, 2006) in the absence of direct observations.

Parameter	Value	Reference
Incoming oceanic plate age (Myr)	85 (Midpoint of 70-100)	(Mountain and Prell, 1990; Hutchison et al., 1981)
Plate convergence rate (mm/yr)	40	(DeMets et al., 2010)
Incoming sediment thickness (km)	7 (5 accreted, 2 subducted)	(Smith et al., 2012)
Thermal conductivity of upper plate ($Wm^{-1}K^{-1}$)	1.2– 2.9 Continental crust 2.9 Oceanic Crust 3.1 Mantle	(Hutchison et al., 1981, Kaul et al., 2000, Wada and Wang, 2009)
Density (kg/m^3)	2750 – Continental Crust 3300 – Mantle and Oceanic Crust	(Wada and Wang, 2009)
Specific Heat ($J/kg\ K^{-1}$)	1250 (constant value)	(Wada and Wang, 2009)
Heat Production (μWm^{-3})	0.02 – Mantle and Oceanic Crust 0.4 – 0.7 – Continental Crust	(Wada and Wang, 2009)
Effective coefficient of friction (μ')	0.03	(Wada and Wang, 2009)

Table 3.1. Table of input parameters to the 2D numerical model.Further details of the reasoning behind the choice of values are discussed in the text.

The subducting plate geometry is constructed from combined 2D seismic reflection lines (Smith et al., 2012) (depth converted using interval velocities from Kopp et al. (2000)), intraslab seismicity (ISC/EHB Catalog: though seismicity is not extensive), and an assumed depth of 100 km for the slab beneath the volcanic arc based on the global average (Wada and Wang, 2009) (Figure *3.2*a). The estimated errors in the depth of the plate boundary range from ± 500 m in the outer prism, to ± 10 km at 100 km depth due to the low level of intraslab seismicity. This construction produces a shallowly-dipping plate geometry, similar to that predicted by previous studies (Byrne et al., 1992, Bijwaard et al., 1998). The forearc Moho is assumed to occur at 30-35 km depth in the absence of observational constraints. The main material parameters are described in Table 3.1. We use a thermal conductivity in the upper

plate increasing linearly from 1.2 $Wm^{-1}K^{-1}$ in the outer prism (Hutchison et al., 1981) to 2.5 $Wm^{-1}K^{-1}$ at 200 km along the profile. This is to account for the low thermal conductivity of the high-porosity outer prism sediments, relative to the more consolidated forearc rocks. Published values for local density, specific heat, or radiogenic heat production have not been identified so we have adopted typical values. Viscous mantle-wedge flow is modelled exactly as in Wada and Wang (2009) using the dislocation-creep rheology, however the wedge flow is unimportant for our study of the shallow thermal regime.

Frictional heating along the plate interface is calculated using the static friction law (Wada and Wang, 2009). The effective coefficient of friction (Table 3.1) includes the effect of pore fluid pressure. For example, if a true friction coefficient of 0.6 is assumed (similar to Byerlee's law), then the effective coefficient (μ') of 0.03 corresponds to a pore fluid pressure 95% of lithostatic. At greater depth, the frictional heating changes to viscous shear heating along the interface with rapidly diminishing intensity, assigned using the method of Wada and Wang (2009). For the continental crust-slab contact with very low effective friction and high strain rate, the transition occurs at temperatures much higher than 350°C. For the shallow part of the mantle wedge-slab contact, because of the presence of talc and other hydrous minerals, the interface becomes extremely weak (Peacock and Hyndman, 1999), and therefore we assume the frictional heating changes to shear heating at the depth of the slab-Moho intersect.

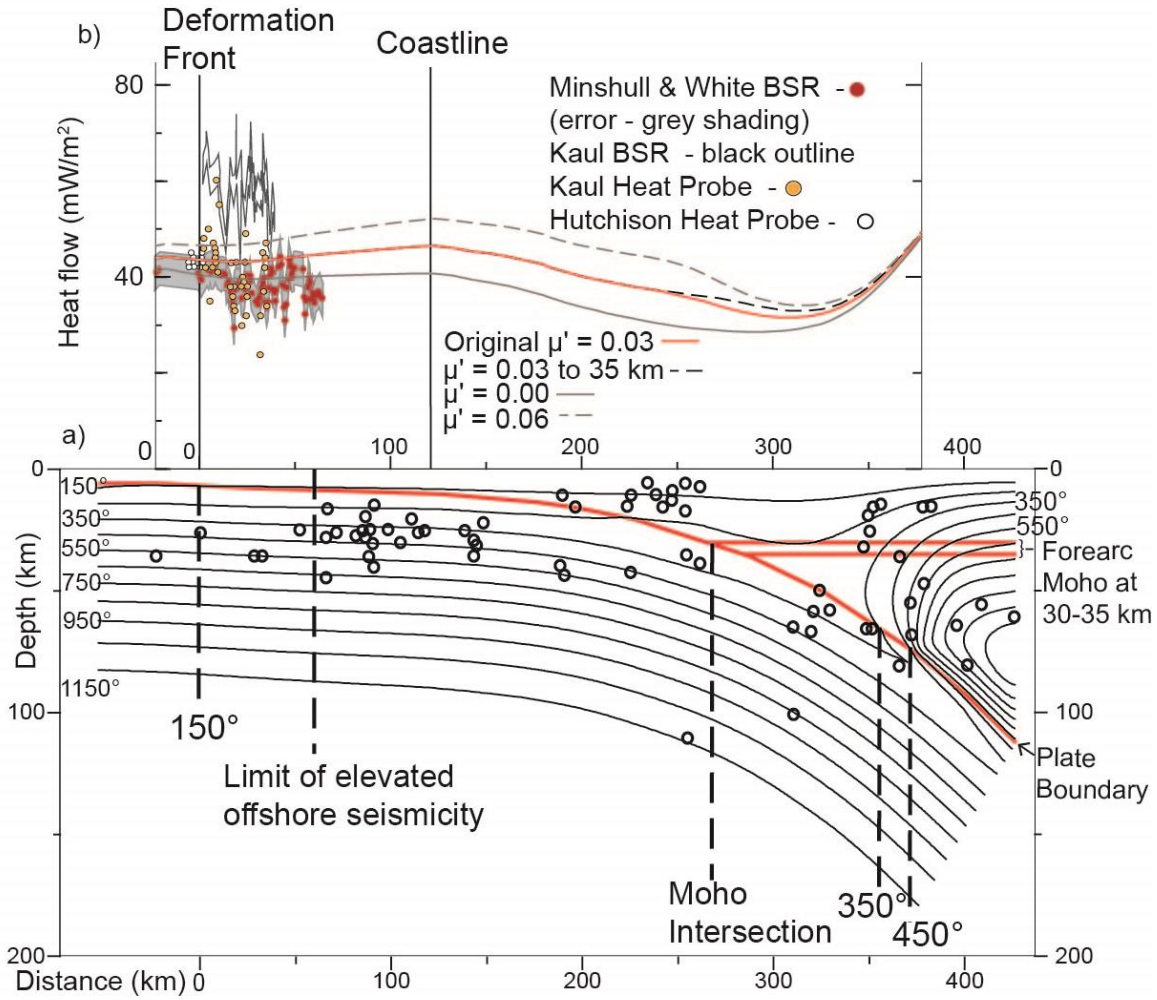

Figure 3.2. Results of thermal modelling and comparison with observed values.
a) Plate interface and forearc Moho indicated by red lines. For simplicity, the plate interface extends to the seaward model boundary to avoid dealing with complications of sediment deformation at the deformation front. Circles indicate seismicity as illustrated on Figure. 3.1. Depths of earthquakes prior to 1980 have very large errors which likely cause the disparity between seismicity and the plotted plate boundary in the seaward region. b) *Comparison of model-predicted heat flow with published data located within 50 km of the thermal profile.μ' – Effective Coefficient of Friction. Heat flow profiles generated from μ' values of 0.00 (no frictional heating), 0.03 (with the Moho at depths of 30 and 35 km), and μ'= 0.06 shown. Data from Hutchison et al. (1981) collected using a thermistor probe attached to a gravity corer. Data from Minshull & White (1989) calculated from BSR depth in reflection data. Heat probe data from Kaul et al. (2000) are fairly consistent with other datasets. Their BSR-derived values may vary from the Minshull and White (1989) results due to differing calculation methods.*

The model results are compared with observed heat flow values, both BSR-derived values and probe measurements (Figure *3.2*) (Hutchison et al., 1981, Minshull and White, 1989, Kaul et al., 2000). The differences between these datasets are likely due to differing data collection and processing methods. We favour the direct heat flow measurements of *Kaul et al*, (2000) and *Hutchison* (1981), and the BSR-derived values of *Minshull and White* (1989) to constrain our model as they show good mutual agreement. The scatter within individual datasets may be due to localized fluid flow within the upper sediments, and the effects of sedimentation/erosion in the prism. These values for comparison with our model are quite variable, but our model fits within the range of observed data. Sensitivity tests on heat production, thermal conductivity and sedimentation rate indicate that varying these values has little to no effect on the location of the updip limit (located at 150°), and causes a minimal variation (<5 km) in the placement of the downdip limit (located at the Moho intersection as a minimum or at 350°C as a maximum landward position). Varying these parameters affects the heat flow profile produced by the model by up to 10%.

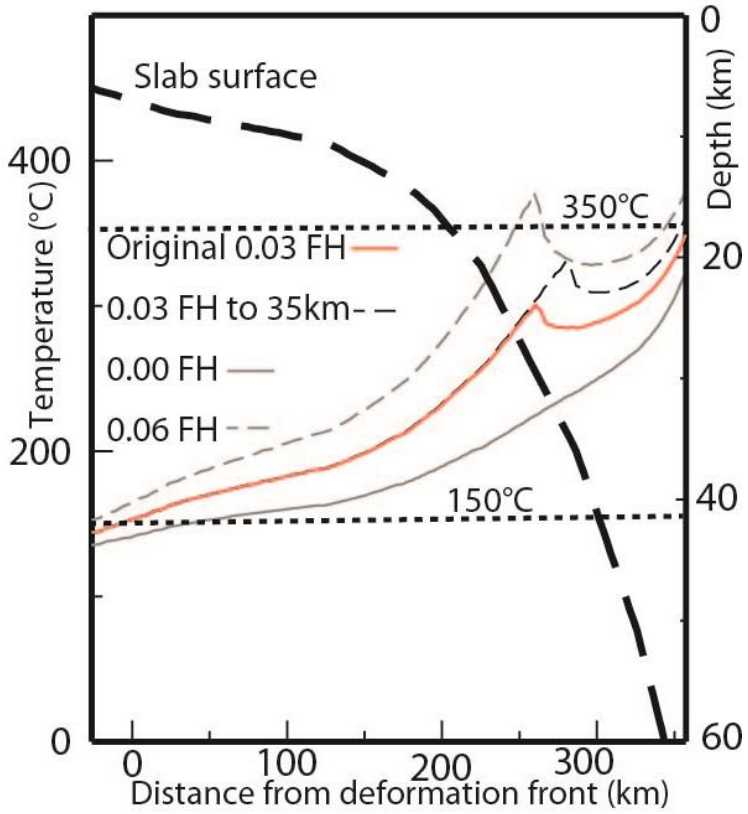

Figure 3.3. Plate boundary temperatures with distance and sensitivity test results.The peaks in the lines at ~ 300 km indicate where frictional heating changes to shear heating at the intersection with the Moho.

In thermal models of the shallow part of subduction zones, the greatest source of error is frictional heating along the interface. It overshadows errors in all the other parameters in Table 1. To illustrate model uncertainties, we show interface temperatures predicted with larger ($\mu' = 0.06$) or no ($\mu' = 0$) frictional heating (Figure 3.3). With large frictional heating, the interface may reach 350°C just shallower than the Moho intersect. With no frictional heating the interface stays cool until warmed by mantle wedge flow, though this is considered to be an unlikely scenario based on the results of previous studies (e.g. Wada and Wang, 2009). As explained in the preceding section, we assume frictional heat changes to shear heating at the Moho intersect. Having a deeper Moho thus makes the transition deeper; however, with our preferred $\mu' = 0.03$, the Moho intersect is still much cooler than 350°C (Figure 3.3). Additional heat flow measurements from the accretionary prism, particularly further landward, would help to constrain the appropriate level of frictional heating.

3.3 Results

The high plate boundary temperatures (~150°C) at the deformation front (Figure. 3.2a) due to the thick sediment section result in no thermally-predicted aseismic zone beneath the prism. However, the outermost 60 km of the accretionary prism appears to be devoid of significant observed seismicity (Figure 3.1), so we incorporate this as a possible aseismic zone when calculating minimum-width potential rupture scenarios (Table 3.2). We do not use the 1945 rupture when defining the seismogenic zone position because of its large location error, and instead we use the cluster of more recent and better located events slightly to the north. The shallow dip of the plate boundary, coupled with the shallow temperature contours, mean that a slight (±1-2 km) vertical shift in plate boundary position could lead to significant (± 10-20 km) lateral changes in the position of the 150°C contour intersection, however the thermal structure at the deformation front does suggest temperatures of 150°C at the plate boundary.

Scenario	Length (km)	Width (km)		Rupture area (m^2)		M_o (Seismic Moment) (N m)		M_w	
		Min	Max	Min	Max	Min	Max	Min	Max
Scenario 1: Full length of subduction zone	800	210	355	1.68E+11	2.84E+11	5.04E+22	8.52E+22	9.07	9.22
Scenario 2: Eastern half of Makran, east of Sistan Suture Zone	400	210	355	8.4E+10	1.42E+11	2.52E+22	4.26E+22	8.87	9.02
Scenario 3: Sistan Suture Zone to Little Murray Ridge	220	210	355	4.62E+10	7.81E+10	1.386E+22	2.343E+22	8.69	8.85

Table 3.2. Potential Magnitude Calculations. Estimated potential magnitudes generated by different rupture scenarios (does not account for partial/heterogeneous rupture). 10 m of coseismic slip is used. Maximum potential rupture width is taken from the deformation front to the 350°C contour. Minimum width is taken from the limit of significant offshore seismicity (~60 km landward of the deformation front) to the forearc Moho (30 km) – subducting plate intersection.

The plate boundary does not reach 350°C until 350 km landward (60 km depth) of the deformation front. The 450°C contour is reached at 370 km (75 km depth). The plate boundary reaches our assumed forearc mantle 90 km seaward of the 350°C contour (at 260 km), and so this may represent the downdip limit if hydrated mantle material is present. It should however be noted that there is currently no evidence to support or refute the presence of hydrated mantle in the Makran and the position of the forearc Moho is poorly constrained.

3.4 Implications for Earthquake and Tsunami Hazards

We combine the thermo-petrologically-predicted limits with three likely rupture length scenarios (Figure 3.1) to calculate the maximum likely earthquake magnitude using the equations of Hanks and Kanamori (1979) (Table 2).

$M_o = A\mathbf{G}D$

$M_w = 2/3 * \log(M_o) - 9.1$

A (Rupture Area), D (Slip), $\mathbf{G}$ (Shear modulus)

The shear modulus used was 30 GPa (Hanks and Kanamori, 1979). The slip used to calculate seismic moment (M_0) was 10 m. Reducing the slip to 7 m, as modelled by Byrne et al. (1992) for the 1945 event, results in a magnitude reduction of ~ M_w 0.1. The minimum rupture width (across strike) used was 210 km, measured from the limit of significant offshore seismicity (therefore incorporating a ~60 km updip aseismic zone) to the plate boundary intersection with the forearc Moho at 30 km depth (a more conservative value to account for uncertainty in Moho depth). The maximum potential rupture width of 355 km was measured from the deformation front to the 350°C contour. Using the 450°C contour intersection would increase the potential magnitudes by up to a further M_w 0.1. Using the youngest suggested oceanic plate age (~50Ma) moves the downdip limit seaward by ~50 km, with an associated < M_w 0.1 decrease in magnitude. The updip limit is unaffected. We used the plate boundary temperatures calculated for the $\mu' = 0.03$ case for these calculations. Using a higher or lower degree of frictional heating would shift the seismogenic zone seaward or landward respectively, with the most significant potential change being the introduction of a ~ 40 km updip aseismic zone in the $\mu' = 0$ case. However, this scenario is already encompassed by our minimum width scenario.

The longest calculated rupture would encompass the full length of the subduction zone (~800 km). There is no historical record of such a rupture occurring (although this record is not extensive or precise) and it is possible that the Makran predominantly ruptures in shorter segments. However evidence from other subduction zones indicates that megathrust earthquakes can rupture multiple

segments, therefore this scenario is included. The second scenario (400 km) encompasses the Pakistan section of the Makran, east of the Sistan Suture Zone. This half of the subduction zone has significantly higher background seismicity than the western half, and includes the 1945 rupture. The final scenario (220 km) accounts for the Little Murray Ridge (Figure 3.1) potentially impeding eastward propagation of a rupture. The different rupture scenarios produce earthquakes with a potential magnitude range of M_w 8.7 – 9.2 (Table 3.2). The uncertainties discussed above generate a cumulative ± 5 % estimated error in these magnitude values.

3.5 Discussion and Conclusions

The potential earthquake magnitudes of M_w 8.7 – 9.2 based on thermal modelling of the Makran are larger than any recorded historical event at this margin. However, palaeoseismological evidence from margins such as Cascadia (e.g. Jacoby et al., 1997) has shown that recurrence intervals can exceed a short historical record. Considering the Makran convergence rate (4 cm/yr), a recurrence interval of 250 years would be required to accumulate the 10 m slip used in this study.

The Makran displays a wide potential seismogenic zone most similar to that of the Alaskan margin (~250 km) where the subducting plate also dips at a shallow angle (Oleskevich et al., 1999, Gutscher and Peacock, 2003). However at the Alaskan margin the updip limit occurs 50 - 100 km landward of the trench because the thinner sediment cover (~3 km) results in a much cooler updip décollement (Gutscher and Peacock, 2003). The potential for shallow rupture due to the occurrence of thick sediments is similar to, but more extreme than, that predicted by thermal modelling of the N. Sumatra region of the 2004 earthquake (Klingelhoefer et al., 2010) where a shallow updip limit is also attributed to thick sediment cover (up to 4-5 km) on the 60Ma subducting plate, with resultant high temperature and strength basal prism sediments. Our rupture scenarios give the maximum potential rupture extent, but the plate boundary may rupture in a partial or heterogeneous manner in a given earthquake. We currently have no information regarding the degree of coupling between the plates.

Following the 1945 earthquake, tsunami run-ups of up to 15 m were reported at Pasni, 1.4 m at Karachi and 2 m at Mumbai (Heidarzadeh et al., 2008). Previous tsunami modelling of the near-field effects of a rupture east of the Sistan Suture Zone (Rupture Scenario 2, Table 3.2) produced wave heights of up to 9 m, and up to 15 m for a rupture of the entire subduction zone (Rupture Scenario 1, Table 3.2) (Heidarzadeh et al., 2009). These models used rupture widths of 100-150 km, and fault displacements of 13-25 m (therefore comparable M_o to our rupture scenarios). Far-field modelling of similar scenarios highlights the potential hazard to Western India, the Maldives and the Seychelles from a Makran megathrust event (Okal and Synolakis, 2008).

Assuming worst-case scenarios, our thermal modelling indicates that the Makran has a wide potential seismogenic zone, and may be capable of generating a very significant (>M_w 8.5) tsunamigenic earthquake. The thick sediment cover (up to 7 km) on the incoming plate leads to high (~150°) plate boundary temperatures at the deformation front making the megathrust potentially seismogenic to shallow depths. The shallow dip of the subducting plate and the lack of significant along-strike rupture barriers lead to a potential seismogenic zone of up to ~350 km in width and 800 km in length, generating large potential earthquake magnitudes. These results illustrate the need for careful analysis of the risks posed by the Makran subduction zone to the neighbouring coastlines of Pakistan, Iran, Oman and India and the need for further palaeoseismological investigations. This study may have important global implications for the hazard potential associated with other high sediment input subduction zones with significant accretionary prisms.

Acknowledgements. The authors would like to thank Ikuko Wada for her assistance in developing the numerical model. We thank the Natural Environment Research Council-NERC (Grant No. NE/H524922/1) for studentship support. We thank Harold Tobin and an anonymous reviewer for their helpful comments. This is also Geological Survey of Canada contribution 20120387

4 Chapter 4. Fluid generation and distribution in the highest sediment input accretionary margin, the Makran

This chapter forms the basis of a manuscript in preparation to be submitted to Earth and Planetary Science Letters in 2013.

Initial interpretation of the Meteor seismic dataset and small area of the WesternGeco seismic dataset undertaken by Daniel Arráiz. This formed part of a Masters project at the University of Bremen, supervised by Volkhard Spiess with co-supervision by G. Smith. Full interpretation of the WesternGeco® dataset, and integration with Meteor dataset undertaken by Gemma Smith. Analysis and write-up completed by Gemma Smith. Lisa McNeill and Tim Henstock provided helpful feedback and discussion.

Fluid generation and distribution in the highest sediment input accretionary margin, the Makran

Abstract

The occurrence of fluids in subduction zones can influence seismogenic behaviour and prism morphology. The E. Makran subduction zone (offshore Pakistan), has a very thick incoming sediment section of up to 7.5 km, providing a large potential fluid source to the accretionary prism. A hydrate bottom simulating reflector (BSR), zones of high amplitude reflectivity, seafloor seep sites and reflective thrust faults are all visible to varying spatial extents across the accretionary prism, indicating fluid and suggesting active fluid migration. High amplitude free gas zones and seep sites are associated with anticlinal hinge traps, and fluids appear to be sourced from the shallow sediment section (previous geochemical analyses of seep gases found a biogenic methane dominated system) with fluid migration to the seafloor facilitated by minor normal faults. There are no observed seep sites associated with the surface expression of the wedge thrust faults. Thrust fault reflectivity is restricted to the upper 3 km of sediment, and the deeper décollement is non-reflective, indicating a lack of deep fluid migration. Thermal modelling of sediments at the deformation front indicates temperatures of over 100°C in the basal sediment section. These results suggest that the deeper sediment section may be relatively dehydrated and that this part of the sediment section is not currently contributing to fluid expulsion in the Makran accretionary prism, with implications for seismogenic potential.

4.1 Introduction

Subduction zones, particularly those with significant accretionary prisms, have long been recognised as potential fluid-rich systems (e.g. Moore et al., 1990b, Chamot-Rooke et al., 1992, Moore et al., 1995, Bangs et al., 1999, Henry et al., 2002, Morley, 2007, Barnes et al., 2010, Crutchley et al., 2013). Fluids can influence accretionary prism morphology and the seismogenic behaviour of the plate boundary and crustal

faults (e.g. Hyndman et al., 1997, Carson and Screaton, 1998, Tobin and Saffer, 2009). Fluids can be sourced both from the subducting oceanic crust (Peacock, 1990), and the sediment overlying it (Moore and Vrolijk, 1992). At subduction zones such as the Makran with a thick sediment section, the sediment section is likely to be the dominant fluid source. Pore waters released through the compaction of both accreted and underthrust sediment will provide a large flux of fluid, particularly in the initial stages of deformation and diagenesis (Moore and Vrolijk, 1992, Saffer and Screaton, 2003). At greater burial depths and temperatures, diagenetic processes dominate: clay minerals and silica within the sediment dehydrate to contribute additional fluid, and hydrocarbons may be generated (e.g. Moore and Saffer, 2001, Saffer et al., 2008, Saffer and Tobin, 2011). These processes and their approximate temperature windows are summarised in Table 4.1.

Process	Temperature Range (°C)	Diagenetic product	Reference
Opal to Quartz	~60-100	Water	(Moore and Vrolijk, 1992)
Smectite to Illite	~100-150	Water	(Saffer et al., 2012)
Biogenic Hydrocarbon Production	< ~50	Methane	(Saffer et al., 2012)
Thermogenic Hydrocarbon Production	~60-150	Methane and higher hydrocarbons	(Peacock, 1990)

Table 4.1. Table of sedimentary digenetic processes, the temperatures at which they occur, and their products.

Prior to subduction or accretion, the sediments in the incoming section will experience vertical compaction, porosity reduction and associated dewatering. The extent to which these processes occur depends primarily on sediment burial depth, lithology and permeability (Saffer and Tobin, 2011). Once the incoming sediment section begins to experience subduction-related deformation and horizontal compression, fluids may be released either as diffuse flow during compaction, or as focused flow along faults, fractures and veins (Moore and Vrolijk, 1992, Carson and Screaton, 1998). Which of these processes dominates the extent of fluid expulsion is controlled by the relative and absolute permeabilities of the sediment and faults. The

presence of vertical impermeability due to sub-horizontal sedimentary layering may favour focused flow along faults, especially considering the fracture networks present in accretionary prisms and the oceanic plate (basement and sediments). Fluid flow may be episodic, potentially related to temporal changes in the stress field and linked to seismicity, and may evolve between diffuse and focused through time (Saffer and Screaton, 2003). Fluid release due to initial compaction and consolidation is likely to dominate in the initial stages of deformation, with dehydration reactions occurring at a later stage (Saffer and Tobin, 2011).

Biogenically generated hydrocarbons (microbial degradation of organic matter) in the accreted sediment can also be trapped within the accretionary prism. Methane may migrate buoyantly through the sediment section as free gas, or dissolved in pore fluid generated by compaction and tectonic compression of the sediment (Gorman et al., 2002). At certain temperatures and pressures, free gas may combine with pore waters to form gas hydrate in the upper sediments, commonly indicated by the presence of a Bottom Simulating Reflector (BSR) (Buffett, 2000).

Evidence for fluid occurrence and migration has been described at many accretionary prisms worldwide including Nankai (Japan), Hikurangi (New Zealand), Barbados and Cascadia (e.g. Olu et al., 1996, Moore et al., 2001, Henry et al., 2002, Barnes et al., 2010). In the Tokai region of the Nankai margin, seep sites have been identified both at the surface of prism thrust fault hanging walls, and at the outcrops of the thrusts themselves, with some seeps linked to high fault reflectivity (Henry et al., 2002). A BSR is observed in the Muroto prism, intermittently in the Kumano prism (Hamamoto et al., 2011, Kinoshita et al., 2011), and in the forearc basin of the Tokai region further to the northeast (Ashi et al., 2002). The Hikurangi margin has extensive evidence for fluid occurrence including a BSR and high seismic amplitude zones (indicating free gas) (Pecher et al., 2010) and seep sites located on prism anticlinal ridges (Barnes et al., 2010, Netzeband et al., 2010). The Barbados accretionary prism has widespread seep sites and mud volcanoes, predominantly located on ridges (Olu et al., 1996). At Cascadia a strong BSR and methane seafloor seepage has been observed, particularly at Hydrate Ridge offshore Oregon (Crutchley et al., 2013) and at sites offshore Vancouver Island (Zühlsdorff et al., 2000, Riedel et al., 2006). Negative polarity fault

reflectors have also been observed offshore Oregon, attributed to high pore fluid pressure and in some cases linked to seabed seeps (Moore et al., 1995). The Makran will be compared with some of these examples in order to further understand the context of fluid occurrence.

4.1.1 Geological setting and previous investigations of fluid occurrence in the Makran

The Makran Subduction Zone is formed where the Arabian Plate subducts beneath the Eurasian plate at ~ 4 cm/yr (DeMets et al., 2010). The thick (up to 7.5 km) incoming sediment section has led to the formation of the world's largest accretionary prism, the offshore section of which is dominated by a structurally relatively simple imbricate thrust belt (Smith et al., 2012). Previous studies have investigated the distribution of fluid-related features in parts of the Makran, both on the seabed and in the shallow sediments (von Rad et al., 2000, Wiedicke et al., 2001). The occurrence of a widespread BSR indicating gas hydrate has been noted in more localised 2D seismic studies (e.g. Minshull and White, 1989, Grevemeyer et al., 2000, Kopp et al., 2000, von Rad et al., 2000) followed by confirmation of its widespread occurrence on the Pakistan margin (Smith et al., 2012). The application of a full waveform inversion to the BSR suggests that hydrate concentrations above the BSR may be as low as 10%, and that the majority of the methane exists in free-gas form (Sain et al., 2000). The free gas zone beneath the BSR is believed to have formed due to a combination of rapid hydrate recycling due to uplift in the wedge, and the stabilisation of gas due to the solubility-curvature mechanism promoted by slow upward fluid flow (Haacke et al., 2007). Active fluid escape has been detected through methane-rich plumes identified in the water column from CTD measurements, and from observed seafloor seeps and associated vent fauna across the accretionary prism (von Rad et al., 1996, von Rad et al., 2000). Most recently R/V Meteor Cruise 74, Legs 2 & 3 in 2007 collected a range of geophysical and geochemical data including multibeam bathymetry, ROV video footage, TOBI 30 kHz sidescan sonar and multichannel seismic data in order to investigate prism structure and fluid occurrence between ~62.4° -63.1°E (e.g. Spiess, 2007, Bohrmann, 2008,

Ding et al., 2010, Römer et al., 2012). High frequency seismic reflection data (from the Meteor cruise) indicate the presence of high amplitude zones beneath the Sixth Ridge anticline (40 km north of the deformation front, (Figure 4.1) and Ding et al. (2010) discussed how these may indicate free gas with links to seafloor seeps (Ding et al., 2010). Part of the Meteor dataset is utilised in this study in conjunction with a more extensive, lower frequency reflection seismic dataset (collected by WesternGeco®) in order to establish if the pattern observed by Ding et al (2010) is consistent along strike. The WesternGeco dataset used in this study (Figure 4.1) was previously used for a structural analysis of the accretionary prism (Smith et al., 2012).

4.2 Data

This study is based on a combination of two 2D seismic reflection datasets of different frequency and resolution, multibeam bathymetry, sidescan sonar and previously identified seeps from ROV/TV sled footage (Bohrmann, 2008). We have incorporated both high frequency and low frequency seismic reflection datasets in order to compare and improve the imaging of fluid-related structures. These two datasets overlap as shown in Figure 4.1. The lower frequency dataset consists of over 6000 km of seismic reflection data collected by WesternGeco® in 1998-1999 with a dominant frequency range of 4 – 60 Hz. This dataset contains 19 strike lines and 34 dip lines with a line spacing of 12 km and a shot spacing of 12.5 m (Smith et al., 2012). The high frequency dataset was collected during R/V Meteor Cruise M74/2 in 2007 with a frequency range of 50-200 Hz (Spiess, 2007, Ding et al., 2010). An initial investigation of high amplitude zones and BSR distribution of the high frequency dataset and the overlapping region of the low frequency dataset was undertaken by Arráiz and Spiess (2012).

For the purposes of this study we have divided the margin into three sections; western (W), eastern (E) and central (C), based on common properties of the incoming section (Figure 4.1). The western section has the thickest incoming sediments of 6.5 - 7.5 km and the central section is located where the Little Murray Ridge (White, 1983) intersects the deformation front, locally reducing sediment

thickness. The eastern section is located where the effects of the impinging Murray Ridge and the Pakistan coastline combine to influence sediment input and prism structure (Smith et al., 2012).

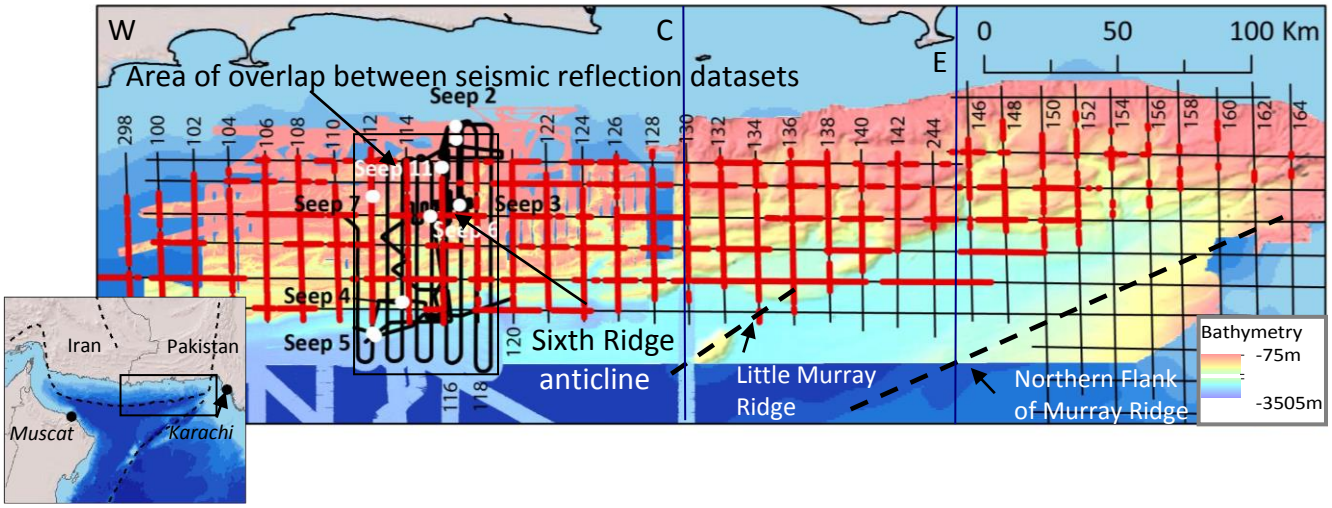

Figure 4.1. Map of data used and BSR and seep distribution. Inset map shows location of data. High frequency dataset in thick black lines, low frequency dataset in thin, black numbered lines. Regions where the BSR is visible on low frequency data indicated in thick red lines. White dots indicate seep sites. Western (W), Central (C) and Eastern (E) sections are defined. Little Murray Ridge and Murray Ridge indicated by black dashed lines. Low frequency seismic lines used in this study are numbered.

4.3 Results

4.3.1 High amplitude zones and seabed seeps across the accretionary prism

In the shallow section between the BSR and the seabed (the uppermost 500 m of sediment), zones of increased seismic amplitude associated with stratigraphic layers are visible, indicating the potential presence of free gas within the hydrate stability zone (Figure 4.2). For the purposes of consistency, we have only picked those zones which have a lateral extent of >500 m. The high amplitude zones consist of multiple short high amplitude segments, individual high amplitude horizons, and diffuse patches of high amplitude reflectors. The discontinuous nature of many of the high amplitude zones can make their polarity difficult to ascertain, and both positive and negative polarity regions can be identified. These zones predominantly occur in the

hinge zones of anticlinal ridges (hanging wall of the prism thrusts). The high amplitude zones indicate that gas is being sealed/trapped in the shallow sediments by stratigraphic horizons with reduced vertical permeability.

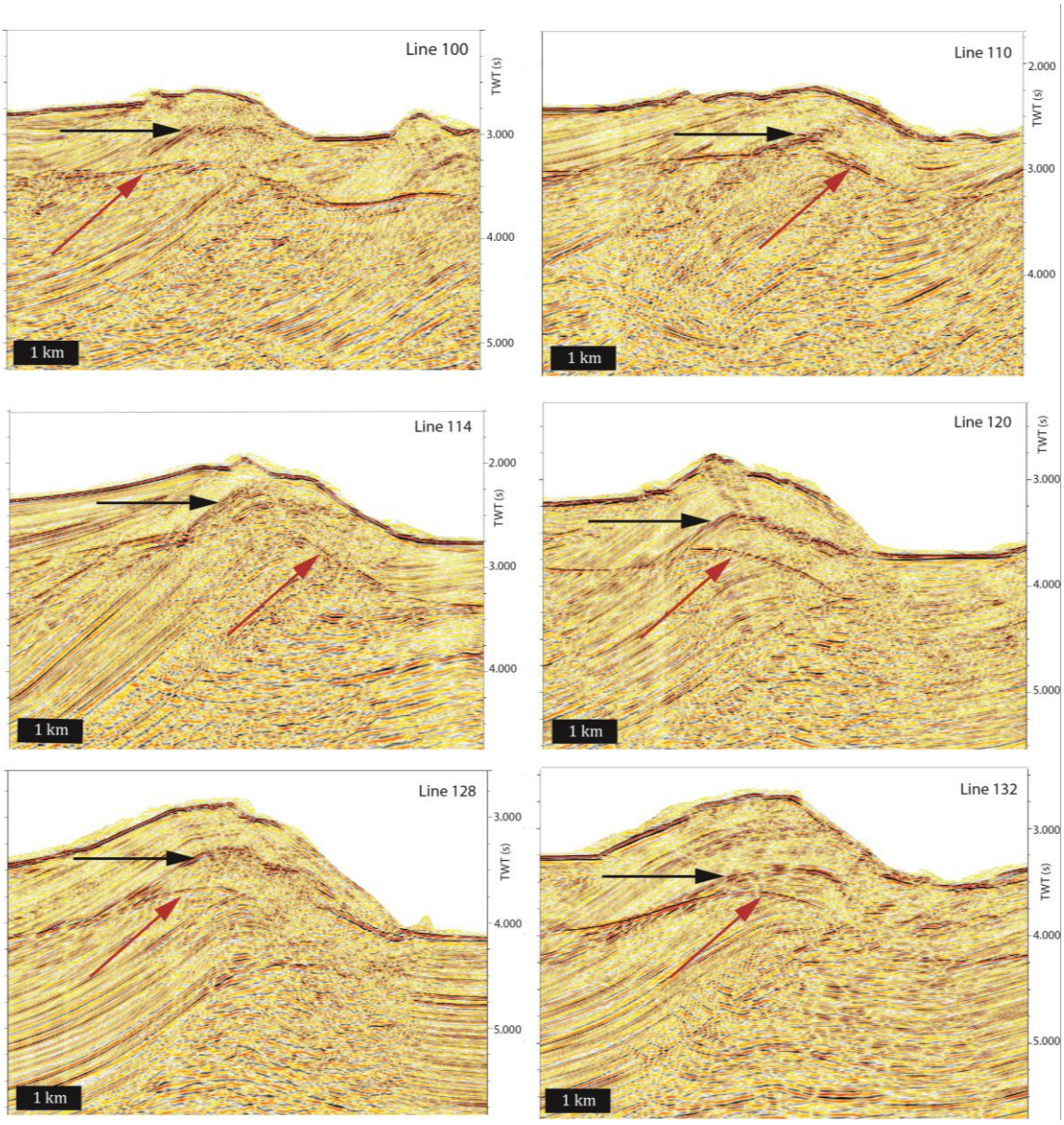

Figure 4.2. Examples of the interaction between BSR and high amplitude zones. Width of view ~7 km. Black arrows point to zones of high amplitude reflections, red arrows to the BSR. All images are North to the left and South to the right.

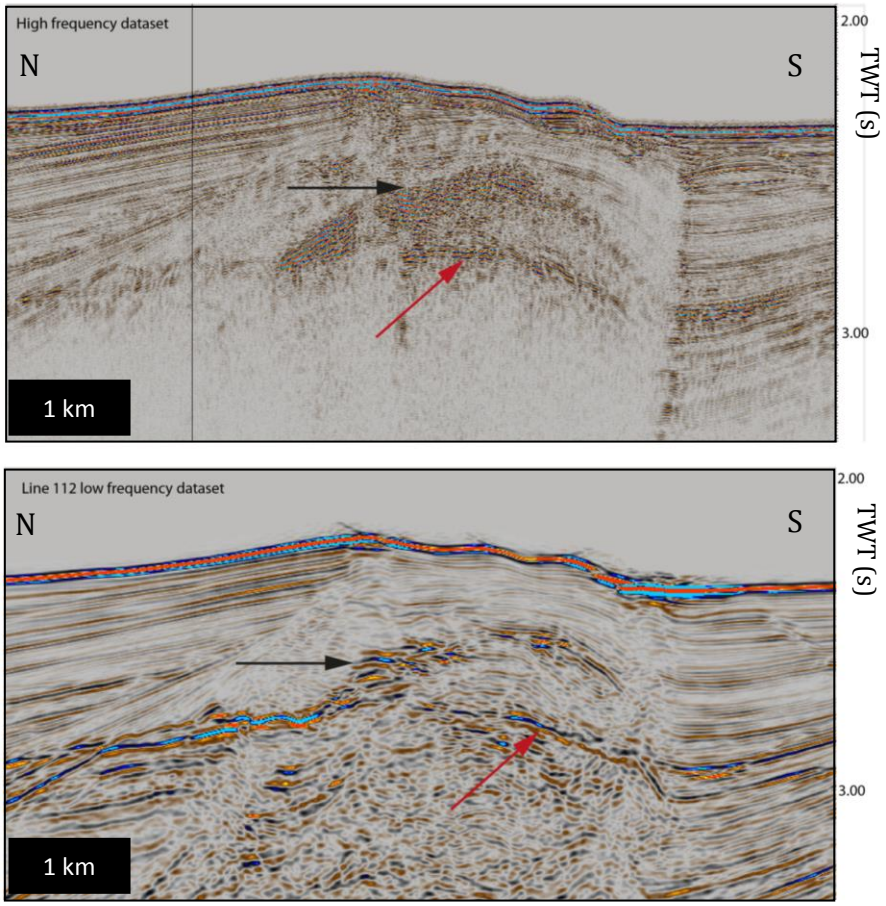

Figure 4.3. An example of the same high amplitude zone viewed in both datasets. The high amplitude zone (black arrow) is larger in the high frequency dataset (Arráiz and Spiess, 2012), but is clearly visible in both. A BSR is also visible in both datasets, indicated by a red arrow.

The high amplitude zones tend to be more pronounced in the high resolution/frequency dataset (Figure 4.3) (Arráiz and Spiess, 2012) but there is generally good agreement between the two datasets. In the west, high amplitude zones are distributed across both the landward and seaward regions of the studied prism (outer ~75 km), but progressing eastwards they become less frequent and more concentrated in the frontal prism (Figure 4.4). Where the datasets overlap, they both show that high amplitude zones are clustered around the frontal and sixth ridges (Ding et al., 2010). However this pattern does not continue along the remainder of the margin (Figure 4.4).

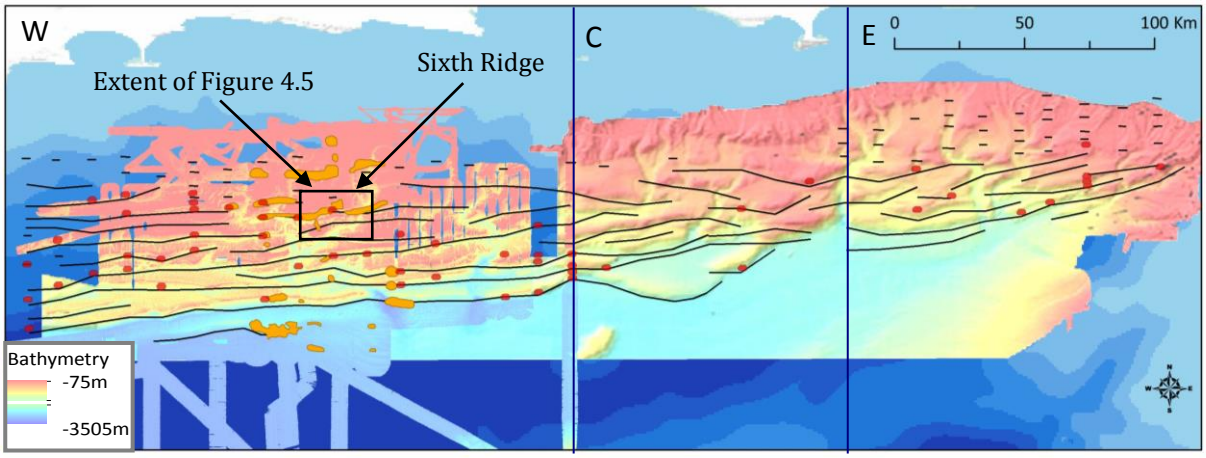

Figure 4.4. Map of high amplitude (free gas) zones. Red zones identified in low frequency dataset, orange in high frequency dataset. In the region where the two datasets overlap, there is good agreement in the zones identified, but with more high amplitude zones easily identified in the high frequency dataset. Black lines are prism thrust faults identified in Smith et al. (2012). Thrust faults are picked to their visible fault tip, which is often not at the seabed; therefore some fault traces appear slightly landward of their associated ridges.

The concentration of high amplitude zones around the sixth ridge is unlikely to be related to variations in the deeper fault structure, as there is no visible linkage between the underlying thrust fault and the high amplitude patches, and there is no evidence from the low frequency data that the thrust fault underlying the sixth ridge is structurally distinct from faults further seaward in terms of displacement or timing of activity. At this location the sixth ridge forms the seaward edge of a mid-slope plateau with reduced bathymetric expression of the underlying thrust faults (Figure 4.4). It does not appear to be an out-of-sequence thrust, as have been observed at other margins influencing fluid transport (e.g. Park et al., 2002a), rather a simple in-sequence imbricate thrust. This concentration around the sixth ridge may instead reflect a local change in prism morphology. The sixth ridge is eroded by canyon systems and general slope failure (Figure 4.5), particularly of the ridge flank, to a greater degree than other locations along the margin, and this enhanced erosion may lead to increased gas migration and release.

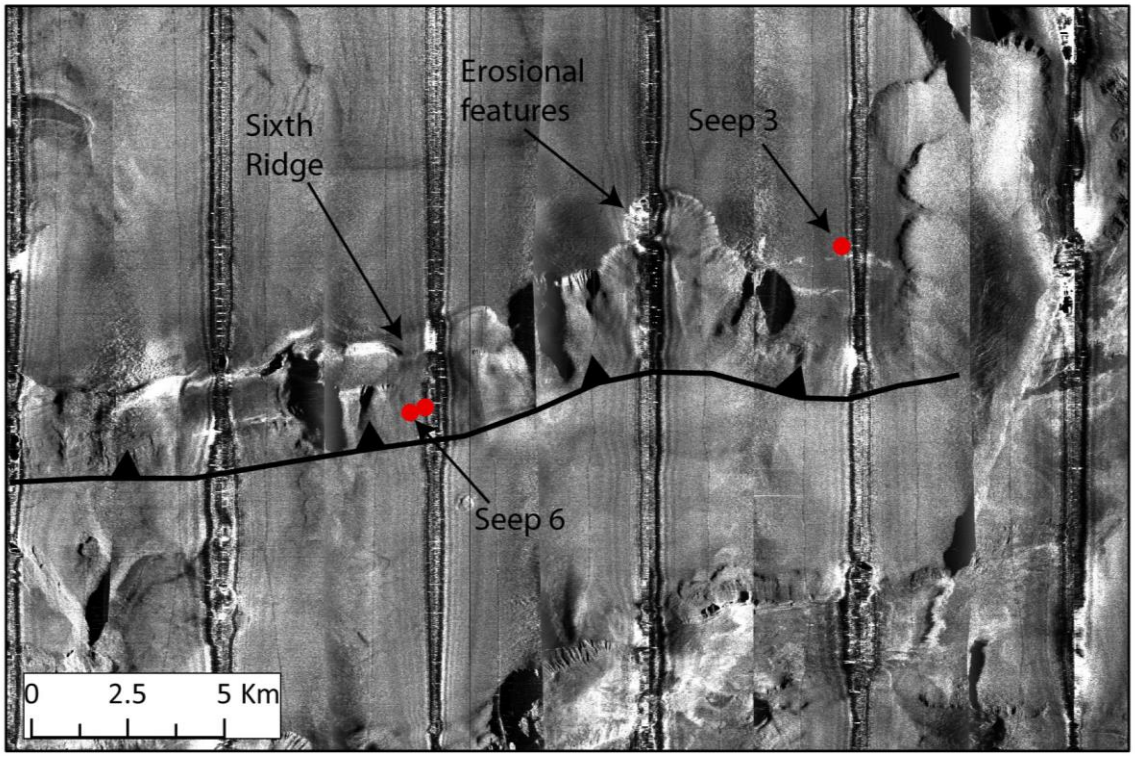

Figure 4.5. Close-up of the sixth ridge and thrust showing seep locations on TOBI sidescan data. Horseshoe shaped erosional features are visible on the ridge. Seeps indicated by red dots.

In the region covered by the high frequency dataset we also have cold seep and flare locations observed on sidescan sonar data (used to identify seep-related carbonates), and deep camera tow/ROV video (Bohrmann, 2008). As can be seen from Figure 4.6, the observed seeps are also clustered around the first and sixth ridges (mapped locations shown in Figure 4.1) coinciding with the high amplitude zones. Seeps 7 and 11 occur within this plateau, Seeps 3 and 6 occur on the sixth ridge itself, and Seep 4 occurs on the first ridge (Figure 4.6).

As with the high amplitude zones, the observed seep sites are located on ridge crests, rather than along thrust fault traces, suggesting little direct linkage to the prism thrusts. As discussed above, the low frequency data suggest that the clustering of high amplitude zones on the sixth ridge in the west is the exception rather than the rule along strike, with more dispersed locations in the central and eastern sections, and

we infer that this may also be the case for seep locations (no observations further east).

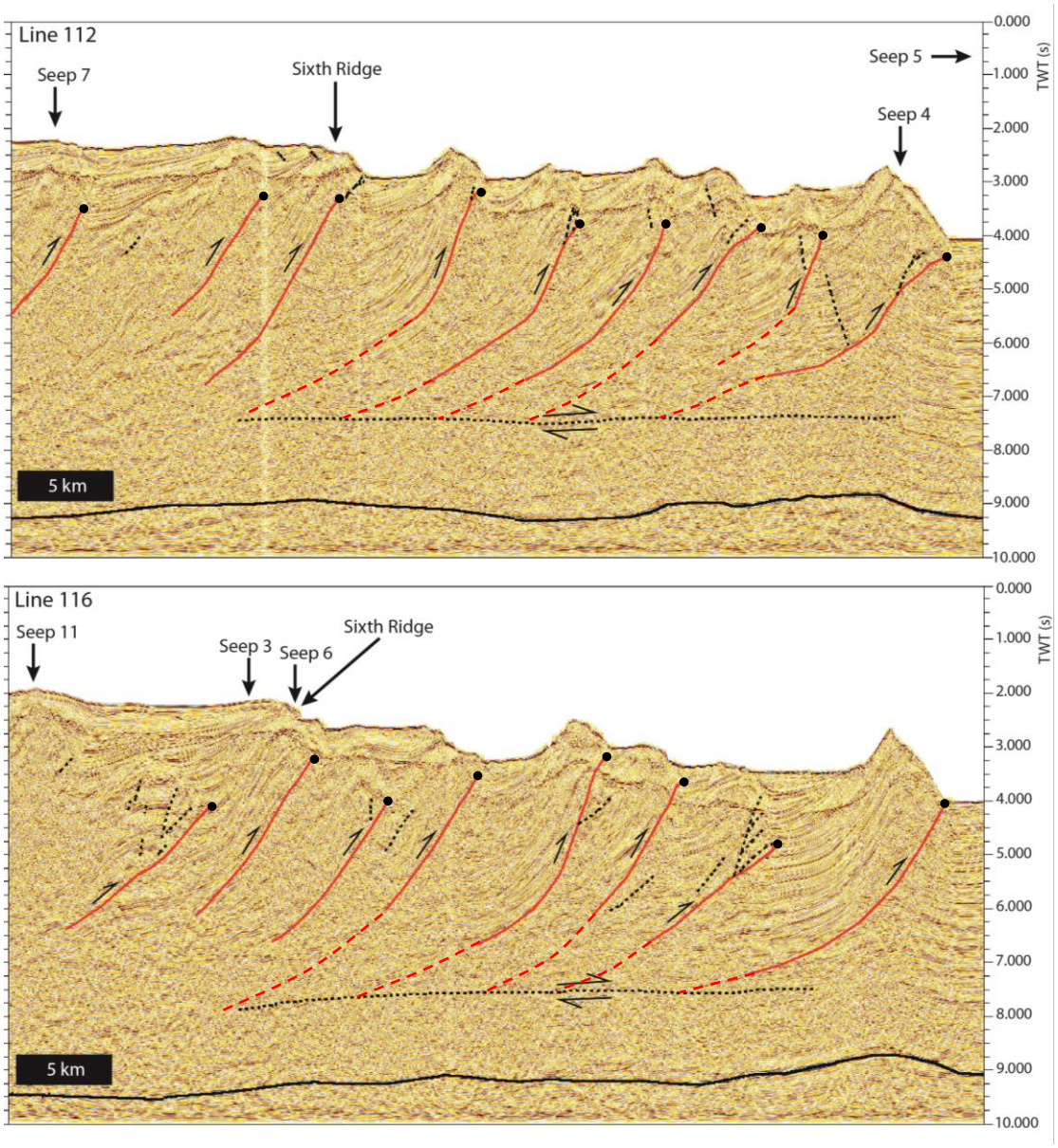

Figure 4.6. Seep sites from Bohrmann et al. (2008) projected onto the closest (<6 km) adjacent low frequency seismic lines. Width of view ~ 55 km. Seep 5 is located ~5 km south of the seaward end of Line 112, at the frontal ridge. Doted line is décollement surface, solid black line is top of oceanic basement.

Geochemical analyses were undertaken on seep gases during Meteor Cruise 74 Leg 3 (Bohrmann, 2008). These results indicate that seep sites at the deformation front (Seep 5) and on the continental shelf (Seeps 1 and 2) were strongly dominated by methane (~99.95%) with smaller quantities of ethane and propane suggesting a

dominantly biogenic source. This is similar to observations at other margins such as Chile and Cascadia (Riedel et al., 2006, Klaucke et al., 2012). Seep site 7, located on the 6th Ridge, had marginally lower quantities of methane (99.80%) and correspondingly higher amounts of ethane, propane and butane and so may have a minor thermogenic component, however it still presents a predominantly biogenic signature (Bohrmann, 2008). Further support for a biogenic/microbial origin is provided by carbon isotopic $\delta^{13}C$ values of CH_4 <–65.2 ‰ (Römer et al., 2012).

4.3.2 BSR distribution

A hydrate BSR occurs across the majority of the accretionary prism and in discrete zones in the incoming section, although it is difficult to identify in sub-horizontal beds, at a depth of ~500 m (most clearly imaged in the lower frequency dataset) (Smith et al., 2012). The BSR is also observed in the high frequency dataset as a less continuous reflector. Its continuity and amplitude decrease towards the eastern section, and the BSR is largely absent in the easternmost lines.

As BSR depth is controlled by the temperature and pressure gradient (in addition to the mix of hydrocarbon phases), upward fluid flow, e.g. along fault planes, may perturb the temperature gradient and locally displace the BSR (Riedel et al., 2006). However, there is no evidence from our low frequency dataset for displacement of the BSR when crossing prism thrusts, though in some cases BSR amplitude is reduced either at the fault or in the hanging wall (Figure 4.7). Previous analysis of the high frequency dataset (Ding et al., 2010) concluded that, though some shoaling of the BSR across faults was visible, this was of too small a change to be indicative of a significant perturbation in local heat and fluid flow. These results suggest the occurrence of widespread free gas and hydrate across the accretionary prism. They also indicate that any fluid flow along the prism thrust faults (as potentially suggested by reflective fault sections – see below) is not causing a major disturbance in the shallow sediment thermal gradient.

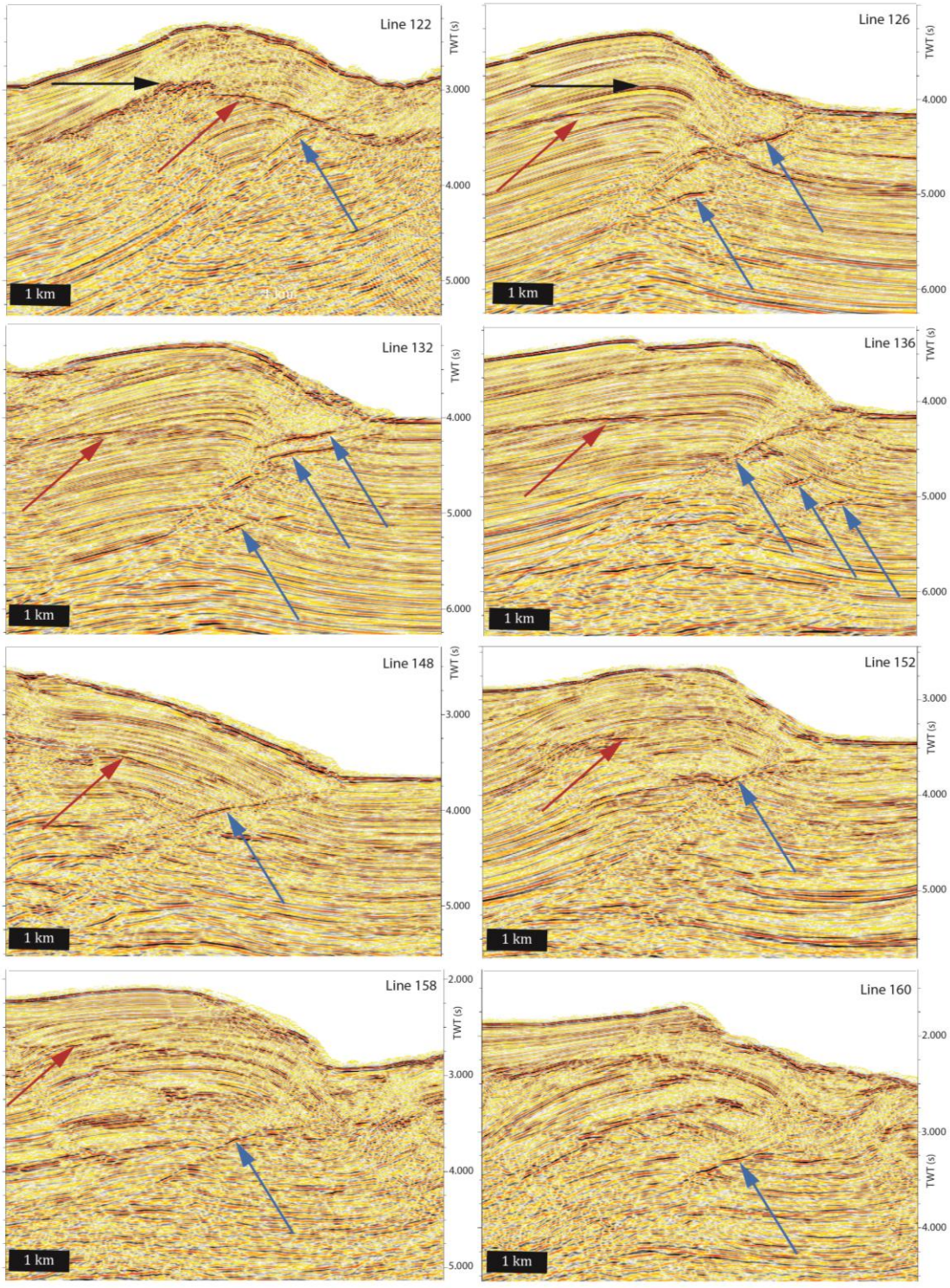

Figure 4.7. Examples of reflective faults. Width of view ~7 km. Black arrows point to high amplitude zones, red arrows point to the BSR, blue arrows to reflective faults. All images are north to the left and south to the right.

The relationship between the BSR and overlying high amplitude zones is variable. In some localities gaps are visible in the BSR beneath a high amplitude patch (e.g. Line

114 Figure 4.2), but in many other instances the BSR appears to be continuous beneath the high amplitude zones (e.g. 120/132 Figure 4.2). This is significant as for free gas to occur above the BSR it must either be being generated in situ, or (if it migrates from below the BSR) must have migrated through and become trapped within the gas hydrate zone without also being converted into hydrate.

4.3.3 Distribution of Reflective Thrust Faults

An important feature particularly observable in the low frequency dataset is the occurrence of reflective sections of thrust faults (Figures 4.7 & 4.8). Reflective faults, specifically those of negative polarity as seen in the Makran (Figure 4.8), may represent regions of high pore fluid pressure and possible fluid migration due to a local reduction in acoustic impedance in the fault itself caused by increased porosity (Moore and Vrolijk, 1992). This has been supported by the spatial correlation of reflective subsurface faults with surface fluid seeps at other margins e.g. Cascadia (Moore et al., 1991).

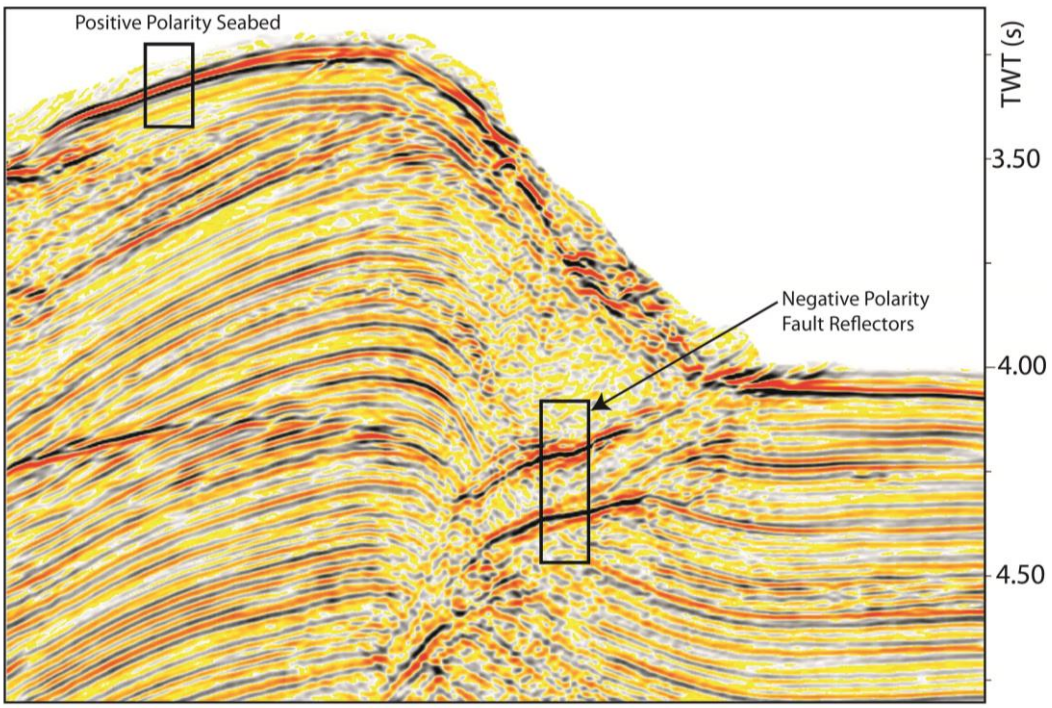

Figure 4.8. An example of negative polarity thrust fault reflectors from Line 132. The positive seabed reflector is highlighted for comparison. Width of view 5 km.

Negative polarity fault reflectors can also be caused by a velocity inversion between the relatively compacted upthrust hanging wall and the underlying, relatively uncompacted footwall sediments. However, the majority of faults in the Makran accretionary prism which demonstrate reflectivity have small (<300 m) displacements (Figure 4.9), therefore unlikely to generate the velocity contrast required.

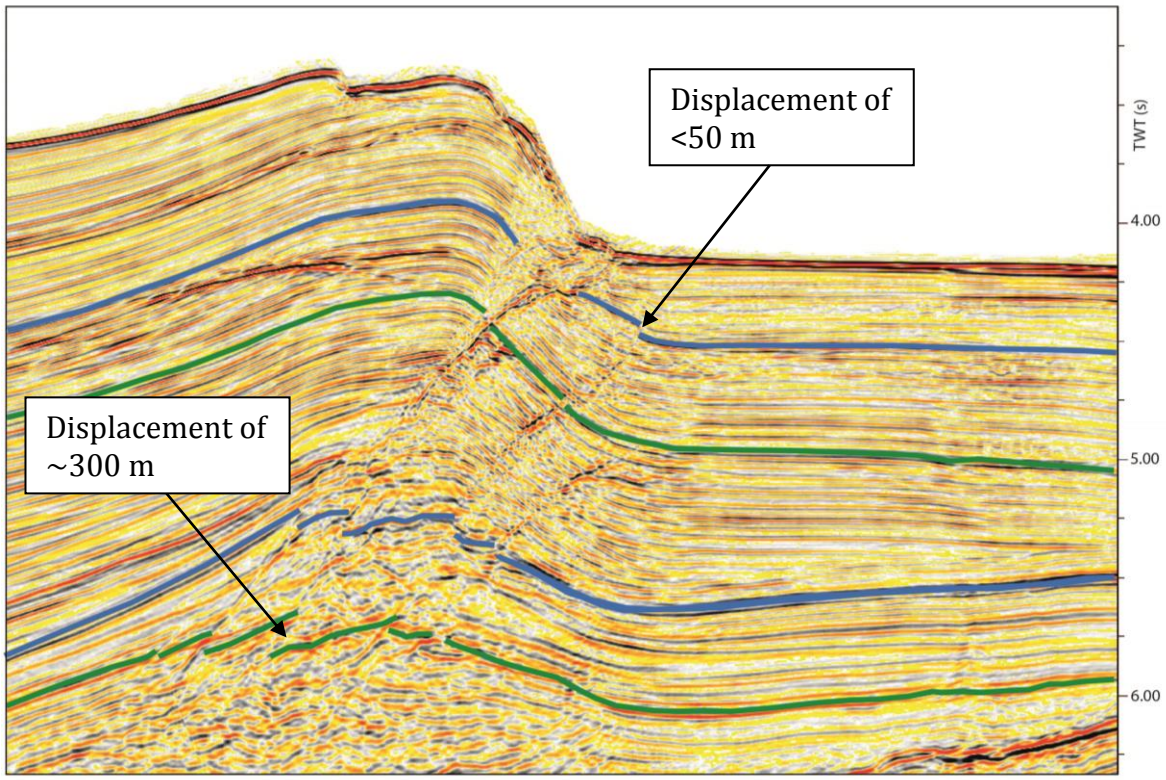

Figure 4.9. Example stratigraphic interpretation of the frontal thrust (Line 136). Width of view ~10 km. Displacements shown are <0.25 s TWT in the lower sections of the fault, which assuming a velocity of 2.5 km/s equates to a displacement of ~300 m. In the upper, reflective sections of the fault displacements are lower (50-100 m).

Low angle thrusts are more likely to show a coherent fault reflector due to their more favourable geometry for imaging. While this may accentuate the reflectivity of some of our examples (e.g. Lines 126 & 132 in Figure 4.7), the majority of the visible reflective faults are not dipping at a discernibly shallower angle than non-reflective examples.

The spatial distribution of fault reflectivity is shown in Figure 4.10 (see Figure 4.13 for the vertical distribution of reflectivity). Reflective faults are generally concentrated within the frontal prism (3-4 thrusts) though there is some occurrence landward, particularly in the west. This seaward concentration can be explained by the fact that the highest rate of fluid expulsion is likely to occur in the frontal prism where the incoming section starts to experience horizontal compression. There is an increased concentration of reflectivity adjacent to the incoming Little Murray Ridge, and in the eastern section in the vicinity of the main Murray Ridge. This pattern correlates with the increased basement topography and changes in the incoming section in these regions, and may be related to associated differences in stress state, deformation and related fluid flow and/or basement sourced fluids.

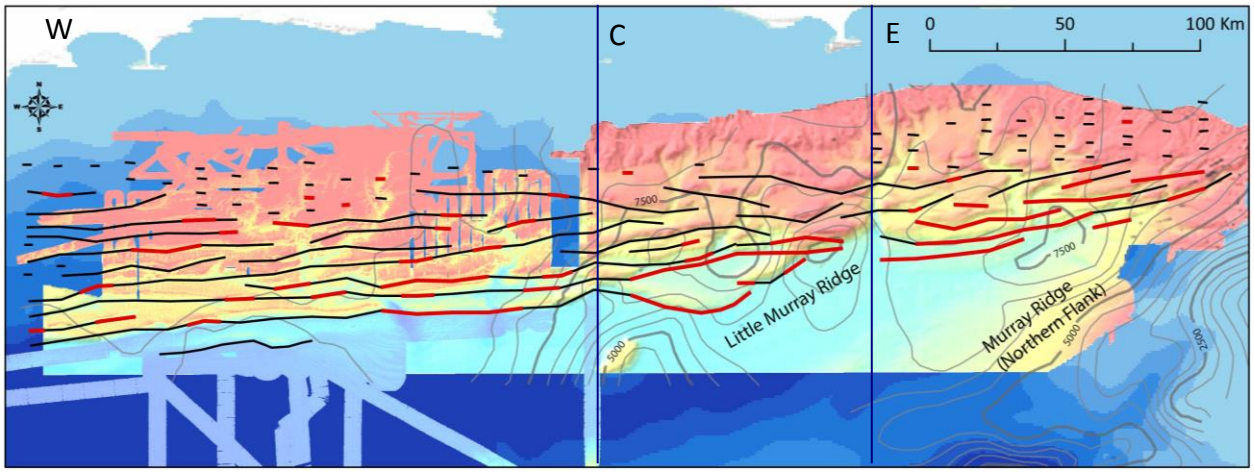

Figure 4.10. Map of reflective faults. Reflective faults indicated by thick red lines, non reflective faults by thin black lines. Grey contours indicate TWT to the top-basement surface, highlighting the Murray Ridge and Little Murray Ridge.

Vertically, the majority of thrust faults which show reflectivity are only reflective in the shallow portion of the thrusts (i.e. ≤4 km below the seafloor), though the reflective section does not often extend all the way to the seabed (Figure 4.7). The faults are not reflective down to the décollement (Figure 4.12), and the décollement itself is non-reflective (Smith et al., 2012), suggesting minimal fluid generation and migration at depth and no significant fluid flow pathways between the décollement and imbricate thrusts.

4.3.4 Relationship to predicted thermal structure

From the thermal structure of the Makran proposed by Smith et al. (2013), a thermal profile (at along strike position 62.9°E) for the 7.5 km thick incoming sediment section indicates temperatures at the base of the sediment section of ~150°C, and of ~100°C at 5 km depth (Figure 4.11). A thermal gradient of 25°C/km in the incoming section sediments is predicted (Smith et al. 2013).

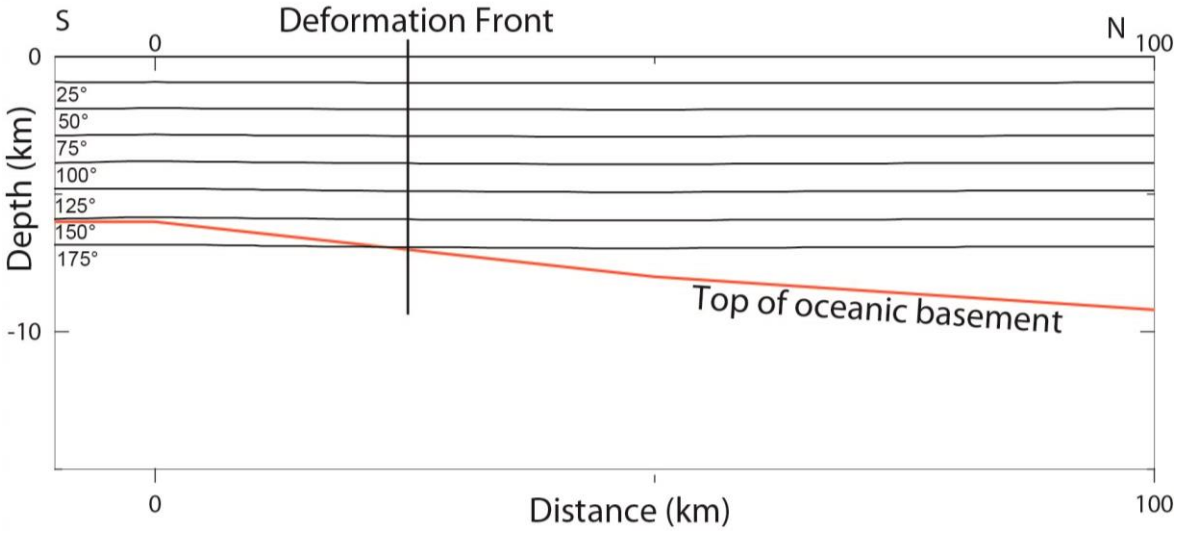

Figure 4.11. 2D thermal profile of the incoming section and frontal ~70 km of the accretionary prism at 62.9°E. The red line indicates the top of basement. Contours are spaced 25°C. Details of the thermal model from Smith et al. (2013).

Figure 4.12 shows the distribution of reflective fault sections, both from east to west along the margin, and with depth compared to the top of basement and the décollement. This plot confirms the observation from Figure 4.7 that the majority of fault reflectivity across the prism occurs in the shallower sediment section with little visible linkage to either the décollement or the deeper sediment section, suggesting that fluid in fault zones is likely sourced from the shallower sediment section.

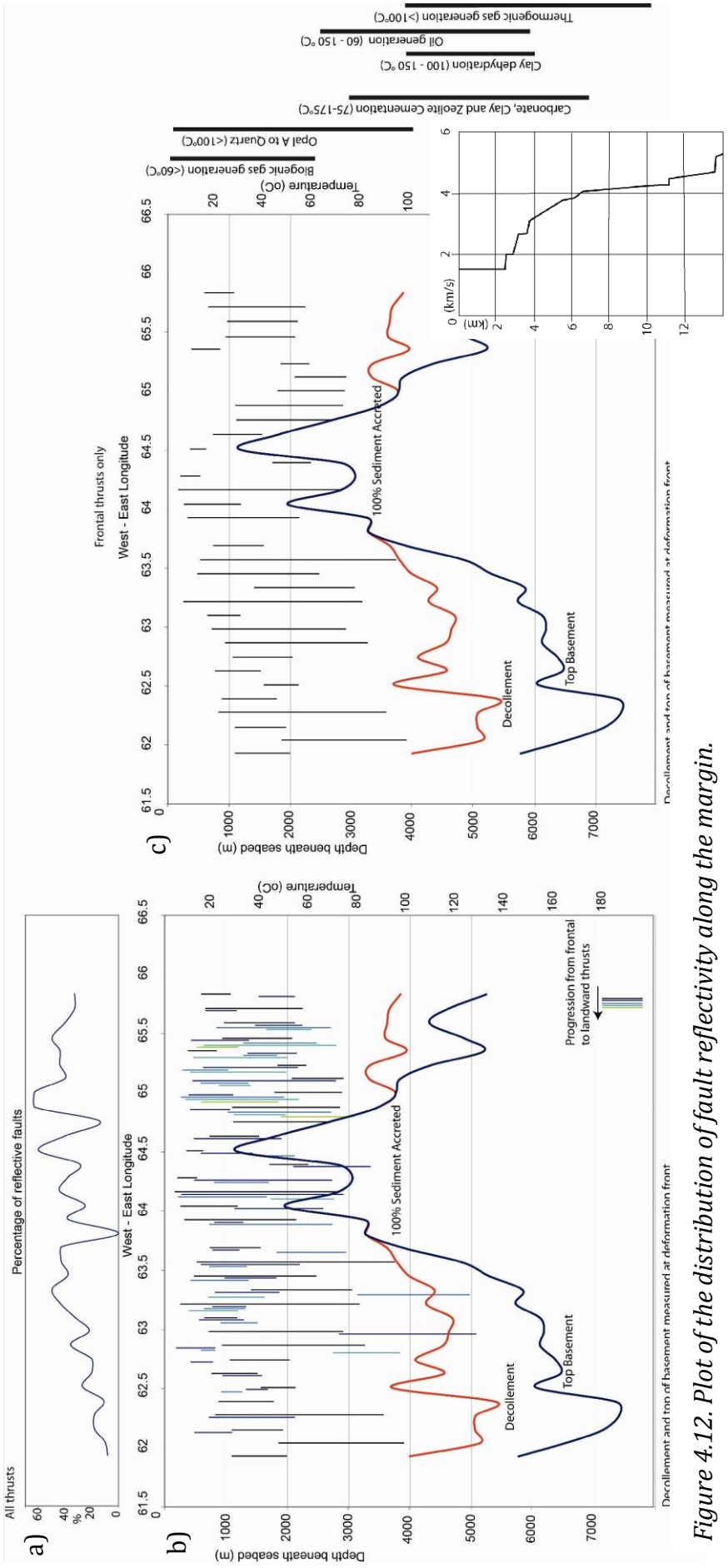

Figure 4.12. Plot of the distribution of fault reflectivity along the margin. a) The upper plot illustrates the percentage of faults which are reflective along each seismic line from the low frequency dataset showing a general eastward increase in fault reflectivity. b) Curves illustrate the depth to basement and décollement at the deformation front. The lines indicate the occurrence of fault reflectivity arranged from east to west, and coloured by how far landward faults are on each line (colours in key on bottom right). These are given in depth below the seabed and then, using the temperature profile of Smith et al. (2013) (Figure 4.9), the estimated temperature at this depth at the deformation front. On the right hand side of the plot are the estimated reaction windows for various fluid producing processes. c) shows the same as b), but just for the frontal thrusts. Inset shows velocity function of Kopp et al. 2000 used for depth conversion.

The temperature profile (Figure 4.11) is used to estimate the positions of mineral dehydration reactions and hydrocarbon production windows in depth context for comparison with fault reflectivity in Figure 4.12 and Figure 4.13. This highlights the position of fault reflectivity at cooler temperatures, within the estimated region of biogenic gas production, and almost entirely shallower than the region where dehydration reactions are expected to occur. Accounting for some uncertainty (~10%) in the reaction temperature windows and the thermal profile, a slightly higher contribution from a deep-fluid source is possible; however the biogenic gas production window still corresponds most favourably to the reflective fault section depths.

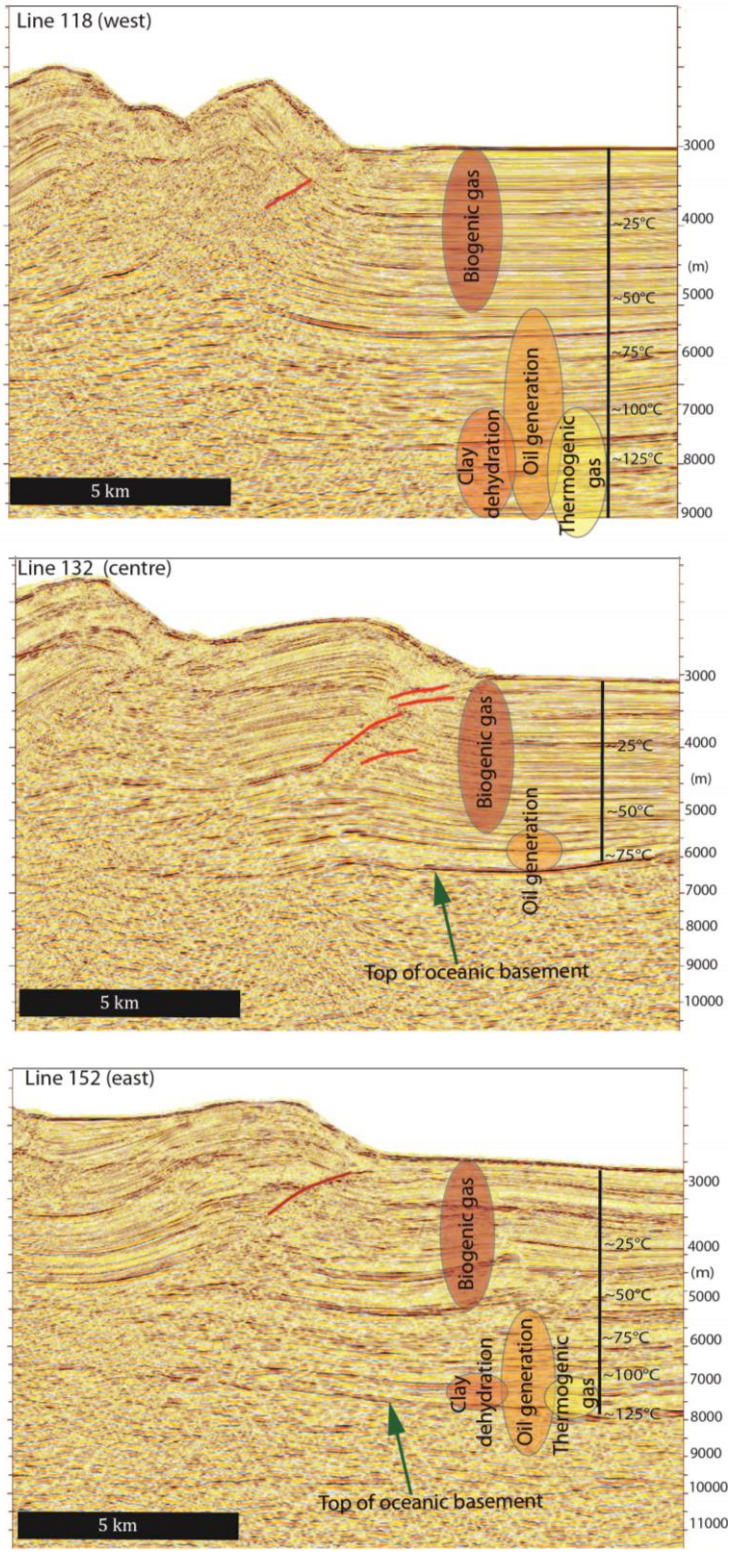

Figure 4.13. Examples of reflective faults and their position relative to the thermal structure of the incoming section. Reflective fault sections interpreted in red. Width of view ~15 km. Estimated depth (velocities from Kopp et al. (2000))/temperature ranges of fluid producing reactions in the sediment section are illustrated by coloured balloons and are as described in Table 4.1*. Thermal structure estimated from Smith et al. 2013.*

4.4 Discussion

Fluids in the form of reflective thrust faults, anticlinal hinge high amplitude (free gas) zones, seafloor seep sites, and the BSR (hydrate) are present to different spatial extents across the Makran accretionary prism. We will discuss how these features may relate to one another, and to the structure and deformation of the prism. The distribution of these features is summarised in Table 4.2.

Feature	West	Centre	East
	Thickest input section (> 7.5 km)	**Region of Little Murray Ridge subduction. Sediment thickness locally reduced to <1 km)**	**Upper input unit (Unit B) pinches out. Max sediment thickness of ~5 km, shallowing to east. Adjacent to N. flank of Murray Ridge**
BSR distribution	> 80% of line length	~70% of line length	50% of line length decreasing eastwards to 15% (more patchy)
Anticlinal hinge high-amplitude gas zones	Highest prevalence, distributed across width of prism	Rare	Low (slightly higher prevalence than central)
Seep sites	Seeps occur on first and sixth ridge (Bohrmann, 2008)	Seeps occur in the frontal and mid prism (in the main canyon) at the base of ridges (von Rad et al., 2000)	Seeps appear quite diffuse in location (von Rad et al., 1996, von Rad et al., 2000)
Fault Reflectivity	~20 – 40% of faults show reflectivity. Distributed across width of prism	0-40% of faults show reflectivity. Concentrated in front 3 thrusts	30-50% of faults show reflectivity. Generally in seaward half of prism.

Table 4.2. Table to compare the spatial distribution of the BSR, high amplitude zones, seep sites and fault reflectivity across the Makran accretionary prism to allow for comparison with changes in structure and the incoming section.

4.4.1 Spatial distribution of the BSR and high amplitude zones, and their relationship to changes in the incoming section

BSR occurrence and continuity shows a gradual decrease from west to east, with the most noticeable feature being the reduction in BSR occurrence in the easternmost section. The eastern section differs from the remainder of the margin in several ways. The incoming section here is dominated by the lower stratigraphic unit (Unit A) which is heavily faulted by normal faults (many of which reach the seabed), rather than the two units present in the west (Smith et al., 2012). The normal faults may facilitate fluid release prior to accretion, reducing the fluid volume within the sediment, and may also continue to provide pathways for fluid escape once accreted. The absence of the second (upper) sedimentary unit may also contribute if it is lithologically distinct from the lower unit and hence has a different fluid generating potential. The eastern prism is also characterised by more complex prism thrust faulting. This denser fault network (of both normal and thrust faults) may enhance dewatering and focus fluid flow along fault planes.

High amplitude zones (and seeps) in the west are loosely concentrated around the sixth ridge, however this is not the case along the remainder of the margin and we propose that the enhanced fluid activity in this region may be due to its location at the confluence of two significant submarine canyons which may promote erosion, slope failure and fluid expulsion. In the central and eastern sections high amplitude patches are less common (Table 4.2), which may be due to the thinner and more faulted incoming section in these regions reducing the potential for fluid trapping in the upper sediments (and also reducing hydrate BSR occurrence as discussed above). Due to the limited area (half of the western section) of the Makran in which seep distribution has been thoroughly investigated it is difficult to discern a clear pattern for their distribution, however, we can infer that they follow a similar distribution to the high amplitude zones given the apparent spatial link between them in the west.

4.4.2 Spatial relationship and origin of high amplitude gas-rich zones and seep sites

In the western region of the Makran there is evidence for a strong spatial correlation between high amplitude zones and seep locations. High amplitude zones tend to occur within anticlinal ridge hinges, often with a corresponding seep site on the overlying crest. It therefore seems reasonable to view these two features as linked and derived from the same source.

The concentration of high amplitude zones and active seeps in the hinges/crests of anticlinal thrust ridges mirrors that seen at Hikurangi: these features are interpreted to be fed by free gas migrating upwards from below the BSR (Barnes et al., 2010). This has also been observed at Hydrate Ridge in Cascadia (Johnson et al., 2003, Riedel et al., 2006). The presence of free gas within the hydrate stability zone (above the BSR) has also been interpreted from seismic reflection data at Blake Ridge, offshore the southeast USA (Gorman et al., 2002), and attributed to a reduced volume of fresh pore water with which to form hydrate and an abundant supply of free gas (Tréhu et al., 2004). Relatively low hydrate concentrations may also increase permeability and facilitate gas migration (Sain et al., 2000). All of these processes fit the observations at the Makran prism.

The vertical migration of free gas across the BSR into shallow sediments at Cascadia (Gorman et al., 2002, Zühlsdorff and Spiess, 2004, Crutchley et al., 2013) and Hikurangi (Netzeband et al., 2010) has been linked with disruptions in the continuity and amplitude of the underlying BSR which may indicate patchiness in hydrate distribution, and/or small-scale faulting which cuts across the BSR (Torres et al., 2004). On the Hikurangi margin, Barnes et al. (2010) and Pecher et al. (2010) observed gaps in the lateral extent of the BSR beneath the anticlinal ridges. These commonly link to high-amplitude regions (and occasional vertical chimney structures) in the shallow sediment suggesting the presence of free gas (Crutchley et al., 2010, Netzeband et al., 2010). Gaps in the BSR are visible at some locations in the Makran (for example in some anticline hinges) (Figure 4.2) but BSR gaps are not associated with all high amplitude zones.

There is evidence in the Makran for small scale shallow normal faulting above the BSR within the hinge zone of many anticlines, which may facilitate gas migration (as suggested for Hikurangi by Pecher et al. (2010)), though these faults do not appear to penetrate down through the BSR. These small normal faults are therefore more likely to provide pathways for gas between the shallow sediment and the seabed, rather than across the BSR. Localised patchiness of the BSR and hydrate, in conjunction with overlying small scale faulting is therefore the most likely explanation for the migration of gas into the shallow section. We also cannot comment on BSR patchiness between our 2D lines. The high amplitude zones visible in the Makran appear to be fed by gas predominantly migrating from landward of the hinge along stratigraphic horizons, with little obvious linkage to the underlying thrust fault (Figure 4.2). Gas may instead migrate along the inclined stratigraphy into the anticlinal hinge zones, where it is able to reach sufficient concentrations to migrate across the BSR into the uppermost sediments to form the high amplitude zones and seep sites.

4.4.3 Spatial distribution of fault reflectivity and relationship to the incoming section, fault activity and shallow fluid features

The distribution of fault reflectivity in the Makran changes along strike from east to west (Table 4.2). In the western and central sections reflective faults are concentrated in the frontal thrusts, but also with some landward examples, particularly in the west. The occurrence of reflective faults further landward in the western section may be due to the sediment section being thickest in this region, therefore providing sufficient fluid even at significant distances from the deformation front. In addition spatial and temporal variations in fault activity may control reflectivity.

Fault activity of the prism thrust faults has been previously analysed, (Smith et al., 2012) with over 75% of the faults visible in this dataset showing some evidence for recent activity, and those which appear to have experienced continuous activity concentrated in the frontal 3-4 thrusts. This seaward concentration of continuous fault activity may also explain the presence of more reflective fault sections here, and

the occurrence of some of the reflective sections further landward appears to be linked to the intermittently active older thrusts, particularly in the western section (Smith et al., 2012). However, the distribution of fault activity does not fully correlate with the observed pattern of fault reflectivity (particularly in the eastern section), and therefore other factors must also contribute.

In the central section, the focussing of fault reflectivity onto the frontal few thrusts may be a result of the incoming Little Murray Ridge. The presence of the basement high may change the stress state of the frontal thrusts, and therefore increase and focus fluid flow. There may also be an increased fluid contribution from the basement itself. Progressing to the eastern section, reflective faults are still concentrated in the seaward region, and a higher percentage of faults are reflective than at any other part of the margin. This is likely due to the denser network of secondary thrusts in this section (Smith et al., 2012) potentially enhancing fault-focused fluid escape. If this is the case and the faults are the main active fluid pathway in the east, we might expect active seeps here to be located along the fault traces, rather than at the hinges of anticlines. Though there is limited data in this region of the Makran, TV-sled photo profiles from Von Rad et al. (1996) do suggest seep sites which are not located at ridge crests. The distribution of fault reflectivity can therefore be mostly explained by changes in the incoming section, deformation style and fault activity but with other unknown factors also contributing (possibly including changes in incoming sediment composition or other internal fault zone properties).

In Eastern Nankai (Chamot-Rooke et al., 1992, Ashi et al., 2002, Henry et al., 2002) and at some regions of Cascadia (Oregon) (Moore et al., 1991) fluid appears to be focused along thrusts. Negative polarity reflective fault sections at depth commonly extend to the seafloor (often with corresponding surface seeps), indicating a dominance of fault-focused fluid flow. South Hikurangi however is similar to the majority of the Makran in that reflective faults show no obvious linkage to the overlying seeps, which are concentrated on ridge crests (Barnes et al., 2010).

Within the shallow section, there does not appear be a direct connection between the high amplitude zones overlying the BSR and the reflective faults (as also previously

concluded by Ding et al. (2010) for the high frequency dataset), and there is an inverse spatial relationship between the two. There are also no seeps confirmed as associated with prism thrust faults, and though some faults do reach the seabed, the shallowest parts of the faults tend to not be reflective. The collapse of over-steepened anticlinal ridges and subsequent burial of the surface fault traces may prevent fluid expulsion at faults.

4.4.4 Fluid sources in the Makran accretionary prism

Our data suggest that fluid-related features (BSR, seeps, high-amplitude zones and reflective faults) in the Makran prism are sourced from the shallow, rather than the deepest, sediment section. In all locations in the Makran fault reflectivity is concentrated in the upper ~4 km of sediments, with faults not showing reflectivity down to the (unreflective) décollement. This suggests that the Makran thrust fault reflectivity is not the result of fluids migrating directly from the deeper sediments and décollement. The shallow reflectivity is more suggestive of fluid sourced from shallower sediments. These results also suggest that the deeper sediment section is relatively dehydrated, as proposed by Smith et al. (2013). This contrasts with observations at Nankai (Henry et al., 2002) and Cascadia (Moore et al., 1991) where faults are reflective through most of their depth and can be often be linked to a reflective décollement, suggesting deeper sourced fluids.

The shallow (< 4 km - defined by where fault reflectivity is concentrated) sediment section in the Makran still provides a large potential fluid source, however sediments at these depths are at insufficient temperatures to drive dehydration reactions and C^{2+} hydrocarbon production. The dominance of a shallow and biogenic source is supported by geochemical data from seep fluids (von Rad et al., 1996, Bohrmann, 2008). The absence of fluid input from the deeper section may be explained by the high (>100°) temperatures at the base of the incoming section predicted by thermal modelling (Smith et al., 2013). This indicates that the lower sediments where the décollement forms are likely to be significantly dehydrated prior to accretion/subduction, and potentially consolidated enough to support seismogenic

rupture. Previously reported high sediment velocities of > 4 km/s (Kopp et al., 2000), velocity/porosity data (Fruehn et al., 1997) and thermal modelling (Smith et al. 2013) also support the hypothesis that the Makran prism may have consolidated, dense sediments at its base. This early dehydration results in a dense, relatively fluid-poor deep input section, and suggests active dehydration and dewatering is restricted to the shallower sediments on accretion.

4.5 Conclusions

- The Makran accretionary prism appears to be dominated by shallow fluid sources, demonstrated by the presence of shallow gas in the anticlinal hinge zones, by reflective faults restricted to the shallower sediment section, and by biogenic sourced seafloor seep fluids. The depth distribution of fault reflectivity also implies that faults are fed by relatively shallowly generated fluids.
- The deeper (>~4 km) sediment section is relatively dewatered /dehydrated and compacted, as previously indicated by geophysical data (Fruehn et al., 1997), and is not the source of the observed shallow fluid/gas structures. The shallower sediments are still sufficiently deeply buried within the accretionary prism to continue to generate and release fluids.
- Variations in the spatial distribution of the BSR, high amplitude zones, seeps and reflective fault sections from east to west appear to be primarily controlled by changes in the incoming section – specifically the density of normal faulting, presence of basement highs in the central and eastern areas and changes in the incoming stratigraphy.
- When compared to other global subduction zones the Makran appears to be most similar to South Hikurangi, in terms of its fluid properties, due to the dominance of fluid escape via shallow normal fault structures, and the lack of visible linkage between deeper reflective faults and shallow fluid features.

5 Chapter 5. Conclusions and Future Work

This thesis presents a comprehensive study of the structure, fluid distribution and seismogenic potential of the Makran subduction zone, a margin which had previously been understudied when compared to many global subduction zones. This study reveals many interesting features of the margin. Chapter 2 uses seismic reflection and bathymetry datasets to construct a structural model of the Makran, a detailed interpretation of the imbricate thrust faults and basement structure, and an analysis of décollement location and properties. It is clear that, despite the unusually thick incoming sediment section, the accretionary prism structure of the Makran is relatively comparable to other margins such as Hikurangi and parts of Cascadia, with a low taper and simple imbricate structure. Interestingly, the seaward vergence of the Makran structures is more typical of conventional prisms rather than the landward vergence often attributed to low basal shear stress, which is in turn linked to low wedge taper (Gutscher et al., 2001). The Makran is more similar to the Lesser Antilles, which has a thick input section generating seaward vergent wedge structures, rather than the relatively thick input sections of the Cascadia and N. Sumatran margins which are associated with areas of landward vergence.

The thick sediment incoming section does however appear to affect the seismogenic potential of the Makran. Combining décollement picks from Chapter 2 and thermal modelling results from Chapter 3, we can conclude that the plate boundary fault beneath the outer accretionary prism occurs within the deep sediment section, and at sufficiently high temperatures to be seismogenic due to the thick overlying section, with important implications for regional hazard assessments. As a result of this thermal modelling we predict potential earthquake magnitudes of up to M_w9.2 at the Makran subduction zone. The thermal model produced in Chapter 3 is also utilised in understanding the potential fluid generation processes and the distribution of fluid indicators mapped in Chapter 4. The mapping (both spatially and with depth) of the BSR, high amplitude gas zones and likely porous, fluid-rich fault zones (reflective faults) suggests that the Makran accretionary prism is dominated by shallow fluid expulsion and that the deep sediment section contributes little to the current fluid

system. This low fluid input from the deep section supports the results of both Chapters 2 and 3 - that the décollement and deep sediment section appear to be dehydrated and normally compacted, rather than weak and overpressured. This is perhaps the most significant result from this thesis, as previous estimations of subduction zone hazards have considered those margins with thick incoming sediment sections, including the Makran, as likely to have a weak, overpressured base. It is possible that the sediments in the Makran are relatively permeable, and therefore allow fluid escape (both from compaction dewatering and diagentic reactions) despite the thickness of the section, therefore preventing the formation of an overpressured zone in the deeper sediment section.

5.1 Key conclusions from each chapter

The following section will endeavour to answer the questions posed in the introduction (Chapter 1) for each chapter.

Chapter 2 - Structure and Fault Activity of the Makran Accretionary Prism

(Q2.1). What is the dominant structural style of the Makran accretionary prism and how does this vary with incoming sediment thickness/basement topography?

The Makran accretionary prism is dominated by simple, seaward verging, imbricate thrust structures, with a relatively consistent fault spacing of ~6 km. These thrusts form anticlinal ridges, some of which can be followed along strike for over 100 km. Piggyback basins have formed between these ridges, locally trapping sediment. The most noticeable change in structure along strike is the local increase in fault spacing to 18 km in the region where the elevated basement of the Little Murray Ridge is being subducted, causing the deformation front to step seaward. Basement topography also affects the eastern end of the accretionary prism where the northern flank of the Murray Ridge approaches the subduction zone influencing sediment transport and reducing the thickness of the incoming section. At the deformation front the incoming section is partitioned into accreted and subducted sediment, separated by a décollement horizon. This décollement horizon occurs within the

sediment section, except in the region of reduced sediment thickness over the Little Murray Ridge where the décollement steps onto the top-basement surface, accreting the entire sediment section. Décollement properties are discussed further in Q2.4.

(Q2.2). How does the unusually thick incoming sediment section affect the structure and prism taper of the Makran?

Despite the thick incoming section, fault spacing in the Makran is similar to that observed at margins with substantially thinner accreted sections; and the thrust deformation convincingly extends to the interpreted décollement, rather than to a shallower level. A wedge taper of 4.5° classifies the Makran as a low taper margin, comparable to parts of the Lesser Antilles, Hikurangi and Cascadia. These results suggest that the unusually high sediment input of the Makran is not generating particularly unusual structural behaviour in the offshore prism. However, analogue models have suggested that high sediment input margins such as the Makran may differ mechanically from classic Coulomb wedges, and may instead be sub-critical and actively deforming in response to the high levels of frontal accretion (e.g. Storti and McClay, 1995). Therefore though the thick incoming section does not appear to produce unusual structural behaviour in the Makran, it may have led to the development of a sub-critical wedge.

(Q2.3). How is activity and deformation distributed between the accretionary prism imbricate thrust faults and how does this vary along strike?

Fault activity in the Makran was investigated through an analysis of the geometry of piggyback basin sediments and the thrust faults themselves. These analyses reveal that over 75% of the faults in the Makran show some evidence for recent activity, including some over 50 km from the deformation front. However the inactive faults still tend to be concentrated in the landward region of our dataset. Fault activity in the easternmost part of the prism is more concentrated onto the frontal thrusts, while activity is more widely distributed across the prism in the west and central regions. The widely distributed fault activity observed in the majority of the Makran is contrary to traditional models of accretionary prism growth which predict fault

activity to be focused on the frontal few thrusts. This distributed activity may be a further result of the Makran developing as a sub-critical wedge (see Q 2.2) which is internally deforming in response to high levels of accretion. The reduction in fault activity in the east of the study area may be due to increased sediment blanketing which has been suggested by analogue models to inhibit fault reactivation through increasing the normal stress on the fault (Storti and McClay, 1995).

(Q2.4). What can we infer about the décollement properties of the Makran and what implications do they have for the seismogenic potential of the margin?

The décollement horizon in the Makran generally occurs within the deep sediment section (see Q 2.1). It does not appear as a reflective horizon, in contrast to many other margins worldwide at which a strong décollement reflector has been observed, however its position stratigraphically can be picked with reasonable certainty based on the extent of wedge deformation. This lack of reflectivity and specifically lack of a negative polarity reflector, in conjunction with previously collected geophysical data, suggests that the décollement in the Makran may not be a weak, overpressured horizon as often inferred for high-sediment input, low-taper margins, and may instead be stronger than expected. High sediment velocities in the deepest sediments of the Makran accretionary prism of >4 km/s (comparable to those seen at depth in the Sumatra 2004 rupture area) indicate that these sediments may be sufficiently consolidated to support seismogenic rupture. When combined with a décollement surface with no major physical property changes across the interface (no reflection), this indicates an increased potential for seismogenic rupture beneath the prism, with implications for tsunamigenesis.

Chapter 3 - Thermal structure and megathrust seismogenic potential of the Makran subduction zone

(Q3.1). What is the thermal structure of the Makran subduction zone, and how does this relate to the incoming section (sediment thickness) and plate geometry?

The primary controls on the thermal structure of the Makran forearc and subducting plate are its thick incoming sediment section and shallow subducting plate geometry. The thick incoming section means that the deepest input sediments and plate boundary reach temperatures of over 100°C seaward of the deformation front. The shallow dip of the subducting plate leads to a slow rate of heat loss with distance from the deformation front. Assuming a thermal seismogenic zone of between 150°C - 350°C these features combine to produce a wide (>350 km) potential seismogenic zone, with potential seismogenic behaviour updip to the deformation front.

(Q3.2). Based on this thermal modelling, what are the maximum potential earthquake magnitudes which could be generated at the Makran?

The thermal structure generated by our model produces potential slip widths of 210-355 km. These widths were then combined with three along-strike rupture scenarios, accounting for potential rupture barriers. The longest rupture of 800 km encompasses the full length of the subduction zone, the second scenario (400 km) uses the historically more seismically active Pakistan half of the margin, and the third scenario (220 km) includes the possible impediment of rupture by the Little Murray Ridge. Combining these scenarios produced a potential earthquake magnitude range of M_w 8.7-9.2 with significant local and regional tsunami hazard potential. All our rupture scenarios include a degree of both offshore and onshore rupture, therefore posing both shaking and tsunami hazards to coastal communities.

Chapter 4 - Fluid generation and distribution in the highest sediment input accretionary margin, the Makran

(Q4.1). What is the distribution of fluid-related features in the Makran accretionary prism?

The Makran accretionary prism exhibits a BSR, shallow high amplitude zones (gas), seabed seeps, and potential low density/high porosity, likely fluid-rich fault zones (reflective faults), all with varying spatial extents. A clear BSR is present across the majority of the margin, but with its occurrence reducing in the easternmost Makran.

The high amplitude zones occur in the shallow sediment section above the BSR (and hence in the expected hydrate zone) and are concentrated in anticlinal hinge zones of the imbricate thrust faults. They occur most commonly in the west of our study area and tend to correlate with surface seeps. In the central and eastern areas high amplitude zones are less common but do still occasionally occur (we do not have seep data for comparison in these regions). Reflective sections of thrust faults, inferred to indicate fluid occurrence, are generally concentrated within the frontal 3-4 thrusts, though there is some occurrence landward particularly in the west. There is an increased concentration of fault reflectivity in the frontal thrusts in the central and eastern sections of our study area.

(Q4.2). How is fluid distribution in the Makran related to changes in the incoming section and prism structure?

A noticeable feature when looking at the spatial distribution of fluids in the Makran is the change in distribution/presence of fluid-related features from west to east along strike. The easternmost Makran shows a higher incidence of thrust fault reflectivity within the wedge, but a lower incidence of high amplitude zones and the BSR. This may be due to the increase in fault density in this region, with widespread normal faulting in the incoming section and more secondary thrusts in the prism itself potentially increasing permeability and favouring fluid escape along more permeable faults, rather than allowing accumulation in the upper sediments. The region overlying the Little Murray Ridge also shows enhanced fault reflectivity relative to adjacent regions, perhaps due to the incoming basement high focusing fluid flow in this region. The relationship between fault reflectivity and fault activity is rather unclear, as fault activity reduces in the east, where reflectivity tends to increase. However in the west, localised reflectivity in the landward region may be related to the reactivation of older thrusts. Seep sites and high amplitude zones occur in the anticlinal hinge zones of the thrust faults, and so are structurally controlled, though they are not directly fed by the thrust faults.

(Q4.3). What are the potential fluid sources and how do these relate to the thermal structure of the margin?

The primary fluid source in the Makran is the thick incoming sediment section. This section will release pore fluids due to compaction and deformation-related dewatering, while processes such as mineral dehydration and hydrocarbon production occur at higher temperatures releasing/generating additional fluids. The thermal structure of the Makran, with temperatures in excess of over 100°C in the lower sediment section, suggests that the deepest sediment may be largely compacted, dehydrated and high density prior to subduction, supported by velocities of >4 km in the lower sediment section (Fruehn et al., 1997, Kopp et al., 2000). As a result the shallow sediment section is a more likely source for fluid in the accretionary prism. This is supported by the vertical distribution of fault reflectivity which is concentrated in the upper ~3 km of the accretionary prism. In addition there is no visible linkage between the reflective fault sections and the décollement suggesting that fluids are not being channelled from depth along the décollement and then to the thrust faults. This predominantly shallow source is also supported by previously collected geochemical data which indicates a dominance of shallow sourced biogenic/microbial methane at the seabed seeps. These results support the presence of a dehydrated lower sediment section which does not exert a significant control on the observed shallow fluid structures.

5.2 Summary

The conclusions reached in this thesis indicate that the Makran is an unusual and globally significant subduction zone. Its large accretionary prism, fed by the exceptionally thick input sediment section, is structurally simple when compared to many other margins, exemplified by its remarkably consistent fault spacing and simple fault structures. Fault activity is fairly widely distributed across the prism, agreeing with analogue models which predict a similar pattern for high sediment input margins. The low (4.5°) taper of the Makran prism suggests low basal shear stress; however this may instead be a function of internal wedge properties. The

Makran prism may also have evolved as a sub-critical wedge due to its high levels of frontal accretion. The observed features of the Makran cannot necessarily be explained by a weak basal surface (as often proposed for high sediment input margins), as both our interpretations of the unreflective décollement surface, and our thermal modelling results suggest otherwise. Our results suggest that, at depth, the sediments of the Makran may be compacted, dehydrated and therefore stronger than predicted. This is further supported by the lack of contribution from the deeper section to the observed fluid features in the Makran, and previously collected geophysical data (Fruehn et al., 1997, Kopp et al., 2000). This study therefore has important implications for the deformation and evolution of high sediment input accretionary margins, and for their seismogenic potential.

5.3 Future work highlighted by this thesis

Several potential avenues of further study have been highlighted by this research. These are described below and grouped by research topic.

Structural investigations

- Due to its unreflective nature the interpretations of décollement position presented are based on a) downward extrapolation of the observed listric thrust fault planes, and b) identifying the interface between deformed and undeformed stratigraphy. These interpretations could be improved by undertaking structural restoration of the frontal prism thrusts, similar to that undertaken for Nankai (Moore et al., 2011). Restorations of this nature, which can be undertaken using 2D Move (Midland Valley), require a depth converted section and confident interpretation of stratigraphic horizons across faults, both of which may not be straightforward for the Makran. However, a structural restoration of the frontal thrusts would help to validate our décollement interpretations.
- Structural restorations of this nature would also allow an assessment of the displacement history and deformation changes along strike of the frontal

thrust, and how these relate to the morphology of the frontal ridge, incoming basement features and changes in the incoming section along strike.

- The extension of the 2D seismic reflection dataset further landward may provide interesting information regarding the progression of deformation northwards. Data from the Iranian half of the margin, just to the west of the Iran/Pakistan border, indicate that the landward part of the prism is overlain by thick sediments, dominated by large extensional faults, mud diapirism and possible sediment underplating, and may represent a forarc basin of some kind (Grando and McClay, 2007), although compressional deformation clearly continues onshore (a clear fold-thrust belt is observed) (Figure 1.1). This contrasts with the simple imbricate thrusts seen in the seaward prism. It would therefore be informative to establish if this pattern continues into the Pakistan side of the Makran.
- The inclusion of data from the Iranian margin into our structure map would also provide a more complete structural interpretation of the prism, allowing the entire Makran accretionary prism to be investigated.
- An extension of the high frequency dataset along strike would allow shallow sedimentary features (e.g. fluid-related features) to be studied in greater detail.
- The Makran accretionary prism continues for over 200 km north of the coastline, and the aridity of the climate in this region means that many structures are easily identifiable from satellite imagery. An integration of our offshore structure map with features identified onshore may provide an interesting comparison in terms of structural style, and the progression of deformation through the prism.

Sediment properties and transport

- An ongoing source of uncertainty in the Makran region is the exact source of the input section, the relationship between the stratigraphy on the northern and southern sides of the Murray Ridge, and hence how the Makran input section is linked to the Indus Fan. Sediments north of the Murray Ridge (and hence Makran input sediments) may have a more mixed provenance with components from the Indus Fan, more proximal fluvial sources, and Oman margin sediments. Sediment packages on either side of the transtensional

Murray Ridge are separated by a transtensional rift trough (the Dalrymple Trough) over 3 km deep (Edwards et al., 2008). Correlating these two sediment packages would improve our understanding of the Makran input section, provide a chronology for the input section and would indicate how the Murray Ridge has developed through time and influenced the regional tectonics. This would also be aided by a higher density of shallow cores and deeper boreholes in the region. Boreholes located in the western, thickest sediment section and in the eastern region close to the Murray Ridge would be particularly informative, and additional sites over the Little Murray Ridge could also be considered.

Heat flow and seismic hazard

- The collection of additional heat flow data, both from offshore and onshore, would help to constrain and reinforce the thermal model presented in Chapter 3. Current heat flow data is clustered around the frontal ~60 km of the accretionary prism, so a more widespread dataset (of both direct and BSR-derived measurements) would be very beneficial.
- Information from GPS data regarding the degree of coupling between the upper and lower plates would allow a more accurate estimation of the degree of seismic hazard in the Makran.
- Perhaps most pertinently, there is a need for the potential seismic hazard posed by the Makran to be further explored, and to be acknowledged and understood by the nations potentially affected by any large earthquake or tsunami events in this region. The installation of a local onshore seismic network would allow a greater understanding of the seismicity of the Makran (and further constrain our thermal model). This would be further aided by increased examinations of the palaeoseismological and palaeotsunami record onshore, building on efforts initiated after the 2004 Aceh-Andaman earthquake. Finally, the installation of a tsunami warning system and evacuation plan may help to mitigate against future hazards in this region.

6 Chapter 6. References

ADAM, J., KLAESCHEN, D., KUKOWSKI, N. & FLUEH, E. (2004) Upward delamination of Cascadia Basin sediment infill with landward frontal accretion thrusting caused by rapid glacial age material flux. *Tectonics,* 23 (3), 21, TC3009.

AHMED, S. S. (1969) Tertiary geology of Part of South Makran, Baluchistan, West Pakistan. *AAPG Bulletin-American Association of Petroleum Geologists,* 53 (7), 1480-1499.

ARRÁIZ, D. & SPIESS, V. (2012) Identification of gas related features as imaged by two different acquisition systems at the accretionary margin of the Makran. *Masters Project, Universität Bremen*.

ASHI, J., TOKUYAMA, H. & TAIRA, A. (2002) Distribution of methane hydrate BSRs and its implication for the prism growth in the Nankai Trough. *Marine Geology,* 187 (1-2), 177-191.

BANGS, N. L., SHIPLEY, T. H., GULICK, S. P. S., MOORE, G. F., KUROMOTO, S. & NAKAMURA, Y. (2004) Evolution of the Nankai Trough décollement from the trench into the seismogenic zone: Inferences from three-dimensional seismic reflection imaging. *Geology,* 32 (4), 273-276.

BANGS, N. L. B., SHIPLEY, T. H., MOORE, J. C. & MOORE, G. F. (1999) Fluid accumulation and channelling along the northern Barbados Ridge decollement thrust. *Journal of Geophysical Research-Solid Earth,* 104 (B9), 20399-20414.

BANGS, N. L. B., WESTBROOK, G. K., LADD, J. W. & BUHL, P. (1990) Seismic velocities from the Barbados Ridge Complex - indicators of high pore fluid pressures in an accretionary complex. *Journal of Geophysical Research-Solid Earth and Planets,* 95 (B6), 8767-8782.

BARKER, D. H. N., SUTHERLAND, R., HENRYS, S. & BANNISTER, S. (2009) Geometry of the Hikurangi subduction thrust and upper plate, North Island, New Zealand. *Geochemistry Geophysics Geosystems,* 10, 23, Q02007.

BARNES, P. M., LAMARCHE, G., BIALAS, J., HENRYS, S., PECHER, I., NETZEBAND, G. L., GREINERT, J., MOUNTJOY, J. J., PEDLEY, K. & CRUTCHLEY, G. (2010) Tectonic and geological framework for gas hydrates and cold seeps on the Hikurangi subduction margin, New Zealand. *Marine Geology,* 272 (1-4), 26-48.

BELL, R., SUTHERLAND, R., BARKER, D. H. N., HENRYS, S., BANNISTER, S., WALLACE, L. & BEAVAN, J. (2010) Seismic reflection character of the Hikurangi subduction interface, New Zealand, in the region of repeated Gisborne slow slip events. *Geophysical Journal International,* 180 (1), 34-48.

BIGI, S., DI PAOLO, L., VADACCA, L. & GAMBARDELLA, G. (2010) Load and unload as interference factors on cyclical behavior and kinematics of Coulomb wedges: Insights from sandbox experiments. *Journal of Structural Geology,* 32 (1), 28-44.

BIJWAARD, H., SPAKMAN, W. & ENGDAHL, E. R. (1998) Closing the gap between regional and global travel time tomography. *Journal of Geophysical Research,* 103 (B12), 30055-30078.

BOHRMANN, G. (2008) Report and Preliminary Results of R/V METEOR Cruise M74/3, Fujairah - Male, 30 October - 28 November 2007. Cold Seeps of the Makran Subduction Zone (Continental Margin of Pakistan). *Berichte Fachbereich Geowissenschaften, Universitat Bremen,* 266, 1 -161.

BOURGET, J., ZARAGOSI, S., ELLOUZ-ZIMMERMANN, N., MOUCHOT, N., GARLAN, T., SCHNEIDER, J. L., LANFUMEY, V. & LALLEMANT, S. (2011) Turbidite system architecture and sedimentary processes along topographically complex slopes: the Makran convergent margin. *Sedimentology,* 58 (2), 376-406.

BOURGET, J., ZARAGOSI, S., ELLOUZ-ZIMMERMANN, S., DUCASSOU, E., PRINS, M. A., GARLAN, T., LANFUMEY, V., SCHNEIDER, J. L., ROUILLARD, P. & GIRAUDEAU, J. (2010) Highstand vs. lowstand turbidite system growth in the Makran active margin: Imprints of high-frequency external controls on sediment delivery mechanisms to deep water systems. *Marine Geology,* 274 (1-4), 187-208.

BUFFETT, B. A. (2000) Clathrate Hydrates. *Annual Review of Earth and Planetary Sciences,* 28 (1), 477-507.

BYRNE, D. E., DAVIS, D. M. & SYKES, L. R. (1988) Loci and maximum size of thrust earthquakes and the mechanics of the shallow region of subduction zones. *Tectonics,* 7 (4), 833-857.

BYRNE, D. E., SYKES, L. R. & DAVIS, D. M. (1992) Great thrust earthquakes and aseismic slip along the plate boundary of the Makran Subduction Zone. *Journal of Geophysical Research-Solid Earth,* 97 (B1), 449-478.

BYRNE, T. & FISHER, D. (1990) Evidence for a Weak and Overpressured Décollement Beneath Sediment-Dominated Accretionary Prisms. *J. Geophys. Res.,* 95 (B6), 9081-9097.

CARSON, B. & SCREATON, E. J. (1998) Fluid flow in accretionary prisms: Evidence for focused, time-variable discharge. *Reviews of Geophysics,* 36 (3), 329-351.

CHAMOT-ROOKE, N., LALLEMANT, S. J., LE PICHON, X., HENRY, P., SIBUET, M., BOULGÈUE, J., FOUCHER, J. P., FURUTA, T., GAMO, T., GLAÇON, G., KOBAYASHI, K., KURAMOTO, S., OGAWA, Y., SCHULTHEISS, P., SEGAWA, J., TAKEUCHI, A., TARITS, P. & TOKUYAMA, H. (1992) Tectonic context of fluid venting at the toe of the eastern Nankai accretionary prism: Evidence for a shallow detachment fault. *Earth and Planetary Science Letters,* 109 (3-4), 319-332.

CHANG, C. P., CHANG, T. Y., ANGELIER, J., KAO, H., LEE, J. C. & YU, S. B. (2003) Strain and stress field in Taiwan oblique convergent system: constraints from GPS observation and tectonic data. *Earth and Planetary Science Letters,* 214 (1-2), 115-127.

CHLIEH, M., AVOUAC, J. P., HJORLEIFSDOTTIR, V., SONG, T. R. A., JI, C., SIEH, K., SLADEN, A., HEBERT, H., PRAWIRODIRDJO, L., BOCK, Y. & GALETZKA, J. (2007) Coseismic slip and afterslip of the great M-w 9.15 Sumatra-Andaman earthquake of 2004. *Bulletin of the Seismological Society of America,* 97 (1), S152-S173.

CLIFT, P., GAEDICKE, C., EDWARDS, R., LEE, J. I., HILDEBRAND, P., AMJAD, S., WHITE, R. S. & SCHLUTER, H. U. (2002) The stratigraphic evolution of the Indus Fan and the history of sedimentation in the Arabian Sea. *Marine Geophysical Researches,* 23 (3), 223-245.

CLIFT, P. D., SHIMIZU, N., LAYNE, G. D., BLUSZTAJN, J. S., GAEDICKE, C., SCHLUTER, H. U., CLARK, M. K. & AMJAD, S. (2001) Development of the Indus Fan and its significance for the erosional history of the Western Himalaya and Karakoram. *Geological Society of America Bulletin,* 113 (8), 1039-1051.

CRUTCHLEY, G. J., BERNDT, C., GEIGER, S., KLAESCHEN, D., PAPENBERG, C., KLAUCKE, I., HORNBACH, M. J., BANGS, N. L. B. & MAIER, C. (2013) Drivers of focused fluid flow and methane seepage at south Hydrate Ridge, offshore Oregon, USA. *Geology,* 41, 551-554.

CRUTCHLEY, G. J., PECHER, I. A., GORMAN, A. R., HENRYS, S. A. & GREINERT, J. (2010) Seismic imaging of gas conduits beneath seafloor seep sites in a shallow marine gas hydrate province, Hikurangi Margin, New Zealand. *Marine Geology,* 272, 114-126.

CURRIE, C. A. & HYNDMAN, R. D. (2006) The thermal structure of subduction zone back arcs. *Journal of Geophysical Research,* 111 (B8), B08404.

CURRIE, C. A., WANG, K., HYNDMAN, R. D. & HE, J. (2004) The thermal effects of steady-state slab-driven mantle flow above a subducting plate: the Cascadia subduction zone and backarc. *Earth and Planetary Science Letters,* 223 (1â€“2), 35-48.

DAHLEN, F. A. (1990) Critical taper model of fold-and-thrust belts and accretionary wedges. *Annual Review of Earth and Planetary Sciences,* 18, 55-99.

DAHLEN, F. A., SUPPE, J. & DAVIS, D. (1984) Mechanics of fold-and-thrust belts and accretionary wedges - Cohesive Coulomb Theory. *Journal of Geophysical Research,* 89 (NB12), 87-101.

DAVIS, D., SUPPE, J. & DAHLEN, F. A. (1983) Mechanics of fold-and-thrust belts and accretionary wedges. *Journal of Geophysical Research,* 88 (NB2), 1153-1172.

DEAN, S. M., MCNEILL, L. C., HENSTOCK, T. J., BULL, J. M., GULICK, S. P. S., AUSTIN, J. A., BANGS, N. L. B., DJAJADIHARDJA, Y. S. & PERMANA, H. (2010) Contrasting Décollement and Prism Properties over the Sumatra 2004-2005 Earthquake Rupture Boundary. *Science,* 329 (5988), 207-210.

DELISLE, G. D., VON RAD, U. V. R., ANDRULEIT, H. A., VON DANIELS, C. V. D., TABREZ, A. T. & INAM, A. I. (2002) Active mud volcanoes on- and offshore eastern Makran, Pakistan. *International Journal of Earth Sciences,* 91 (1), 93-110.

DEMETS, C., GORDON, R. G. & ARGUS, D. F. (2010) Geologically current plate motions. *Geophysical Journal International,* 181 (1), 1-80.

DEMETS, C., GORDON, R. G., ARGUS, D. F. & STEIN, S. (1990) Current Plate Motions. *Geophysical Journal International,* 101 (2), 425-478.

DING, F., SPIESS, V., FEKETE, N., MURTON, B., BRÜNING, M. & BOHRMANN, G. (2010) Interaction between accretionary thrust faulting and slope sedimentation at the frontal Makran accretionary prism and its implications for hydrocarbon fluid seepage. *Journal of Geophysical Research,* 115 (B8), B08106.

DONATO, S. V., REINHARDT, E. G., BOYCE, J. I., PILARCZYK, J. E. & JUPP, B. P. (2009) Particle-size distribution of inferred tsunami deposits in Sur Lagoon, Sultanate of Oman. *Marine Geology,* 257 (1-4), 54-64.

EDWARDS, R. A., MINSHULL, T. A., FLUEH, E. R. & KOPP, C. (2008) Dalrymple Trough: An active oblique-slip ocean-continent boundary in the northwest Indian Ocean. *Earth and Planetary Science Letters,* 272 (1-2), 437-445.

EDWARDS, R. A., MINSHULL, T. A. & WHITE, R. S. (2000) Extension across the Indian-Arabian plate boundary: The Murray Ridge. *Geophysical Journal International,* 142 (2), 461-477.

ENGDAHL, E. R., VAN DER HILST, R. & BULAND, R. (1998) Global teleseismic earthquake relocation with improved travel times and procedures for depth determination. *Bulletin of the Seismological Society of America,* 88 (3), 722-743.

FARHOUDI, G. & KARIG, D. E. (1977) Makran of Iran and Pakistan as an active arc system. *Geology,* 5 (11), 664-668.

FOWLER, S. R., WHITE, R. S. & LOUDEN, K. E. (1985) Sediment dewatering in the Makran accretionary prism. *Earth and Planetary Science Letters,* 75 (4), 427-438.

FRUEHN, J., WHITE, R. S. & MINSHULL, T. A. (1997) Internal deformation and compaction of the Makran accretionary wedge. *Terra Nova,* 9 (3), 101-104.

FUJIWARA, T., KODAIRA, S., NO, T., KAIHO, Y., TAKAHASHI, N. & KANEDA, Y. (2011) The 2011 Tohoku-Oki Earthquake: Displacement Reaching the Trench Axis. *Science,* 334 (6060), 1240.

FULLER, C. W., WILLETT, S. D. & BRANDON, M. T. (2006) Formation of forearc basins and their influence on subduction zone earthquakes. *Geology,* 34 (2), 65-68.

GAEDICKE, C., SCHLUTER, H. U., ROESER, H. A., PREXL, A., SCHRECKENBERGER, B., MEYER, H., REICHERT, C., CLIFT, P. & AMJAD, S. (2002) Origin of the northern Indus Fan and Murray Ridge, Northern Arabian Sea: interpretation from seismic and magnetic imaging. *Tectonophysics,* 355 (1-4), 127-143.

GORMAN, A. R., HOLBROOK, W. S., HORNBACH, M. J., HACKWITH, K. L., LIZARRALDE, D. & PECHER, I. (2002) Migration of methane gas through the hydrate stability zone in a low-flux hydrate province. *Geology,* 30 (4), 327-330.

GRANDO, G. & MCCLAY, K. (2007) Morphotectonics domains and structural styles in the Makran accretionary prism, offshore Iran. *Sedimentary Geology,* 196 (1-4), 157-179.

GREVEMEYER, I., ROSENBERGER, A. & VILLINGER, H. (2000) Natural gas hydrates on the continental slope off Pakistan: constraints from seismic techniques. *Geophysical Journal International,* 140 (2), 295-310.

GULICK, S. P. S., AUSTIN, J. A., MCNEILL, L. C., BANGS, N. L. B., MARTIN, K. M., HENSTOCK, T. J., BULL, J. M., DEAN, S., DJAJADIHARDJA, Y. S. & PERMANA, H. (2011) Updip rupture of the 2004 Sumatra earthquake extended by thick indurated sediments. *Nature Geoscience,* 4 (7), 453-456.

GULICK, S. P. S., BANGS, N. L. B., SHIPLEY, T. H., NAKAMURA, Y., MOORE, G. & KURAMOTO, S. (2004) Three-dimensional architecture of the Nankai accretionary prism's imbricate thrust zone off Cape Muroto, Japan: Prism reconstruction via en echelon thrust propagation. *Journal of Geophysical Research-Solid Earth,* 109 (B2), 12, B02105.

GUTSCHER, M. A., KLAESCHEN, D., FLUEH, E. & MALAVIEILLE, J. (2001) Non-Coulomb wedges, wrong-way thrusting, and natural hazards in Cascadia. *Geology,* 29 (5), 379-382.

GUTSCHER, M. A., KUKOWSKI, N., MALAVIEILLE, J. & LALLEMAND, S. (1996) Cyclical behavior of thrust wedges: Insights from high basal friction sandbox experiments. *Geology,* 24 (2), 135-138.

GUTSCHER, M. A., KUKOWSKI, N., MALAVIEILLE, J. & LALLEMAND, S. (1998) Episodic imbricate thrusting and underthrusting: Analog experiments and mechanical analysis applied to the Alaskan accretionary wedge. *Journal of Geophysical Research-Solid Earth,* 103 (B5), 10161-10176.

GUTSCHER, M. A. & PEACOCK, S. M. (2003) Thermal models of flat subduction and the rupture zone of great subduction earthquakes. *Journal of Geophysical Research,* 108 (B1).

GUTSCHER, M. A. & WESTBROOK, G. K. (2009) Great Earthquakes in Slow-Subduction, Low-Taper Margins. IN LALLEMAND, S. & FUNICIELLO, F. (Eds.) *Subduction Zone Geodynamics.* Berlin, Springer-Verlag Berlin.119-133

HAACKE, R. R., WESTBROOK, G. K. & HYNDMAN, R. D. (2007) Gas hydrate, fluid flow and free gas: Formation of the bottom-simulating reflector. *Earth and Planetary Science Letters,* 261 (3/4), 407-420.

HAMAMOTO, H., YAMANO, M., GOTO, S., KINOSHITA, M., FUJINO, K. & WANG, K. (2011) Heat flow distribution and thermal structure of the Nankai subduction zone off the Kii Peninsula. *Geochemistry Geophysics Geosystems,* 12, Q0AD20.

HANKS, T. C. & KANAMORI, H. (1979) A Moment Magnitude Scale. *Journal of Geophysical Research,* 84 (B5), 2348-2350.

HARDY, S., DUNCAN, C., MASEK, J. & BROWN, D. (1998) Minimum work, fault activity and the growth of critical wedges in fold and thrust belts. *Basin Research,* 10 (3), 365-373.

HEIDARZADEH, M., PIROOZ, M. D. & ZAKER, N. H. (2009) Modeling the near-field effects of the worst-case tsunami in the Makran subduction zone. *Ocean Engineering,* 36 (5), 368-376.

HEIDARZADEH, M., PIROOZ, M. D., ZAKER, N. H., YALCINER, A. C., MOKHTARI, M. & ESMAEILY, A. (2008) Historical tsunami in the Makran Subduction Zone off the southern coasts of Iran and Pakistan and results of numerical modeling. *Ocean Engineering,* 35 (8-9), 774-786.

HENRY, P., LALLEMANT, S., NAKAMURA, K., TSUNOGAI, U., MAZZOTTI, S. & KOBAYASHI, K. (2002) Surface expression of fluid venting at the toe of the Nankai wedge and implications for flow paths. *Marine Geology,* 187 (1-2), 119-143.

HENSTOCK, T. J., MCNEILL, L. C. & TAPPIN, D. R. (2006) Seafloor morphology of the Sumatran subduction zone: Surface rupture during megathrust earthquakes? *Geology* 34 (6), 485-488.

HEURET, A., CONRAD, C. P., FUNICIELLO, F., LALLEMAND, S. & SANDRI, L. (2012) Relation between subduction megathrust earthquakes, trench sediment thickness and upper plate strain. *Geophysical Research Letters,* 39 (5), L05304.

HU, Y. & WANG, K. L. (2008) Coseismic strengthening of the shallow portion of the subduction fault and its effects on wedge taper. *Journal of Geophysical Research-Solid Earth,* 113 (B12), 14, B12411.

HUTCHISON, I., LOUDEN, K. E., WHITE, R. S. & VONHERZEN, R. P. (1981) Heat-flow and age of the Gulf of Oman. *Earth and Planetary Science Letters,* 56 (DEC), 252-262.

HYNDMAN, R. D. & PEACOCK, S. M. (2003) Serpentinization of the forearc mantle. *Earth and Planetary Science Letters,* 212 (3-4), 417-432.

HYNDMAN, R. D. & WANG, K. (1993) Thermal constraints on the zone of major thrust earthquake failure - the Cascadia Subduction Zone. *Journal of Geophysical Research-Solid Earth,* 98 (B2), 2039-2060.

HYNDMAN, R. D., WANG, K. & YAMANO, M. (1995) Thermal constraints on the seismogenic portion of the southwestern Japan subduction thrust. *Journal of Geophysical Research-Solid Earth,* 100 (B8), 15373-15392.

HYNDMAN, R. D., YAMANO, M. & OLESKEVICH, D. A. (1997) The seismogenic zone of subduction thrust faults. *Island Arc,* 6 (3), 244-260.

IDE, S., BALTAY, A. & BEROZA, G. C. (2011) Shallow Dynamic Overshoot and Energetic Deep Rupture in the 2011 M(w) 9.0 Tohoku-Oki Earthquake. *Science,* 332 (6036), 1426-1429.

IKARI, M. J. & SAFFER, D. M. (2011) Comparison of frictional strength and velocity dependence between fault zones in the Nankai accretionary complex. *Geochemistry Geophysics Geosystems,* 12, Q0AD11.

JACOB, K. H. & QUITTMEYER, R. C. (1979) The Makran Region of Pakistan and Iran: Trench-Arc System with Active Plate Subduction. *Geodynamics of Pakistan,* 305-317.

JACOBY, G. C., BUNKER, D. E. & BENSON, B. E. (1997) Tree-ring evidence for an AD 1700 Cascadia earthquake in Washington and northern Oregon. *Geology,* 25 (11), 999-1002.

JOHNSON, J. E., GOLDFINGER, C. & SUESS, E. (2003) Geophysical constraints on the surface distribution of authigenic carbonates across the Hydrate Ridge region, Cascadia margin. *Marine Geology,* 202 (1-2), 79-120.

KARATO, S.-I. & WU, P. (1993) Rheology of the Upper Mantle: A Synthesis. *Science,* 260 (5109), 771-778.

KAUL, N., ROSENBERGER, A. & VILLINGER, H. (2000) Comparison of measured and BSR-derived heat flow values, Makran accretionary prism, Pakistan. *Marine Geology,* 164 (1-2), 37-51.

KINOSHITA, M., MOORE, G. F. & KIDO, Y. N. (2011) Heat flow estimated from BSR and IODP borehole data: Implication of recent uplift and erosion of the imbricate thrust zone in the Nankai Trough off Kumano. *Geochemistry Geophysics Geosystems,* 12, 18, Q0AD18.

KLAUCKE, I., WEINREBE, W., LINKE, P., KLSCÄHEN, D. & BIALAS, J. (2012) Sidescan sonar imagery of widespread fossil and active cold seeps along the central Chilean continental margin. *Geo-Marine Letters,* 32 (5-6), 489-499.

KLINGELHOEFER, F., GUTSCHER, M. A., LADAGE, S., DESSA, J. X., GRAINDORGE, D., FRANKE, D., ANDRE, C., PERMANA, H., YUDISTIRA, T. & CHAUHAN, A. (2010) Limits of the seismogenic zone in the epicentral region of the 26 December 2004 great Sumatra-Andaman earthquake: Results from seismic refraction and wide-angle reflection surveys and thermal modeling. *Journal of Geophysical Research-Solid Earth,* 115, 23, B01304.

KOPP, C., FRUEHN, J., FLUEH, E. R., REICHERT, C., KUKOWSKI, N., BIALAS, J. & KLAESCHEN, D. (2000) Structure of the Makran subduction zone from wide-angle and reflection seismic data. *Tectonophysics,* 329 (1-4), 171-191.

KOPP, H. & KUKOWSKI, N. (2003) Backstop geometry and accretionary mechanics of the Sunda margin. *Tectonics,* 22 (6), 16.

KOYI, H. A., HESSAMI, K. & TEIXELL, A. (2000) Epicenter distribution and magnitude of earthquakes in fold thrust belts: Insights from Sandbox Models. *Geophysical Research Letters,* 27 (2), 273-276.

KUKOWSKI, N., SCHILLHORN, T., FLUEH, E. R. & HUHN, K. (2000) Newly identified strike-slip plate boundary in the northeastern Arabian Sea. *Geology,* 28 (4), 355-358.

KUKOWSKI, N., SCHILLHORN, T., HUHN, K., VON RAD, U., HUSEN, S. & FLUEH, E. R. (2001) Morphotectonics and mechanics of the central Makran accretionary wedge off Pakistan. *Marine Geology,* 173 (1-4), 1-19.

LALLEMAND, S. E., SCHNURLE, P. & MALAVIEILLE, J. (1994) Coulomb theory applied to accretionary and nonaccretionary wedges - possible causes for tectonic erosion and or frontal accretion. *Journal of Geophysical Research-Solid Earth,* 99 (B6), 12033-12055.

LE PICHON, X., HENRY, P. & LALLEMANT, S. (1993) Accretion and erosion in subduction zones - the role of fluids. *Annual Review of Earth and Planetary Sciences,* 21, 307-331.

LEGGETT, J. K. & PLATT, J. P. (1984) Structural Features of the Makran Fore-arc on Landsat Imagery. *In: Haq, B.U., Milliman, J.D. (Eds.), Marine Geology and Oceanography of Arabian Sea and Coastal Pakistan. Van Nostrand Reinhold, New York,* 33–43.

LOHRMANN, J., KUKOWSKI, N., ADAM, J. R. & ONCKEN, O. (2003) The impact of analogue material properties on the geometry, kinematics, and dynamics of convergent sand wedges. *Journal of Structural Geology,* 25 (10), 1691-1711.

MACKAY, M. E. (1995) Structural variation and landward vergence at the toe of the Oregon accretionary prism. *Tectonics,* 14 (6), 1309-1320.

MCADOO, B. G., CAPONE, M. K. & MINDER, J. (2004) Seafloor geomorphology of convergent margins: Implications for Cascadia seismic hazard. *Tectonics,* 23 (6), 15.

MINSHULL, T. & WHITE, R. (1989) Sediment compaction and fluid migration in the Makran accretionary prism. *Journal of Geophysical Research-Solid Earth and Planets,* 94 (B6), 7387-7402.

MOORE, G. F., SAFFER, D., STUDER, M. & COSTA PISANI, P. (2011) Structural restoration of thrusts at the toe of the Nankai Trough accretionary prism off Shikoku Island, Japan: Implications for dewatering processes. *Geochemistry Geophysics Geosystems,* 12 Q0AD12.

MOORE, G. F., SHIPLEY, T. H., STOFFA, P. L., KARIG, D. E., TAIRA, A., KURAMOTO, S., TOKUYAMA, H. & SUYEHIRO, K. (1990a) Structure of the Nankai trough accretionary zone from multichannel seismic-reflection data. *Journal of Geophysical Research-Solid Earth and Planets,* 95 (B6), 8753-8765.

MOORE, G. F., TAIRA, A., KLAUS, A., BECKER, L., BOECKEL, B., CRAGG, B. A., DEAN, A., FERGUSSON, C. L., HENRY, P., HIRANO, S., HISAMITSU, T., HUNZE, S., KASTNER, M., MALTMAN, A. J., MORGAN, J. K., MURAKAMI, Y., SAFFER, D. M., SANCHEZ-GOMEZ, M., SCREATON, E. J., SMITH, D. C., SPIVACK, A. J., STEURER, J., TOBIN, H. J., UJIIE, K., UNDERWOOD, M. B. & WILSON, M. (2001) New insights into deformation and fluid flow processes in the Nankai Trough accretionary prism: Results of Ocean Drilling Program Leg 190. *Geochemistry Geophysics Geosystems,* 2, 22, GC000166.

MOORE, J. C. (1989) Tectonics and hydrogeology of accretionary prisms - role of the decollement zone. *Journal of Structural Geology,* 11 (1-2), 95-106.

MOORE, J. C., BROWN, K. M., HORATH, F., COCHRANE, G., MACKAY, M. & MOORE, G. (1991) Plumbing Accretionary Prisms: Effects of Permeability Variations. *Philosophical Transactions: Physical Sciences and Engineering,* 335 (1638), 275-288.

MOORE, J. C., MOORE, G. F., COCHRANE, G. R. & TOBIN, H. J. (1995) Negative-polarity seismic reflectors along faults of the Oregon Accretionary Prism - Indicators of overpressuring *Journal of Geophysical Research-Solid Earth,* 100 (B7), 12895-12906.

MOORE, J. C., ORANGE, D. & KULM, L. D. (1990b) Interrelationship of fluid venting and structural evolution: Alvin observations from the frontal accretionary prism, Oregon. *Journal of Geophysical Research: Solid Earth,* 95 (B6), 8795-8808.

MOORE, J. C. & SAFFER, D. (2001) Updip limit of the seismogenic zone beneath the accretionary prism of southwest Japan: An effect of diagenetic to low-grade metamorphic processes and increasing effective stress. *Geology,* 29 (2), 183-186.

MOORE, J. C. & VROLIJK, P. (1992) Fluids in accretionary prisms. *Reviews of Geophysics,* 30 (2), 113-135.

MORLEY, C. K. (2007) Interaction between critical wedge geometry and sediment supply in a deep-water fold belt. *Geology,* 35 (2), 139-142.

MOUCHOT, N., LONCKE, L., MAHIEUX, G., BOURGET, J., LALLEMANT, S., ELLOUZ-ZIMMERMANN, N. & LETURMY, P. (2010) Recent sedimentary processes along the Makran trench (Makran active margin, off Pakistan). *Marine Geology,* 271 (1-2), 17-31.

MOUNTAIN, G. S. & PRELL, W. L. (1990) A multiphase plate tectonic history of the southeast continental margin of Oman. *Geology and Tectonics of the Oman Region,* 49, 725-743.

NETZEBAND, G. L., KRABBENHOEFT, A., ZILLMER, M., PETERSEN, C. J., PAPENBERG, C. & BIALAS, J. (2010) The structures beneath submarine methane seeps: Seismic evidence from Opouawe Bank, Hikurangi Margin, New Zealand. *Marine Geology,* 272, 59-70.

OKAL, E. A. & SYNOLAKIS, C. E. (2008) Far-field tsunami hazard from mega-thrust earthquakes in the Indian Ocean. *Geophysical Journal International,* 172 (3), 995-1015.

OLESKEVICH, D. A., HYNDMAN, R. D. & WANG, K. (1999) The updip and downdip limits to great subduction earthquakes: Thermal and structural models of Cascadia, south Alaska, SW Japan, and Chile. *Journal of Geophysical Research-Solid Earth,* 104 (B7), 14965-14991.

OLU, K., SIBUET, M., HARMEGNIES, F., FOUCHER, J. P. & FIALA-MÉDIONI, A. (1996) Spatial distribution of diverse cold seep communities living on various diapiric structures of the southern Barbados prism. *Progress in Oceanography,* 38 (4), 347-376.

PARK, J. O., TSURU, T., KODAIRA, S., CUMMINS, P. R. & KANEDA, Y. (2002a) Splay fault branching along the Nankai subduction zone. *Science,* 297 (5584), 1157-1160.

PARK, J. O., TSURU, T., TAKAHASHI, N., HORI, T., KODAIRA, S., NAKANISHI, A., MIURA, S. & KANEDA, Y. (2002b) A deep strong reflector in the Nankai accretionary wedge from multichannel seismic data: Implications for underplating and interseismic shear stress release. *Journal of Geophysical Research-Solid Earth,* 107 (B4), 18.

PEACOCK, S. M. (1990) Fluid processes in subduction zones. *Science,* 248 (4953), 329-337.

PEACOCK, S. M. & HYNDMAN, R. D. (1999) Hydrous minerals in the mantle wedge and the maximum depth of subduction thrust earthquakes. *Geophysical Research Letters,* 26 (16), 2517-2520.

PEACOCK, S. M. & WANG, K. (1999) Seismic Consequences of Warm Versus Cool Subduction Metamorphism: Examples from Southwest and Northeast Japan. *Science,* 286 (5441), 937-939.

PECHER, I. A., HENRYS, S. A., WOOD, W. T., KUKOWSKI, N., CRUTCHLEY, G. J., FOHRMANN, M., KILNER, J., SENGER, K., GORMAN, A. R., COFFIN, R. B., GREINERT, J. & FAURE, K. (2010) Focussed fluid flow on the Hikurangi Margin, New Zealand - Evidence from possible local upwarping of the base of gas hydrate stability. *Marine Geology,* 272, 99-113.

PLATT, J. P., LEGGETT, J. K. & ALAM, S. (1988) Slip vectors and fault mechanics in the Makran accretionary wedge, southwest Pakistan. *Journal of Geophysical Research-Solid Earth and Planets,* 93 (B7), 7955-7973.

PLATT, J. P., LEGGETT, J. K., YOUNG, J., RAZA, H. & ALAM, S. (1985) Large-scale sediment underplating in the Makran accretionary prism, southwest Pakistan. *Geology,* 13 (7), 507-511.

RANI, V. S., SRIVASTAVA, K., SRINAGESH, D. & DIMRI, V. P. (2011) Spatial and Temporal Variations of b-Value and Fractal Analysis for the Makran Region. *Marine Geodesy,* 34 (1), 77-82.

RIEDEL, M., NOVOSEL, I., SPENCE, G. D., HYNDMAN, R. D., CHAPMAN, R. N., SOLEM, R. C. & LEWIS, T. (2006) Geophysical and geochemical signatures associated with gas hydrate-related venting in the northern Cascadia margin. *Geological Society of America Bulletin,* 118 (1-2), 23-38.

RÖMER, M., SAHLING, H., PAPE, T., BOHRMANN, G. & SPIEß, V. (2012) Quantification of gas bubble emissions from submarine hydrocarbon seeps at the Makran continental margin (offshore Pakistan). *Journal of Geophysical Research: Oceans,* 117 (C10).

SAFFER, D. M. & BEKINS, B. A. (2006) An evaluation of factors influencing pore pressure in accretionary complexes: Implications for taper angle and wedge mechanics. *Journal of Geophysical Research-Solid Earth,* 111 (B4), 21, B04101.

SAFFER, D. M., LOCKNER, D. A. & MCKIERNAN, A. (2012) Effects of smectite to illite transformation on the frictional strength and sliding stability of intact marine mudstones. *Geophysical Research Letters,* 39 (11), L11304.

SAFFER, D. M. & SCREATON, E. J. (2003) Fluid flow at the toe of convergent margins: interpretation of sharp pore-water geochemical gradients. *Earth and Planetary Science Letters,* 213 (3-4), 261-270.

SAFFER, D. M. & TOBIN, H. J. (2011) Hydrogeology and Mechanics of Subduction Zone Forearcs: Fluid Flow and Pore Pressure. *Annual Review of Earth and Planetary Sciences,* 39 (1), 157-186.

SAFFER, D. M., UNDERWOOD, M. B. & MCKIERNAN, A. W. (2008) Evaluation of factors controlling smectite transformation and fluid production in subduction zones: Application to the Nankai Trough. *Island Arc,* 17 (2), 208-230.

SAIN, K., MINSHULL, T. A., SINGH, S. C. & HOBBS, R. W. (2000) Evidence for a thick free gas layer beneath the bottom simulating reflector in the Makran accretionary prism. *Marine Geology,* 164 (1-2), 3-12.

SCHLUTER, H. U., PREXL, A., GAEDICKE, C., ROESER, H., REICHERT, C., MEYER, H. & VON DANIELS, C. (2002) The Makran accretionary wedge: sediment thicknesses and ages and the origin of mud volcanoes. *Marine Geology,* 185 (3-4), 219-232.

SHAW, B. & JACKSON, J. (2010) Earthquake mechanisms and active tectonics of the Hellenic subduction zone. *Geophysical Journal International,* 181 (2), 966-984.

SMITH, G., MCNEILL, L., HENSTOCK, T. J. & BULL, J. (2012) The structure and fault activity of the Makran accretionary prism. *Journal of Geophysical Research,* 117 (B7), B07407.

SMITH, G. L., MCNEILL, L. C., WANG, K., HE, J. & HENSTOCK, T. J. (2013) Thermal structure and megathrust seismogenic potential of the Makran subduction zone. *Geophysical Research Letters,* 40.

SMITH, W. H. F. & SANDWELL, D. T. (1997) Global sea floor topography from satellite altimetry and ship depth soundings. *Science,* 277 (5334), 1956-1962.

SPIESS, V., BAUMANN, L., BRUNING, M., COLLINS, G. (2007) Cold Seeps of the Makran Subduction Zone (Continental Margin of Pakistan). *Meteor-Berichte 10-3. Cruise No. 74, Leg 2. Cruise Report*.

STEIN, C. A. & STEIN, S. (1992) A model for the global variation in oceanic depth and heat flow with lithospheric age. *Nature,* 359 (6391), 123-129.

STORTI, F. & MCCLAY, K. (1995) Influence of syntectonic sedimentation on thrust wedges in analog models. *Geology,* 23 (11), 999-1002.

STRASSER, M., MOORE, G. F., KIMURA, G., KOPF, A. J., UNDERWOOD, M. B., GUO, J. & SCREATON, E. J. (2011) Slumping and mass transport deposition in the Nankai fore arc: Evidence from IODP drilling and 3-D reflection seismic data. *Geochemistry Geophysics Geosystems,* 12, Q0AD13.

SUPPE, J. (2007) Absolute fault and crustal strength from wedge tapers. *Geology,* 35 (12), 1127-1130.

TIRRUL, R., BELL, I. R., GRIFFIS, R. J. & CAMP, V. E. (1983) The Sistan Suture Zone of Eastern Iran. *Geological Society of America Bulletin,* 94 (1), 134-150.

TOBIN, H. J. & SAFFER, D. M. (2009) Elevated fluid pressure and extreme mechanical weakness of a plate boundary thrust, Nankai Trough subduction zone. *Geology,* 37 (8), 679-682.

TORRES, M. E., WALLMANN, K., TRÉHU, A. M., BOHRMANN, G., BOROWSKI, W. S. & TOMARU, H. (2004) Gas hydrate growth, methane transport, and chloride enrichment at the southern summit of Hydrate Ridge, Cascadia margin off Oregon. *Earth and Planetary Science Letters,* 226 (1-2), 225-241.

TRÉHU, A. M., FLEMINGS, P. B., BANGS, N. L., CHEVALLIER, J., GRACIA, E., JOHNSON, J. E., LIU, C. S., LIU, X. L., RIEDEL, M. & TORRES, M. E. (2004) Feeding methane vents and gas hydrate deposits at south Hydrate Ridge. *Geophysical Research Letters,* 31 (23), 4, L23310.

VAN KEKEN, P. E., CURRIE, C., KING, S. D., BEHN, M. D., CAGNIONCLE, A., HE, J., KATZ, R. F., LIN, S.-C., PARMENTIER, E. M., SPIEGELMAN, M. & WANG, K. (2008) A community benchmark for subduction zone modeling. *Physics of the Earth and Planetary Interiors,* 171, 187-197.

VAN KEKEN, P. E., KIEFER, B. & PEACOCK, S. M. (2002) High-resolution models of subduction zones: Implications for mineral dehydration reactions and the transport of water into the deep mantle. *Geochemistry, Geophysics, Geosystems,* 3 (10), 1056.

VON HUENE, R. & SCHOLL, D. W. (1991) Observations at convergent margins concerning sediment subduction, subduction erosion, and the growth of continental-crust. *Reviews of Geophysics,* 29 (3), 279-316.

VON RAD, U., BERNER, U., DELISLE, G., DOOSE-ROLINSKI, H., FECHNER, N., LINKE, P., LUCKGE, A., ROESER, H. A., SCHMALJOHANN, R., WIEDICKE, M. & PARTIES, S. S. (2000) Gas and fluid venting at the Makran accretionary wedge off Pakistan. *Geo-Marine Letters,* 20 (1), 10-19.

VON RAD, U., RÖSCH, H., BERNER, U., GEYH, M., MARCHIG, V. & SCHULZ, H. (1996) Authigenic carbonates derived from oxidized methane vented from the Makran accretionary prism off Pakistan. *Marine Geology,* 136 (1-2), 55-77.

WADA, I. (2003) Thermal Structure and Geodynamics of Subduction Zones. *PhD Thesis, University of Victoria, School of Earth and Ocean Sciences*.

WADA, I. & WANG, K. (2009) Common depth of slab-mantle decoupling: Reconciling diversity and uniformity of subduction zones. *Geochemistry Geophysics Geosystems,* 10 (10), Q10009.

WADA, I., WANG, K., HE, J. & HYNDMAN, R. D. (2008) Weakening of the subduction interface and its effects on surface heat flow, slab dehydration, and mantle wedge serpentinization. *Journal of Geophysical Research: Solid Earth,* 113 (B4), B04402.

WALLACE, L. M., REYNERS, M., COCHRAN, U., BANNISTER, S., BARNES, P. M., BERRYMAN, K., DOWNES, G., EBERHART-PHILLIPS, D., FAGERENG, A., ELLIS, S., NICOL, A.,

MCCAFFREY, R., BEAVAN, R. J., HENRYS, S., SUTHERLAND, R., BARKER, D. H. N., LITCHFIELD, N., TOWNEND, J., ROBINSON, R., BELL, R., WILSON, K. & POWER, W. (2009) Characterizing the seismogenic zone of a major plate boundary subduction thrust: Hikurangi Margin, New Zealand. *Geochemistry Geophysics Geosystems,* 10 32.

WANG, K. & BILEK, S. L. (2011) Do subducting seamounts generate or stop large earthquakes? *Geology,* 39 (9), 819-822.

WANG, K. & DAVIS, E. E. (1992) Thermal effects of marine sedimentation in hydrothermally active areas. *Geophysical Journal International,* 110 (1), 70-78.

WANG, K., MULDER, T., ROGERS, G. C. & HYNDMAN, R. D. (1995) Case for very low coupling stress on the Cascadia subduction fault. *Journal of Geophysical Research,* 100 (B7), 12907-12918.

WANG, K. L. & HU, Y. (2006) Accretionary prisms in subduction earthquake cycles: The theory of dynamic Coulomb wedge. *Journal of Geophysical Research-Solid Earth,* 111 (B6), 16, B06410.

WHITE, R. S. (1979) Deformation of the Makran Continental Margin. *Geodynamics of Pakistan,* 295-304.

WHITE, R. S. (1982a) Deformation of the Makran accretionary sediment prism in the Gulf of Oman (north-west Indian Ocean). *Geological Society of London, Special Publication,* 10, 357-372.

WHITE, R. S. (1983) The Little Murray Ridge. *in Bally, A.W., ed., Seismic expression of structural styles. American Association of Petroleum Geologists Studies in Geology,* 15, 10 - 23.

WHITE, R. S., LOUDON, K.E. (1982b) The Makran Continental Margin: Structure of a Thickly Sedimented Convergent Plate Boundary. *Studies in Continental Margin Geology,* AAPG Memoir No. 34, 499-518.

WHITE, R. S. & ROSS, D. A. (1979) Tectonics of the Western Gulf of Oman. *J. Geophys. Res.,* 84 (B7), 3479-3489.

WHITMARSH, R. B. (1979) Owen Basin off the southeast margin of Arabia and the evolution of the Owen Fracture Zone. *Geophysical Journal of the Royal Astronomical Society,* 58 (2), 441-470.

WIEDICKE, M., NEBEN, S. & SPIESS, V. (2001) Mud volcanoes at the front of the Makran accretionary complex, Pakistan. *Marine Geology,* 172 (1-2), 57-73.

WILLETT, S., BEAUMONT, C. & FULLSACK, P. (1993) Mechanical model for the tectonics of doubly vergent compressional orogens. *Geology,* 21 (4), 371-374.

ZHAO, Z. Y., MOORE, G. F., BANGS, N. L. B. & SHIPLEY, T. H. (2000) Spatial variations of the decollement/protodecollement zone and their implications: A 3-D seismic inversion study of the northern Barbados accretionary prism. *Island Arc,* 9 (2), 219-236.

ZÜHLSDORFF, L. & SPIESS, V. (2004) Three-dimensional seismic characterization of a venting site reveals compelling indications of natural hydraulic fracturing. *Geology,* 32 (2), 101-104.

ZÜHLSDORFF, L., SPIEß, V., HÜBSCHER, C., VILLINGER, H. & ROSENBERGER, A. (2000) Implications for focused fluid transport at the northern Cascadia accretionary prism from a correlation between BSR occurrence and near-sea-floor reflectivity anomalies imaged in a multi-frequency seismic data set. *International Journal of Earth Sciences,* 88 (4), 655-667.

Appendix 1. Thermal modelling methodology and sensitivity test results

Modelling outline

The thermal model used in Chapter 3 of this thesis is the PGCTherm code developed by Dr. Jiangheng He of the Pacific Geoscience Centre, Canada. PGCTherm is a steady state 2D finite element model which has been previously tested and used in several studies (e.g. Gutscher and Peacock, 2003, Currie et al., 2004, Wada and Wang, 2009). This method was shown to agree well with other finite element models in a community benchmarking exercise (van Keken et al., 2008).

There are three main components to the model:

- A subducting slab with assigned convergence velocity
- A non-deforming upper plate and rigid upper mantle of 30-35 km thickness
- A viscous mantle wedge

The subducting slab is given a uniform thickness of 95 km, with an assumed mantle temperature at its base of 1450°C (Peacock and Wang, 1999), but the thermally relevant thickness is defined by the oceanic geotherm which forms the seaward boundary of the model (Wada et al., 2008). Uncertainties in the lower boundary temperature have little effect on the temperatures generated for the plate boundary due to the efficient advective heat transfer from the oceanic geotherm to the subducting slab (Currie et al., 2004). Heat flow is treated as conductive within the subducting and upper plates.

The viscous mantle wedge accounts for advective heat transport and solid-state viscous flow in the wedge. The upper boundary of the wedge is coupled to the upper plate and the lower boundary moves at the subduction velocity (Currie et al., 2004). The effects of adiabatic heating due to mantle flow have been shown to be negligible and so this is neglected in this model (Currie et al., 2004). Volume changes due to

metamorphic phase changes are not included, nor are the effects of magma migration. Compositional and thermal buoyancy in the wedge is also ignored.

The wedge flow field is approximated using the coupled thermal and viscous flow numerical method of Wada et al (2008) with a prescribed mantle maximum depth of slab-mantle decoupling of 75 km (Wada and Wang, 2009). This method invokes a dislocation-creep rheology and uses the customary uniaxial-deformation expression:

$\dot{\varepsilon}_a = A(\sigma_a/\mu)^n \exp(-E/RT)$ (1)

$\dot{\varepsilon}_a$ = *Axial strain rate*
A = *Constant* ($2 \times 10^{18}\ s^{-1}$)
σ_a = *Stress*
μ = *Shear Modulus (80 GPa)*
n = *Constant (3)*
E = *Activation Energy (430kJ/mol)*
R = *Universal Gas Constant* ($8.3145\ J\ mol^{-1}\ K^{-1}$)
T = *Absolute Temperature*

Constants are for a wet olivine rheology (Karato and Wu, 1993)

Equation (1) is cast into the relationship between deviatoric stress ($\dot{\varepsilon}_{ij}$) and deviatoric strain rate (σ_{ij}) (2)

$\sigma_{ij} = 2\eta_e \dot{\varepsilon}_{ij}$ (2)

where η_e is the effective viscosity as expressed in (3),

$\eta_e = 3\text{-}(n+1/2)\ \mu/A\ (\mu/\sigma)^{n-1} \exp(E/RT)$ (3)

where σ is the second invariant of σ_{ij} (Wada et al., 2008)

Methodology

The finite element mesh contains of isoparametric, quadrilateral elements of variable sizes (few cm to 10 km) (Figure A1), and is primarily kinematic, whilst also incorporating mantle wedge flow. The mesh size is user defined and is finest along the plate boundary and in the mantle wedge corner.

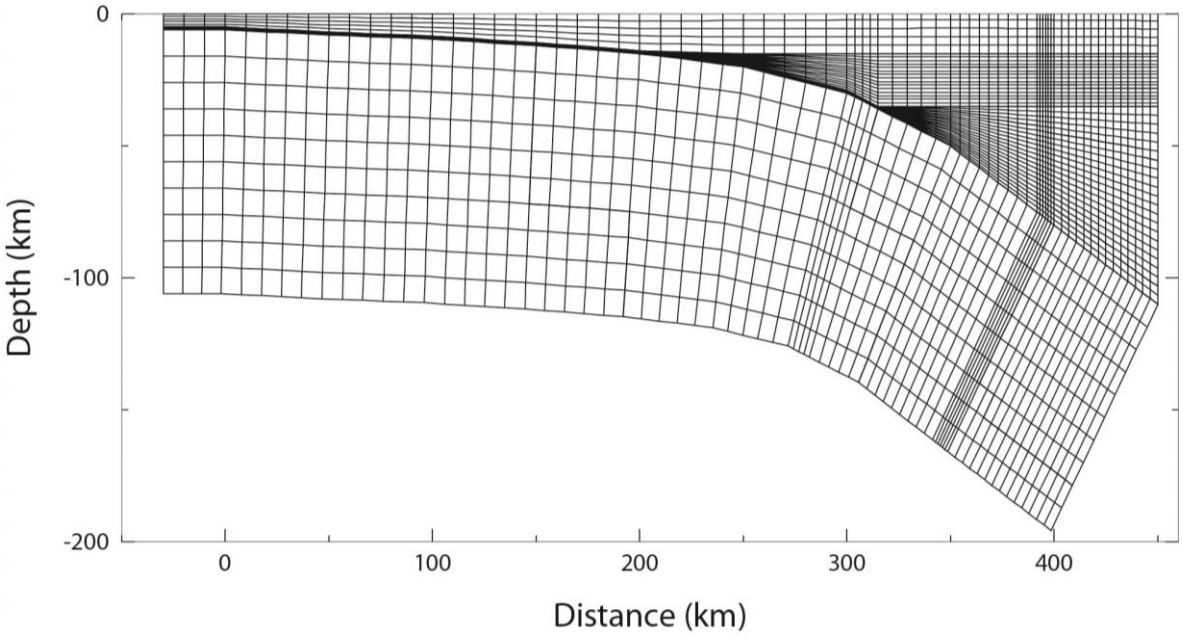

Figure A1. *The finite element mesh, showing change in element size across the grid. Smallest elements are located along the plate boundary and in the mantle wedge. Mantle wedge flow is incorporated through the equations for mass and momentum conservation for an incompressible Boussinesq fluid (1) & (2).*

The model runs by numerically solving equations (4) and (5) for the mantle wedge, and then solving the steady state heat advection-diffusion equation (6) for the entire grid, using a finite element approach which allows for accurate discretization of the grid (van Keken et al., 2002). Nine-node isoparametric elements are used for temperature and velocity, and four-node compatible elements for pressure (Currie et al., 2004).

$\nabla \cdot v = 0$ (4) Equation for mass conservation

$\nabla \cdot (2\eta\dot{\varepsilon}) - \nabla P = 0$ (5) Equation for momentum conservation

v = Flow velocity

P = Dynamic pressure (non hydrostatic pressure generated by flow)

η = Viscosity

$\dot{\varepsilon}$ = Strain rate tensor

The steady state heat advection-diffusion equation, allowing for thermal conductivity, radiogenic heat production and frictional heating is expressed below:

$\rho c_p (v \cdot \nabla) T = \nabla \cdot (k \nabla T) + Q + Q_{sh}$ (6)

ρ = Density

c_p = Heat capacity

T = Temperature

k = Thermal conductivity

Q = Internal heating rate caused by radiogenic elements

Q_{sh} = Shear heating rate along the plate interface

The Stokes and heat equations (4-6) are solved simultaneously. A conventional penalty function formulation is used to stabilize the pressure solutions, and the Galerkin least squares method is used to alleviate uncertainties in advection-dominated temperature solutions (Currie et al., 2004). Linear Taylor-Hood triangles are utilised for equations (4) and (5), and for (6) after discretisation using streamline upwinding (van Keken et al., 2002). Velocity and pressure are found through conjugate gradient iteration (BiCCSTAB) after ILU preconditioning (van Keken et al., 2002). Equation (5) becomes nonlinear and nonlinearly coupled with Equation (6) when a stress and temperature dependant rheology is used, therefore a multicorrector fixed-point iteration algorithm is used to solve this (Currie et al., 2004). An inner iteration in which velocity and viscosity are updated is used for Equation (5), and then a global iteration is undertaken on equations (4)-(6) (Wada, 2003). The iteration is considered converged when the maximum relative difference

between successive iterations of the velocity and temperature solutions is less than 10^{-6} (van Keken et al., 2002). This tends to occur after 18-20 iterations for models with a non-linear rheology (Currie et al., 2004).

Frictional heating in the shallow part of the plate boundary is derived from fault slip rate and the shear stress (7), (8) & (9) (Wada, 2003).

Shear stress on a fault at failure is derived as:

$$\tau = \mu (1-\lambda) \sigma_n = \mu' \sigma_n \qquad (7)$$

τ = Shear stress
μ = Coefficient of friction on the fault
μ' = Effective coefficient of friction
σ_n = Normal stress
λ = Fluid pressure ratio

$$\lambda = P_f / P_l \qquad (8)$$

P_f *= Fluid pressure*
P_l *= Lithostatic pressure*

Frictional heating is then derived as:

$$Q_{fh} = \tau v = \mu' \sigma_n v \qquad (9)$$

Q_{fh} = Frictional heating
τ = Shear stress
v = Downdip velocity
σ_n = Normal stress
μ' = Effective coefficient of friction

μ' is taken as 0.03 in our final model, consistent with previous applications of this model. The weight of the overriding rock column is used to approximate σ_n.

Viscous heating along the deeper plate boundary (where the subducting slab is in contact with the mantle wedge) is calculated from the product of shear stress and shear strain rate (Wada et al., 2008). This transition is shown in Figure A2.

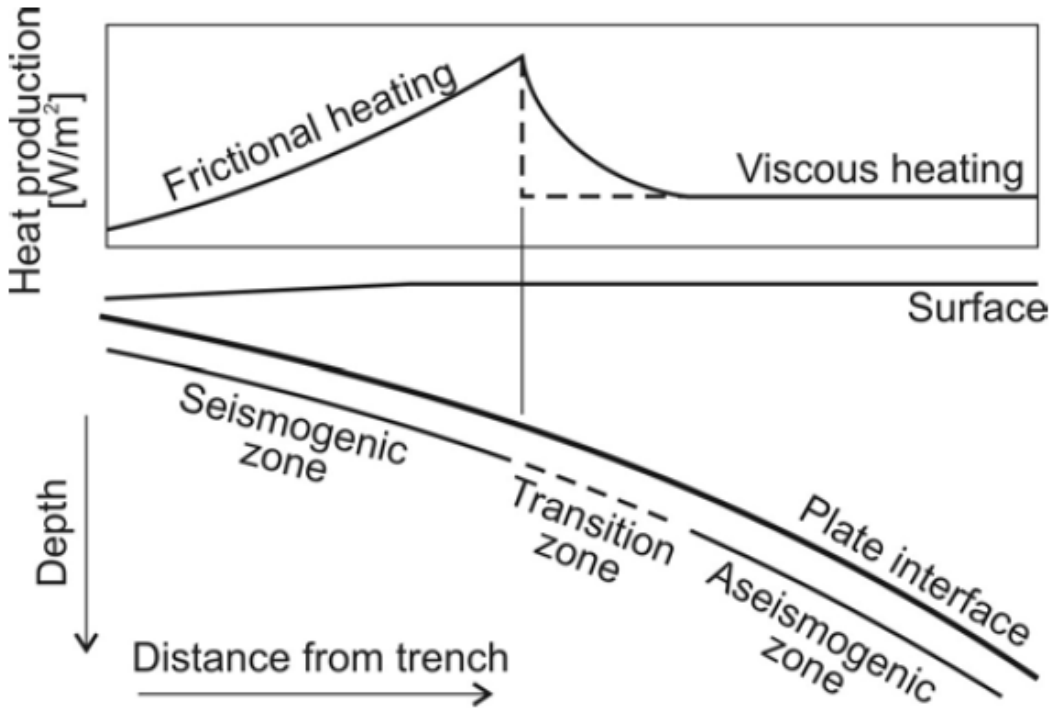

Figure A2. *Schematic of the downdip transition from frictional heating to viscous heating. In this example the transition occurs concurrent with the downdip seismogenic limit. From (Wada and Wang, 2009).*

Boundary conditions

Upper boundary = 0°C (Peacock and Wang, 1999). A smoothed profile of bathymetry and topography

Lower boundary = 1450°C (Peacock and Wang, 1999) at the base of the 95 km thick subducting slab

Seaward boundary = Oceanic geotherm calculated in the SEDTEM program. This accounts for plate age and sedimentation rate (producing a known sediment thickness), and produces a result which matches observed surface heat flow. SEDTEM is a1D finite element code which simulates the cooling of an isothermal half-space with an initial temperature of 1450 °C, with sedimentation on top (Stein and Stein, 1992, Wang and Davis, 1992).

Landward boundary = One-dimensional, steady state, conductive heat equation generates a geotherm for upper plate producing a surface heat flow of 80 mW/m^2. Beneath this depth (in the mantle wedge) inflow and outflow are permitted at the landward edge of the model due to the presence of the circulating mantle wedge and an adiabatic thermal gradient of 0.3°C/km is applied. The depth at which the transition between inflow and outflow occurs is iteratively determined by the model and is controlled by wedge rheology and subducting plate geometry (Currie et al., 2004). No horizontal conductive heat flow is allowed in the flow direction of the mantle wedge portion of the landward boundary ($\nabla T \cdot \nu = 0$) (Wada, 2003), and a boundary condition which requires no velocity gradient across the boundary is applied (Currie et al., 2004). Previous studies have found that changes in the assumed backarc surface heat flow (down to 50 mW/m^2) have little effect on the thermal profile of the slab because heat supply from the backarc to the forarc is controlled by the deeper, flowing portion (the mantle wedge).

Inputs

Three user defined files are input the model: The oceanic geotherm (generated from SEDTEM, the continental geotherm, and an input file containing the material properties, plate geometry and convergence rate. The material properties input are as described in Chapter 3.

Sensitivity test results

Plate Age

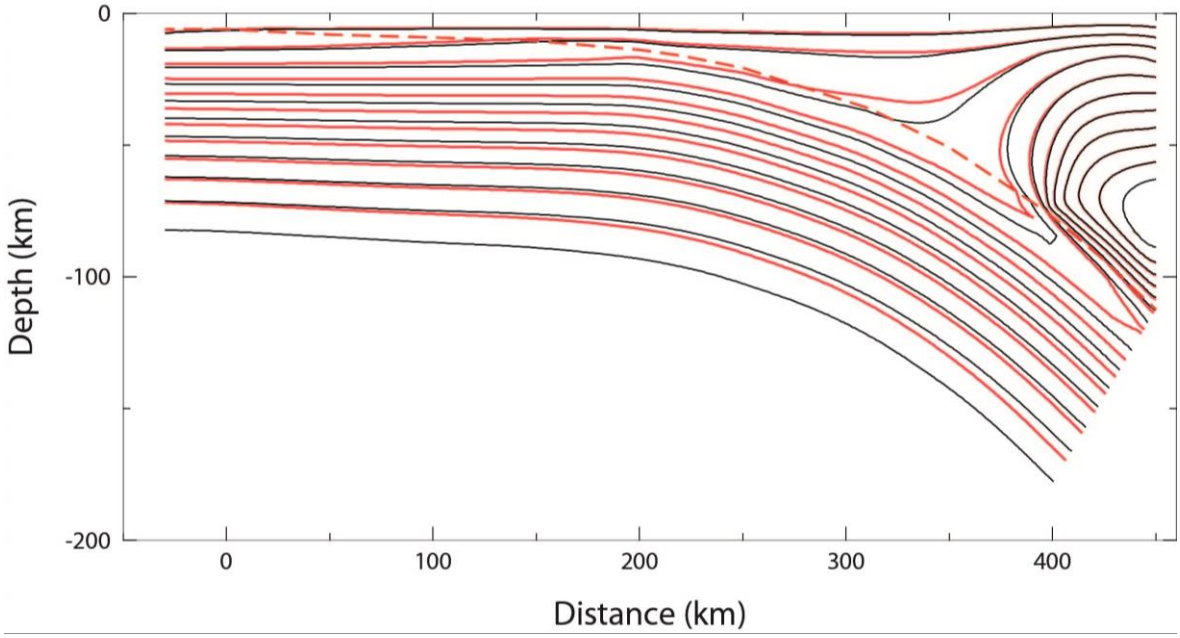

Figure A3. *Plate age. 85Ma in black, 50 Ma in red. Contour interval 100°C.*

Thermal Conductivity

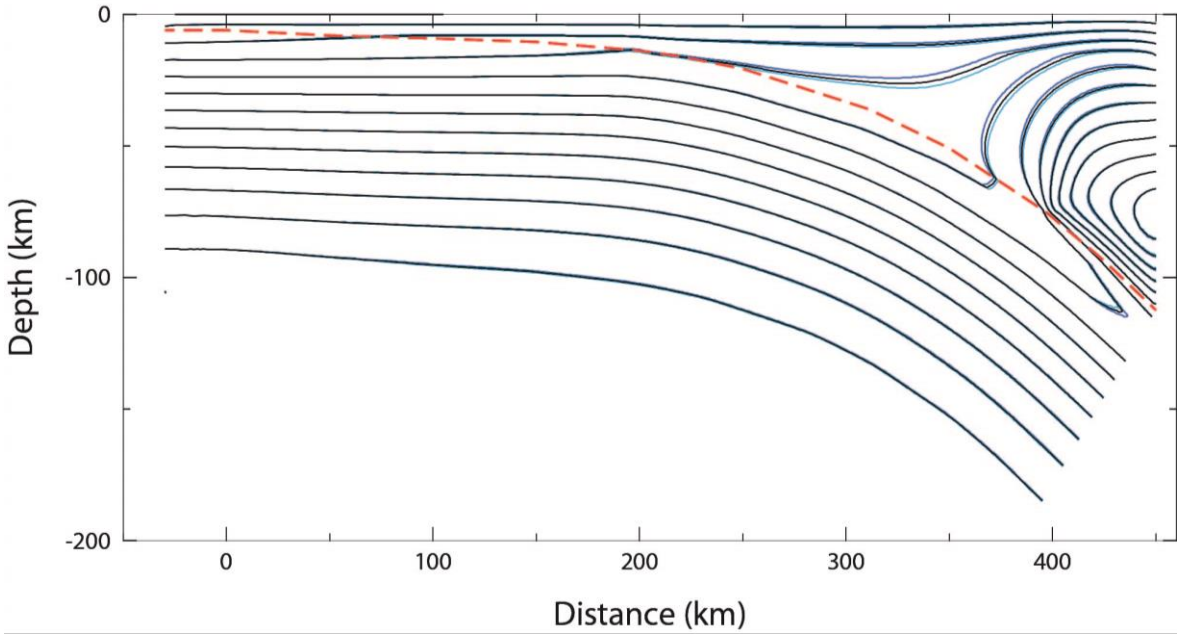

Figure A4. *Thermal conductivity. Light blue = Thermal conductivity +0.2 $Wm^{-1}K^{-1}$. Dark Blue + Thermal conductivity -0.2 $Wm^{-1}K^{-1}$. Contour interval 100°C.*

Heat Productivity

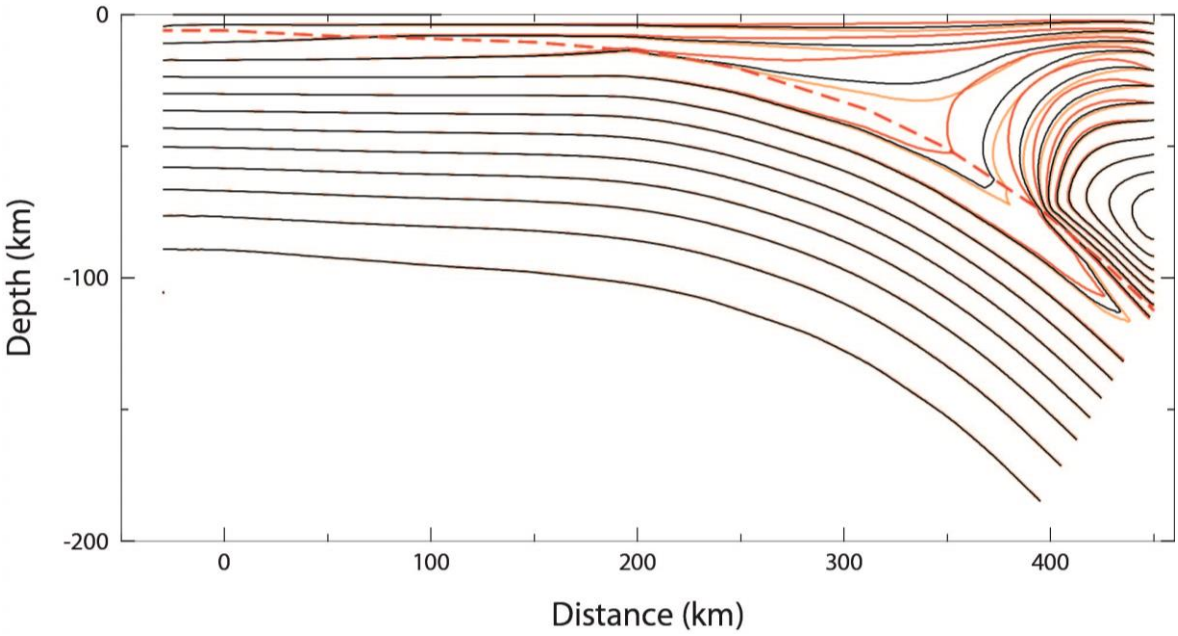

Figure A5. *Heat Productivity. Red= Heat Productivity x 2, Orange= Heat Productivity/2. Contour interval 100°C.*

Frictional Heating

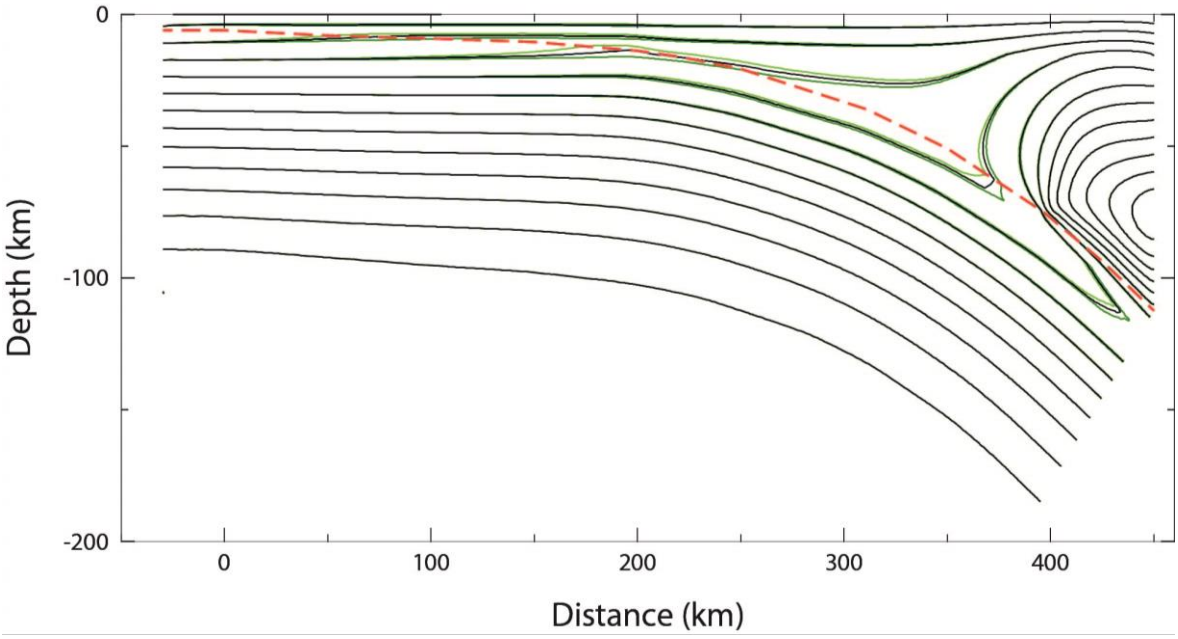

Figure A6. *Frictional heating. Light green – FH =0.00. Dark green – FH = 0.06. Contour interval 100°C.*

Heat Flow values

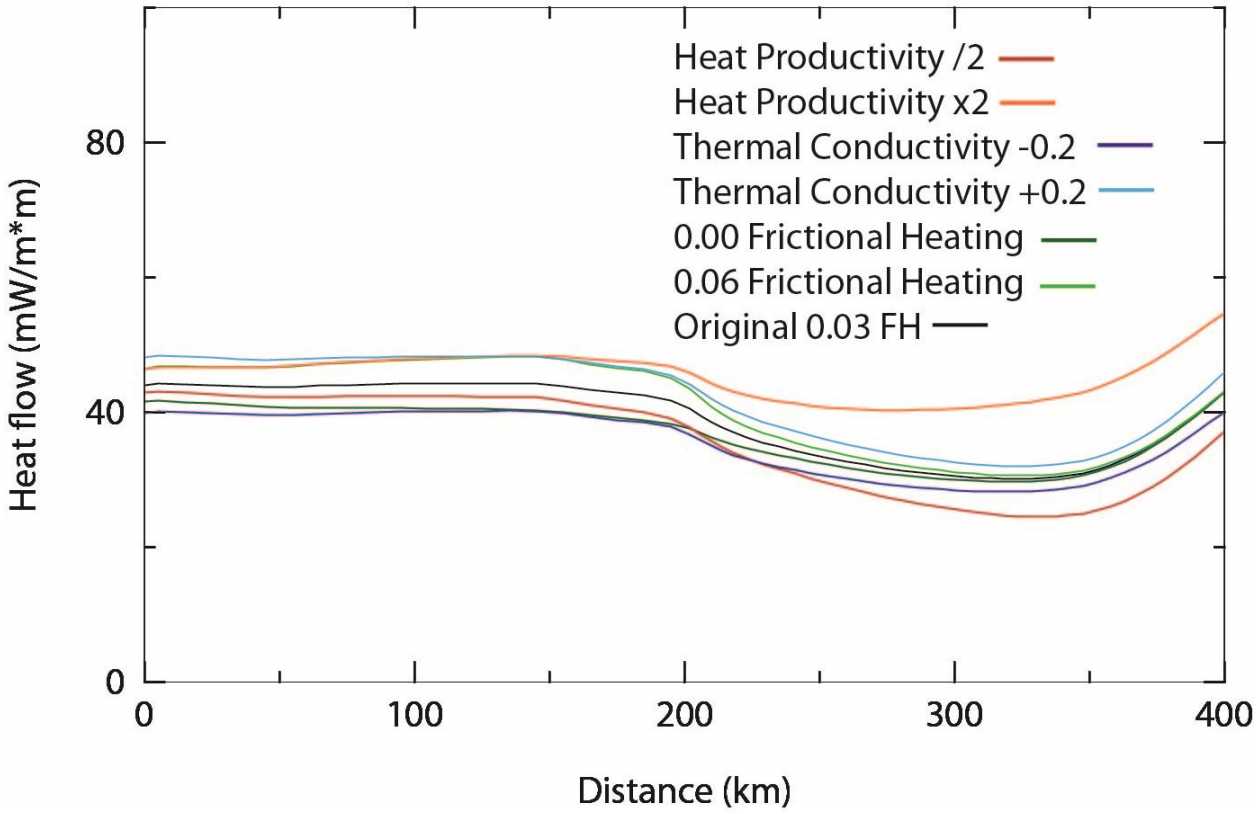

Figure A7. *Comparison of generated heat flow values.*